END

FILMED

DTIC

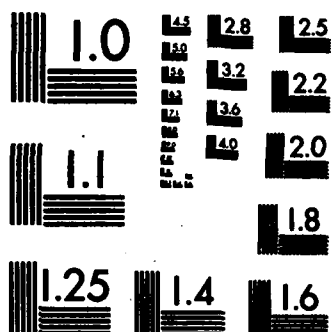|				2.8		2.5
	1.0			**3.2**		**2.2**
				3.6		
				4.0		**2.0**
	1.1					
						1.8
	1.25		**1.4**			**1.6**

MICROCOPY RESOLUTION TEST CHART
NATIONAL BUREAU OF STANDARDS-1963-A

MASSACHUSETTS INSTITUTE OF TECHNOLOGY
LINCOLN LABORATORY

SOLID STATE RESEARCH

QUARTERLY TECHNICAL REPORT

1 FEBRUARY — 30 APRIL 1984

ISSUED 17 AUGUST 1984

Accession For	
NTIS GRA&I	☒
DTIC TAB	☐
Unannounced	☐
Justification___	
By___	
Distribution/	
Availability Codes	
Dist	Avail and/or Special
A-1	

DTIC
ELECTE
NOV 2 3 1984

S   E   D

LEXINGTON   **MASSACHUSETTS**

ABSTRACT

This report covers in detail the solid state research work of the Solid
State Division at Lincoln Laboratory for the period 1 February
through 30 April 1984. The topics covered are Solid State Device
Research, Quantum Electronics, Materials Research, Microelectron-
ics, and Analog Device Technology. Funding is primarily provided
by the Air Force, with additional support provided by the Army,
DARPA, Navy, NASA, and DOE.

TABLE OF CONTENTS

LIST OF ILLUSTRATIONS

LIST OF TABLES

INTRODUCTION

1. SOLID STATE DEVICE RESEARCH

Buried-heterostructure, actively Q-switched diode lasers have been made with threshold currents as low as 14 mA. The lasers operate continuously at room temperature. Full on/off modulation has been observed at measurement-limited rates of about 12.6 GHz, while modulation has been seen at rates of 13.5 GHz.

An electrooptic guided-wave interferometric modulator has been fabricated in GaAs. The interferometer uses three-guide couplers as the input and output sections and slab-coupled p^+-n-n^+ rib waveguides fabricated by Be-ion implantation for the two active arms. These interferometers should be capable of large depths of modulation up to at least 5 GHz.

Measurements of the far-field "antenna" patterns of integrated-optics horns, both as receivers and transmitters, and of the corresponding near-field output patterns have been made. The experimental results agree with theory. The horn antennas used as receivers increase the collection efficiency of the wavefront measurement sensor which is under development.

Nonlinearities in the I-V characteristics of semi-insulating InP as a function of light-spot position, intensity, and uniformity were investigated. Use of p, n, and double p/n planar electrodes indicates that the observed nonlinearities are not due to charge pile-up near the contacts.

2. QUANTUM ELECTRONICS

Na-atom concentration profiles in SiO_2 films have been measured by monitoring the Na fluorescence during reactive-ion etching of the films in a very simple triode plasma reactor. Sensitivities to surface Na concentrations of $\sim 10^{10}$ cm^{-2} have been achieved, with a measurement time of < 4 min. for a 100-nm-thick oxide film.

ArF excimer laser radiation has been used to deposit tungsten films on silicon and on SiO_2 by initiating the gas-phase reaction of WF_6 with H_2. Deposition rates >100 nm/min. and film resistivities as low as two times the bulk value have been obtained at deposition temperatures of 440°C.

3. MATERIALS RESEARCH

The radiation hardness of CMOS devices fabricated in zone-melting-recrystallized Si films on SiO_2-coated Si substrates has been substantially improved, and vertical bipolar transistors have been fabricated in such silicon-on-insulator (SOI) films for the first time. If a bias of –5 V is applied to the Si substrate during irradiation and measurement of the SOI/CMOS devices, both NMOS and PMOS devices exhibit low subthreshold leakage, small threshold voltage shifts, and very little transconductance degradation for total radiation doses up to 10^7 rad(Si). The SOI vertical bipolar transistors, which are n-p-n devices with the emitter formed by low-temperature diffusion from a doped poly-Si film, have electrical characteristics comparable to those of bulk Si devices.

Double-heterostructure AlGaAs diode lasers have been fabricated for the first time on a monolithic GaAs/Si substrate. The heterostructure was prepared by MBE growth of a series of GaAs and AlGaAs layers on a Ge-coated Si wafer. For pulsed operation at 77 K the lowest threshold current was 260 mA, the highest power output was 1.8 mW per facet, and the highest differential quantum efficiency was 1.2 percent.

As a first step in the development of GaAsP/Si tandem solar cells, shallow-homojunction cells have been fabricated in $GaAs_{0.75}P_{0.25}$ epitaxial layers grown on single-crystal GaAs substrates by $AsCl_3$-PCl_3-GaAs-H_2 chemical vapor deposition. By using two intermediate step-graded GaAsP layers to reduce the density of misfit dislocations resulting from the lattice mismatch between $GaAs_{0.75}P_{0.25}$ and GaAs, a one-sun conversion efficiency of 14 percent at AM1 has been obtained for cells with an anodic antireflection coating.

4. MICROELECTRONICS

A self-aligned technique has been developed for embedding two submicrometer-period tungsten gratings, one above the other in single-crystal GaAs. This technique has been used to fabricate permeable-base transistor structures with independently contacted base gratings that permit either vertical or planar integration.

A fabrication technique has been developed which allows the successive multiplication of the number of lines in a grating pattern. The basic sequence consisting of CVD deposition, reactive-ion etching, and selective isotropic etching can be repeatedly applied, each cycle doubling the number of lines in the pattern. Gratings with ~40-nm period have been fabricated by doubling the number of lines in a 160-nm period grating twice.

Direct evidence has been obtained that the presence of impurities in a quantum well will lower the resonant tunneling current density. By eliminating impurities from the well, we have been able to increase the tunneling current density by a factor of nearly 30 over previously reported measurements.

Harmonic multiplication using only solid-state components has yielded submillimeter radiation at 556 GHz (540 μm). This radiation was derived from a Schottky diode frequency tripler and doubler driven in tandem by a 92.7-GHz IMPATT oscillator. Future attention will be given to reducing the noise level by replacing the IMPATT oscillator with a Gunn oscillator.

5. ANALOG DEVICE TECHNOLOGY

A superconductive convolver with 16-dB improvement in output power and 9-dB increase in efficiency has been developed. The new configuration uses mixer rings which employ series arrays of superconductive tunnel junctions driven by delay-line taps in a quasi-balanced manner. The improved dynamic range has allowed demonstration of pulse compression with 850-MHz bandwidth chirped waveforms.

The first observations of acoustic-wave reflections from optically written holographic gratings have been made. It is intended that this effect be exploited to create signal-processing devices of >1-GHz bandwidth employing low-loss bulk acoustic waves.

REPORTS ON SOLID STATE RESEARCH

1 February through 30 April 1984

PUBLISHED REPORTS

Journal Articles

JA No.

5495	Use of Plasma-Deposited Si_3N_4 as an Oxidation Mask in the Fabrication of GaAs Shallow-Homojunction Solar Cells	G.W. Turner M.K. Connors	J. Electrochem. Soc. 131, 1211 (1984)
5499	A CCD Time-Integrating Correlator	B.E. Burke D.L. Smythe, Jr.	IEEE J. Solid-State Circuits SC-18, 736 (1983)
5501	Deep-UV Spatial-Frequency Doubling by Combining Multi-layer Mirrors with Diffraction Gratings	A.M. Hawryluk* H.I. Smith* D.J. Ehrlich	J. Vac. Sci. Technol. B 1, 1200 (1983)
5504	A High-Speed Digitally Programmable CCD Transversal Filter	A.M. Chiang B.E. Burke	IEEE J. Solid-State Circuits SC-18, 745 (1983)
5528	Optimal Design of Amorphous/Crystalline Tandem Cells	J.C.C. Fan B.J. Palm	Solar Cells 11, 247 (1984)
5536	Monolithic Silicon Bolometers	P.M. Downey* A.D. Jeffries* S.S. Meyer* R.W. Weiss* F.J. Bachner J.P. Donnelly W.T. Lindley R.W. Mountain D.J. Silversmith	Appl. Opt. 23, 910 (1984)
5546	Efficient AlGaAs Shallow-Homojunction Solar Cells	R.P. Gale J.C.C. Fan G.W. Turner R.L. Chapman J.V. Pantano	Appl. Phys. Lett. 44, 632 (1984)

*Author not at Lincoln Laboratory.

*Author not at Lincoln Laboratory.

6445	A CCD Matrix-Matrix Product Parallel Processor	A.M. Chiang R.W. Mountain D.J. Silversmith B.J. Felton	IEEE Intl. Solid-State Cir- cuits Conf., San Francisco, 22-24 February 1984, Digest of Technical Papers, p. 110

* * * * *

UNPUBLISHED REPORTS

Journal Articles

JA No.

5465	Electron Devices on Piezoelectric Semiconductors: A Device Model	R.S. Withers	Accepted by IEEE Trans. Sonics Ultrason.
5522	Broadband Guided-Wave Electrooptic Modulators	R.A. Becker	Accepted by IEEE J. Quantum Electron.
5535	Topographic Imperfections in Zone-Melting-Recrystallized Si Films on SiO_2	C.K. Chen M.W. Geis B-Y. Tsaur R.L. Chapman J.C.C. Fan	Accepted by J. Electrochem. Soc.
5545	Fabrication, Characterization and Analysis of Mass-Transported GaInAsP/InP Buried-Heterostructure Lasers	Z.L. Liau J.N. Walpole D.Z. Tsang	Accepted by IEEE J. Quantum Electron.
5551	Lasers, Their Development and Applications at M.I.T. Lincoln Laboratory	R.H. Rediker I. Melngailis A. Mooradian	Accepted by IEEE J. Quantum Electron. Centennial Issue
5585	Wideband Electrooptic Guided-Wave Analog-to-Digital Converters	R.A. Becker C.E. Woodward F.J. Leonberger R.C. Williamson	Accepted by Proc. IEEE, Special Issue on Optical Computing
5599	GaAs MESFETs Fabricated on Monolithic GaAs/Si Substrates	H.K. Choi B-Y. Tsaur G.M. Metze G.W. Turner J.C.C. Fan	Accepted by IEEE Electron Device Lett.

Meeting Speeches[†]

---

*Author not at Lincoln Laboratory.
[†]Titles of Meeting Speeches are listed for information only. No copies are available for distribution.

MS No.

6097D	Wideband Analog Signal Processing with Superconductive Circuits	R.S. Withers	U.S.-Japanese Workshop on Josephson Junction Technology, Tokyo, Japan, 19-20 April 1984
6192B	Advances in LEC Growth of InP Crystals	G.W. Iseler	Seminar, Dept. of Electrical Engineering, University of Maryland, College Park, 8 March 1984
6226A	Laser Remote Sensing of Atmospheric Species Using IR Differential-Atmospheric LIDAR	D.K. Killinger	Seminar, Dept. of Planetary Sciences, Harvard University, Cambridge, Massachusetts, 2 March 1984
6242A	Spectral Properties of Semiconductor Diode Lasers	A. Mooradian	Modern Optics and Spectroscopy Seminar, M.I.T., 1 May 1984
6299B	Nitrocellulose as a Self-Developing Resist with Submicrometer Resolution and Processing Stability	M.W. Geis J.N. Randall T.F. Deutsch N.N. Efremow J.P. Donnelly J.D. Woodhouse	Electrical Engineering Seminar, Los Alamos National Laboratory, Los Alamos, New Mexico, 1 March 1984
6343A	High-Quality Silicon Films Prepared by Zone-Melting Recrystallization	B-Y. Tsaur	SOI-3DIC Workshop, San Francisco, California, 21 February 1984
6380A	New Solid-State Lasers	P.F. Moulton	Electro-Optics/Laser Intl. Conf., Tokyo, Japan, 16-18 February 1984
6389C	Wideband Analog Signal Processing	S.A. Reible	Seminar, Dept. of Physics, University of Wisconsin, Milwaukee, 12 March 1984
6400A	Laser Photolysis for Materials Growth	D.J. Ehrlich J.Y. Tsao	ICMOVPE II, University of Sheffield, England, 10-12 April 1984
6439A	Auger Analysis of Electronic Materials — Some Illustrative Examples	M.C. Finn	Southern California Microbeam Analysis Society Mtg., Pasadena, California, 3 February 1984

MS No.

6444	AlGaAs Shallow-Homojunction Solar Cells for Tandem Applications	R.P. Gale G.W. Turner J.C.C. Fan R.L. Chapman J.V. Pantano	
6450	Ultralight GaAs CLEFT Solar Cells for Space Applications	J.C.C. Fan R.W. McClelland B.D. King	17th IEEE Photovoltaic Specialists Conference, Kissimmee, Florida, 1-4 May 1984
6452	GaAsP Shallow-Homojunction Solar Cells for Tandem Applications	R.W. McClelland B.D. King J.C.C. Fan R.L. Chapman	
6456	GaAs/Ge/Si Solar Cells	B-Y. Tsaur J.C.C. Fan G.W. Turner B.D. King R.W. McClelland	
6651	A New High-Efficiency GaAs Solar Cell Structure Using a Heterostructure Back-Surface Field	R.P. Gale J.C.C. Fan G.W. Turner R.L. Chapman	
6458	The Microstructure, Diffusion, Stress and Electrical Characteristics of 300-500 Å Thick Tungsten Films on GaAs	W.D. Goodhue G.A. Lincoln K.B. Nichols	WOCSEMMAD '84, San Francisco, California, 19-23 February 1984
6479	PMMA and Gold Proton Masks for Gallium Arsenide	S. Rabe C.O. Bozler N.N. Efremow	
6465	Masked Ion Beam Lithography Using Stencil Masks	J.N. Randall D.C. Flanders N.P. Economou	SPIE Conf. on Micro-Lithography, Santa Clara, California, 15-16 March 1984
6499	TaSi$_2$ Formation by Rapid Thermal Annealing	D.L. Kwong* R. Kwor* B-Y. Tsaur	Electrochemical Society Mtg., Cincinnati, Ohio, 6-11 May 1984

*Author not at Lincoln Laboratory.

MS No.

6500	Effect of Low Temperature Pre-anneal and High Temperature Rapid Thermal Annealing on Arsenic-Implanted Silicon	R. Kwor* D.L. Kwong* B-Y. Tsaur	Electrochemical Society Mtg., Cincinnati, Ohio, 6-11 May 1984
6506A	Developing a Technology Base for Advanced Devices and Circuits	N.P. Economou	Electrical Engineering Seminar, University of Pennsylvania, Philadelphia, 22 March 1984
6510	Fabrication and Characterization of Mach-Zehnder Modulators in LiNbO$_3$	R.A. Becker	1984 Mtg., American Ceramic Society, Pittsburgh, Pennsylvania, 30 April 1984
6528	Broadband Ti:LiNbO$_3$ Guided-Wave Lumped-Element and Traveling-Wave Interferometric Modulators	R.A. Becker	
6538	Integrated-Optical Channel-Waveguide Frequency Shifter	L.M. Johnson R.A. Becker R.H. Kingston	
6543	Design, Fabrication and Characterization of Horn Antennas in Ti-indiffused LiNbO$_3$ Channel Waveguides	R.H. Rediker T.A Lind R.A. Becker L.M. Johnson	7th Topical Mtg. on Integrated and Guided-Wave Optics, Kissimmee, Florida, 24-26 April 1984
6553	A Gallium Arsenide Electrooptical Interferometric Modulator	J.P. Donnelly N.L. DeMeo G.A. Ferrante K.B. Nichols F.J. O'Donnell	
6561	Characterization of Instability in Ti-indiffused LiNbO$_3$ Modulators Due to Photorefractive and Non-Optical Sources	R.A. Becker	
6562	Mass-Transported GaInAsP/InP Buried-Heterostructure Lasers and Integrated Mirrors	Z.L. Liau J.N. Walpole D.Z. Tsang	
6574	High-Speed Integrated Optoelectronic Signal Processing Devices	F.J. Leonberger	

*Author not at Lincoln Laboratory.

| 6558 | Zone Melting Recrystallization of Patterned Films and Low Temperature Graphoepitaxy | H.I. Smith* C.V. Thompson* M.W. Geis H.A. Atwater* T. Yonehara* C.C. Wong* | Materials Research Society Mtg., Boston, 26-30 November 1983 |

| 6565,A | The Search for the Fastest Three-Terminal Device: The Permeable Base Transistor Approach | B.A. Vojak | Graduate Student Electrical Engineering Seminar, University of Illinois, Urbana, 6 February 1984; Northwestern University, Evanston, Illinois, 9 February 1984 |

| 6566 | Microwave Semiconductor Device Research at Lincoln Laboratory | R.A. Murphy | Graduate Student Electrical Engineering Seminar, Washington University, St. Louis, Missouri, 10 February 1984 |

| 6567 | Submicrometer Structures and Their Application to High Speed Devices | D.D. Rathman | Electrochemical Society, Local Chapter Mtg., Newton, Massachusetts, 14 February 1984 |

| 6569 | Buried-Heterostructure GaInAsP Diode Lasers | D.Z. Tsang Z.L. Liau J.N. Walpole S.H. Groves | Seminar, Bell Laboratories, Holmdel, New Jersey, 15 February 1984 |

| 6577 | Zone-Melting Recrystallization of Si Films with a Moveable-Strip-Heater Oven | M.W. Geis H.I. Smith* B-Y. Tsaur J.C.C. Fan D.J. Silversmith R.W. Mountain | Electrical Engineering Seminar, Bell Laboratories, Murray Hill, New Jersey, 22-23 February 1984 |
| 6578 | Large Area Ion Beam Assisted Etching of GaAs with High Etch Rates and Controlled Anisotropy | G.A. Lincoln M.W. Geis S.W. Pang N.N. Efremow | |

---

*Author not at Lincoln Laboratory.

MS No.

ORGANIZATION

SOLID STATE DIVISION

A.L. McWhorter, *Head*
I. Melngailis, *Associate Head*
E. Stern, *Associate Head*
J.F. Goodwin, *Assistant*

P.E. Tannenwald, *Senior Staff*

QUANTUM ELECTRONICS

A. Mooradian, *Leader*
P.L. Kelley, *Associate Leader*

Barch, W.E.
Belanger, L.J.
Brueck, S.R.J.
Burke, J.W.
Bushee, J.F., Jr.
DeFeo, W.E.
Deutsch, T.F.
Ehrlich, D.J.
Feldman, B.
Hancock, R.C.

Harrison, J.*
Johnson, B.C.*
Killinger, D.K.
Lenth, W.
Menyuk, N.
Moulton, P.F.
Sedlacek, J.H.C.
Sharpe, K.A.
Sullivan, D.J.
Tsao, J.Y.

ELECTRONIC MATERIALS

A.J. Strauss, *Leader*
J.C.C. Fan, *Associate Leader*
J.G. Mavroides, *Senior Staff*
H.J. Zeiger, *Senior Staff*

Anderson, C.H., Jr.
Branz, H.M.*
Button, M.J.
Chapman, R.L.
Chen, C.K.
Choi, H.K.
Connors, M.K.
Delaney, E.J.
Fahey, R.E.
Finn, M.C.
Gale, R.P.
Iseler, G.W.
King, B.D.

Kolesar, D.F.
Krohn, L., Jr.
Mastromattei, E.L.
McClelland, R.W.
Metze, G.M.
Nitishin, P.M.
Palm, B.J.
Pantano, J.V.
Tracy, D.M.
Tsaur, B-Y.
Turner, G.W.
Windhorn, T.H.

APPLIED PHYSICS

R.C. Williamson, *Leader*
F.J. Leonberger, *Assistant Leader*
T.C. Harman, *Senior Staff*
R.H. Kingston, *Senior Staff*
R.H. Rediker, *Senior Staff*

Becker, R.A.
Chinnock, C.B.
Cox, C.H., III
DeMeo, N.L., Jr.
Diadiuk, V.
Donnelly, J.P.
Ferrante, G.A.
Groves, S.H.

Hovey, D.L.
Johnson, L.M.
Liau, Z.L.
McBride, W.F.
Molter-Orr, L.*
O'Donnell, F.J.
Plonko, M.C.
Reeder, R.E.

Schloss, R.P.*
Spears, D.L.
Tsang, D.Z.
Walpole, J.N.
Whitaker, N.*
Woodhouse, J.D.
Yap, D.*

---

* Research Assistant

ANALOG DEVICE TECHNOLOGY

J.H. Cafarella, *Leader*
R.W. Ralston, *Associate Leader*

Anderson, A.C.	Gottschalk, P.G.*	Melngailis, J.†
Arsenault, D.R.	Green, J.B.	Oates, D.E.
Boisvert, R.R.	Hauser, E.M.	Reible, S.A.
Bouman, C.A.	Holtham, J.H.	Sage, J.P.
Brogan, W.T.	Kernan, W.C.	Slattery, R.L.
Dolat, V.S.	Lattes, A.L.	Smith, L.N.
Fischer, J.H.	Macedo, E.M., Jr.	Withers, R.S.
Fitch, G.L.	Macropoulos, W.	Yao, I.
Flynn, G.T.	Marden, J.A.	

MICROELECTRONICS

W.T. Lindley, *Leader*
N.P. Economou, *Associate Leader*
R.A. Murphy, *Assistant Leader*

Bozler, C.O.	Hollis, M.A.	Peck, D.D.
Bromley, E.I.	Kosicki, B.B.	Piacentini, W.J.
Burke, B.E.	Lax, B.†	Pichler, H.H.
Calawa, A.R.	LeCoz, Y.L.*	Rabe, S.
Chen, C.L.	Lincoln, G.A., Jr.	Randall, J.N.
Chiang, A.M.	Lyszczarz, T.M.	Rathman, D.D.
Chu, A.	Mahoney, L.J.	Shaver, D.C.
Clifton, B.J.	Manfra, M.J.	Silversmith, D.J.
Daniels, P.J.	McGonagle, W.H.	Smythe, D.L., Jr.
Durant, G.L.	Mountain, R.W.	Sollner, T.C.L.G.
Efremow, N.N., Jr.	Mroczkowski, I.H.	Taylor, J.A.*
Felton, B.J.	Nichols, K.B.	Vera, A.
Flanders, D.C.	Pang, S.W.	Vojak, B.A.
Geis, M.W.	Parker, C.D.	Wilde, R.E.
Gray, R.V.		

---

* Research Assistant
† Part Time

1. SOLID STATE DEVICE RESEARCH

1.1 Q-SWITCHING OF LOW-THRESHOLD BURIED-HETEROSTRUCTURE DIODE LASERS AT 13 GHz

Actively Q-switched diode lasers are of interest for high-bandwidth optical fiber communication systems. Laser pulses at modulation rates of several tens of gigahertz should be possible.[1] Previously reported actively Q-switched semiconductor lasers with an integrated electroabsorption modulator have been operated on a pulsed basis with thresholds of 240 mA.[1,2] A two-section buried-heterostructure laser with a proton-isolated modulator was also reported.[3] These devices had a threshold of about 40 mA and were Q-switched at 3 GHz. Here we report buried-heterostructure Q-switched lasers[4] with thresholds as low as 14 mA at an emission wavelength of 1.3 μm. These devices are operated with DC current applied to an amplifier section and microwave modulation applied to a reverse-biased pn junction modulator. Since the capacitance of the intracavity modulator can be as low as 0.1 pF under a few volts reverse bias, the laser can be easily modulated when integrated with low-power, high-speed transistors without the high current drive required for direct-current modulation. The devices have been continuously operated with full on/off modulation confirmed at rates of 12.6 GHz.

The design, fabrication, and operation of the laser are similar to the zinc-diffused stripe Q-switched lasers reported earlier[1,2] except for modifications made to incorporate the buried heterostructure. The laser is fabricated from a double-heterostructure wafer consisting of an LPE-grown 2×10^{18} cm^{-3} Sn-doped buffer layer, a 1×10^{16} cm^{-3} n-type $Ga_{0.26}In_{0.74}As_{0.60}P_{0.40}$ active layer, and a 1×10^{16} cm^{-3} n-type InP cap layer. Both selective chemical etching to define an active region about 2 μm wide and a mass transport process[5] to bury the active region are used to form the buried heterostructure. Zinc is selectively diffused to form an amplifier section, and beryllium is selectively implanted to form a modulator section, as shown in Figure 1-1. Au-Zn contacts are applied to the p-type regions and Au-Sn contacts are applied to the n-type substrate. Mirrors are formed by cleaving. The amplifier is forward-biased to produce optical gain while the modulator is reverse-biased to produce optical loss by electroabsorption (Franz-Keldysh effect). For optical energies slightly less than the bandgap of the GaInAsP layer, the optical absorption can be controlled by the electric field produced in the modulator p-n junction. The bulk absorption in the GaInAsP layer can be increased from a very small value to over 1000 cm^{-1} as the electric field is varied from zero to $>3.6 \times 10^5$ V/cm for photon energies as much as 60 meV below the energy gap.[6] The amplifier and modulator are optically coupled but electrically isolated by the waveguide section. The cross section of the buried heterostructure is constant throughout the device. The active region is about 0.2 μm thick and 2 μm wide. The position of the beryllium-implanted junction is deliberately offset from the quaternary layer, as shown in Figure 1-1, to prevent electroabsorption at zero bias.[2] Typically the length of the amplifier is 150 to 250 μm while the length of the modulator is 25 μm.
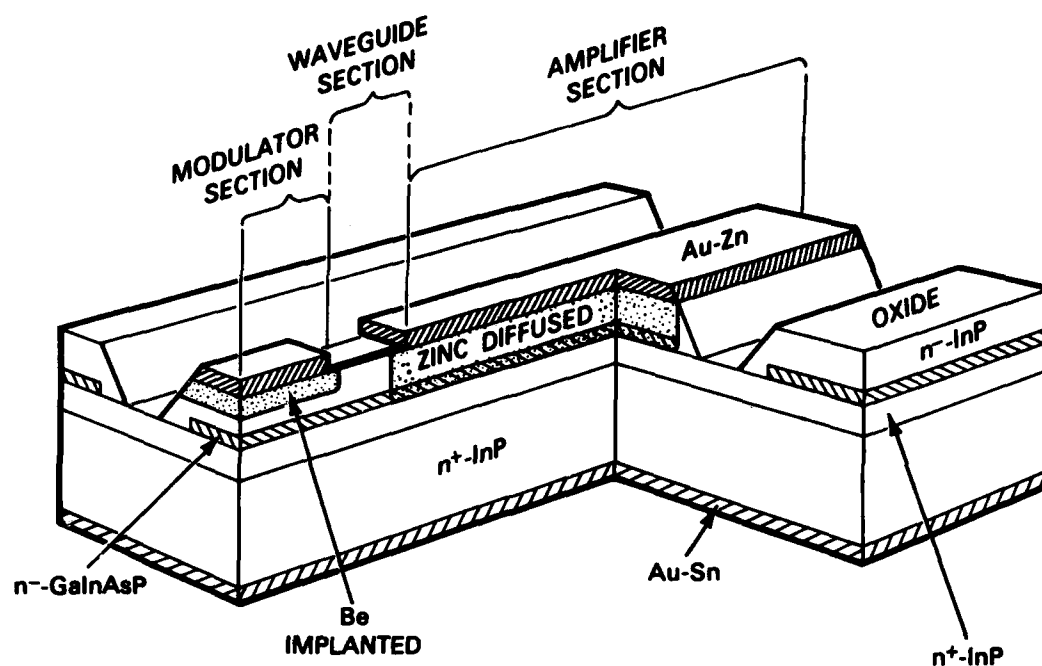
Figure 1-1. Perspective cutaway view of the Q-switched laser. The buried-heterostructure active region extends through all three sections of the device.
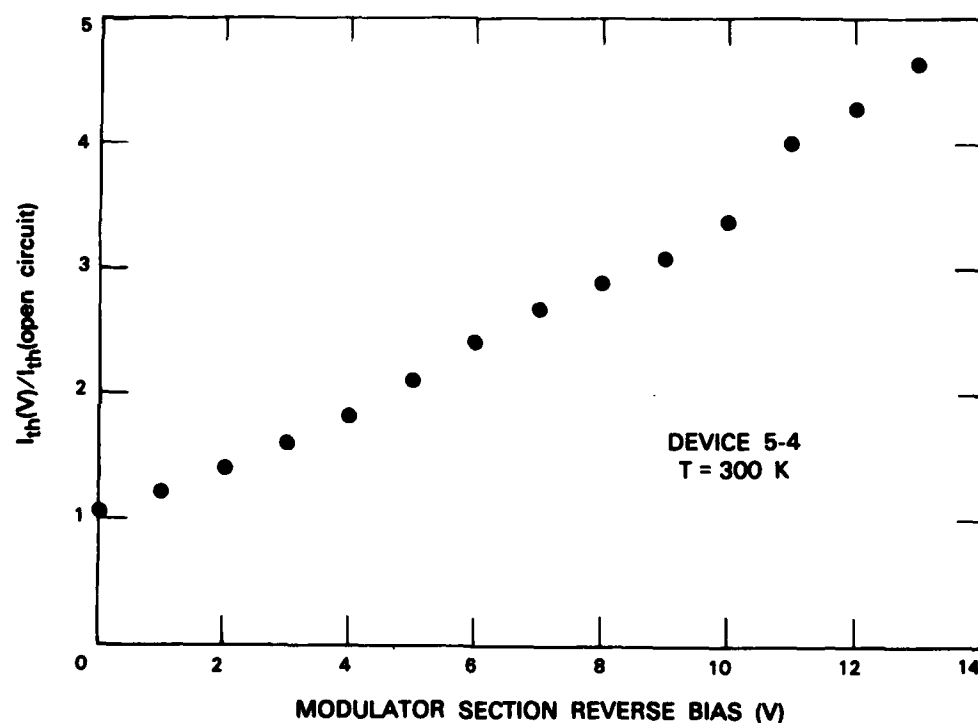
Figure 1-2. Pulsed threshold, normalized to the threshold of the laser with the modulator open, as a function of modulator reverse bias.

The laser is mounted in a package between two microstriplines which bring the electrical drive signals to the two sections. In order to facilitate bonding, the device is mounted with the substrate side soldered to the heatsink.

The lasers have thresholds as low as 14 mA with the modulator open-circuited. The low threshold of the lasers permits continuous operation at room temperature. In order to characterize the modulator loss, the threshold of the laser can be measured as a function of the modulator reverse bias. At 13 V reverse bias the pulsed threshold for one device (Figure 1-2) increases by a factor of about 4.5 compared to the threshold with the modulator open-circuited, indicating a substantial variation in intracavity loss.

The devices were modulated by application of both a DC voltage and a microwave signal to the modulator.[1] Typically 70 to 200 mW of microwave power and a few volts of DC reverse bias were sufficient to drive the unmatched modulator. The devices were modulated at rates between 2 and 13.5 GHz. The optical pulses out of the laser were collected and focused on a back-illuminated 25-μm-dia. GaInAs/InP p-i-n photodiode that had <70-ps FWHM response time.[7] The detector output was displayed on a sampling oscilloscope which had a 20-ps rise time. Continuous Q-switched operation at a rate of 8 GHz with full on/off modulation is illustrated in Figure 1-3(a). The laser amplifier was driven at 2.1 times the threshold of the device with the modulator open. The modulator was DC biased with 1.3 V reverse bias. Microwave power of 100 mW was applied to the system. The actual modulator drive power was somewhat less due to insertion losses in the bias tee, cables, and connectors. Full on/off modulation was seen at 10.2 GHz as shown in Figure 1-3(b), although the detected signal is smaller. Full on/off modulation was observed up to 12.6 GHz with further reduction in output. At 13.5 GHz the depth of modulation was limited by the detector and its package.

The results reported here demonstrate Q-switched diode lasers with low threshold current. The lasers have been modulated at rates above 13 GHz and should be useful for optical fiber communication systems and other applications requiring such high rates.

D.Z. Tsang   S.H. Groves
J.N. Walpole   V. Diadiuk
Z.L. Liau

1.2 A GALLIUM ARSENIDE ELECTROOPTIC INTERFEROMETRIC MODULATOR

Interferometers in which the effective length of one arm can be electronically varied are important optical components for signal processing and high-speed laser modulation. Integrated optical Mach-Zehnder interferometers have been fabricated in LiNbO$_3$ (References 8-10) but, to our knowledge, there have been no reports of such an interferometer in the III-V semiconductors. Interferometers in the III-V's have the potential of being integrated with lasers, detectors, and high-speed electronic devices for a fully monolithic integrated optical circuit. In this section we report initial results on a GaAs interferometer capable of amplitude modulation via the electrooptic effect.
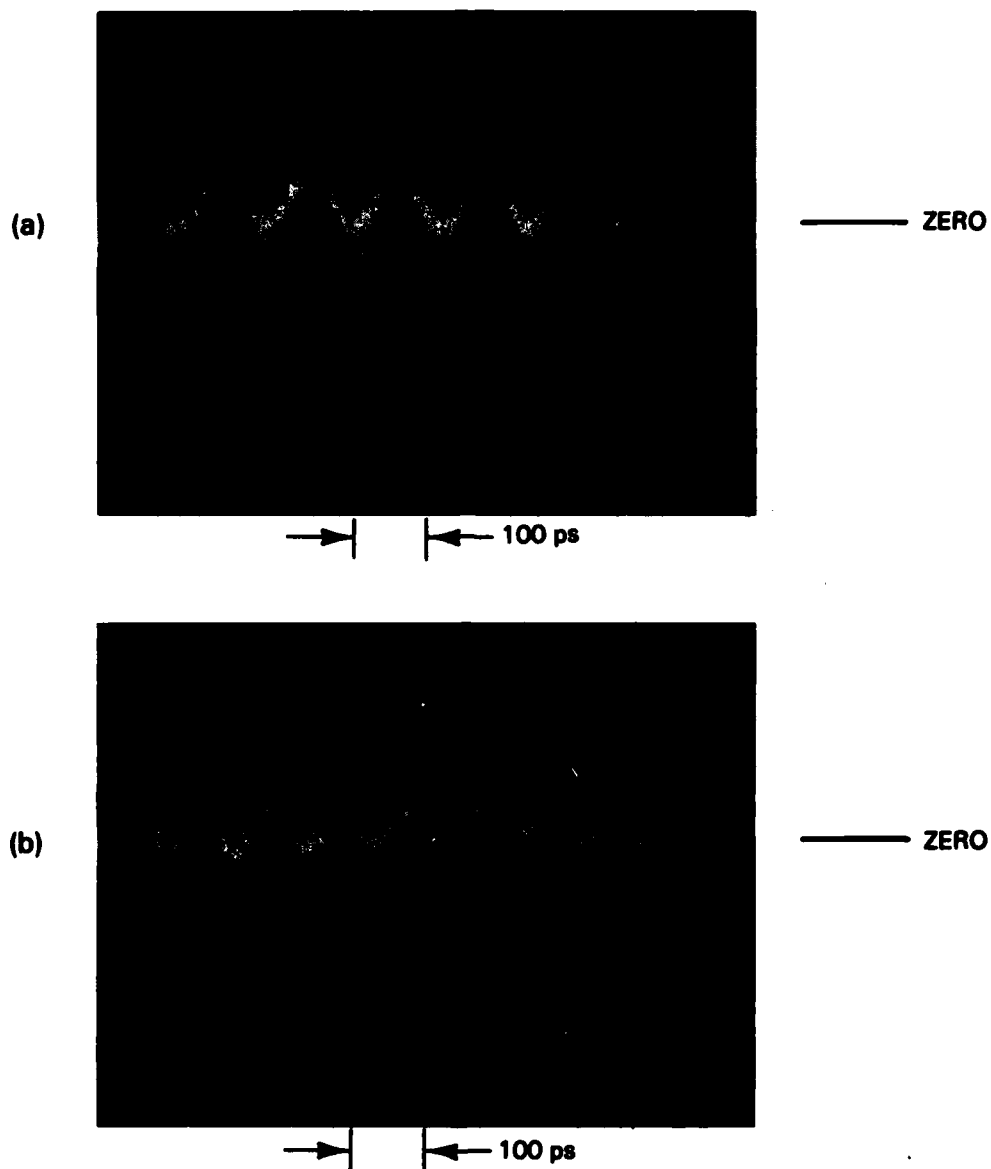
Figure 1-3. (a) Continuous Q-switching at 8 GHz and (b) Q-switching at 10.2 GHz. Both figures have an extra trace to show the reference level with the light blocked. The intensity of the reference was reduced in (b).

4

A schematic representation of the interferometer is shown in Figure 1-4. The input and output sections are three-guide couplers[11-13] which, for this application, behave similarly to "Y" branches. They consist of three n^--n^+ slab-coupled rib waveguides,[14] as illustrated in cross section A-A. Power input into the center guide is divided equally between the two outer guides at the coupling length L_c. For power input into the two outside guides, the in-phase components of the two inputs are combined in the center guide in a length L_c while the out-of-phase components remain in the outside guides. Three-guide couplers were used instead of the traditional "Y" branches to avoid fabrication difficulties associated with making low-loss "Y" branches in rib-coupled semiconductor waveguides. The two active arms of the interferometer are p^+-n^--n^+ slab-coupled rib waveguides,[15] as illustrated in cross section B-B. The effective index in these arms may be changed via the electrooptic effect by changing the bias on the p-n junctions. The phase of the output of either or both arms of the interferometer may therefore be changed, resulting in modulation of the signal out of the center guide of the output three-guide coupler. Although the experimental data presented here were obtained by applying a voltage to only one arm of the interferometer, a DC bias can be applied to both arms and the signal applied in a push-pull fashion, as illustrated in Figure 1-4.

The interferometer was fabricated in a 4.2-μm-thick nominally undoped (n < 3 × 10^{15} cm^{-3}) n^- epitaxial layer grown on an n^+ GaAs substrate (n = 2 × 10^{18} cm^{-3}). Be was implanted into the regions which would be used for the arms of the interferometer to form a p^+ region approximately 1.5 μm deep.[16] After implantation annealing, the rib-waveguide interferometric structure illustrated in Figure 1-4 was etched. Ti-Au and Au-Sn contacts were used to contact the p^+ implanted regions and the n^+ substrate, respectively. The p-n junctions had low leakage currents and breakdown voltages >45 V. The GaAs wafer was then cleaved so that the input and output three-guide couplers would be one coupling length, 3.2 mm. The arms of the interferometer were 2.5 mm long. The three-guide couplers were designed using a slab-coupled waveguide effective-index approximation so that the coupling length would not be too critically dependent on the etch depth (≈1.5 μm) or width of the guides (≈5 μm). In addition, the separation between the two outside guides was made sufficiently large so that coupling between the two arms of the interferometer would be negligible.

To test the interferometer, TE-polarized 1.3-μm light from an InGaAsP/InP diode laser was end-fire coupled into the center guide of the input three-guide coupler. The output of the output coupler was collected by a microscope and viewed with either an infrared vidicon or a Ge photodiode detector. Figure 1-5(a) shows the signal obtained by mechanically scanning the output across a detector with no bias applied to either arm of the interferometer. Almost all the output is from the center guide, indicating that the length of the input and output three-guide couplers was ≈L_c, as designed. With a bias applied to either arm, the output of the center guide decreases, as expected, while the output of the outside guides increases. The output of the interferometer with one arm biased near the point where the phase in that arm is changed by π radians is shown in Figure 1-5(b). Much of the asymmetry observed in Figure 1-5 is due to the measurement system.

5
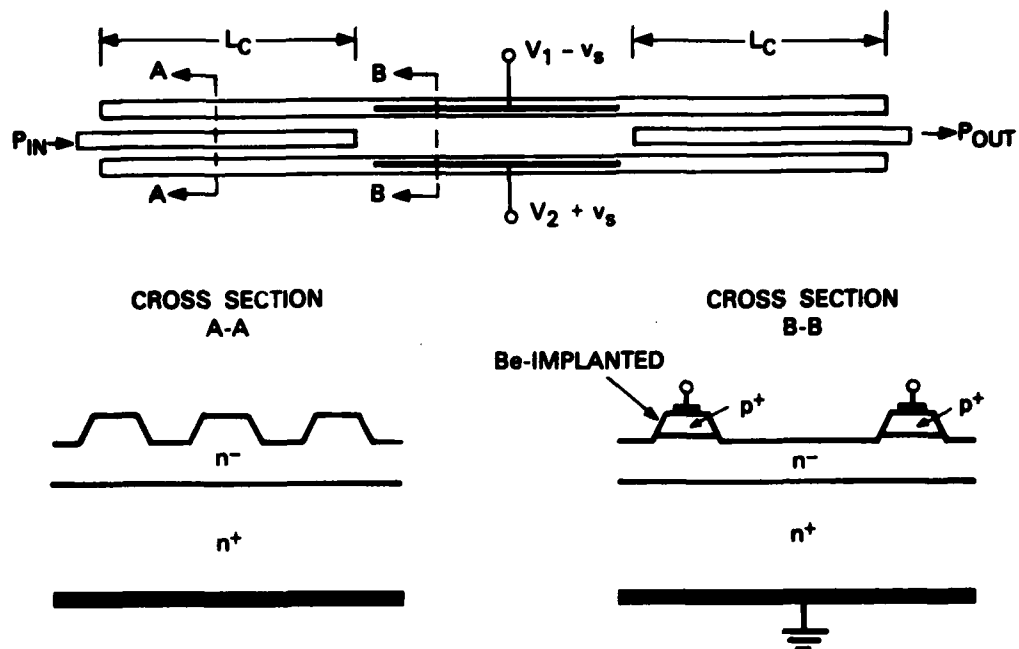
Figure 1-4. Schematic illustration of a GaAs electrooptical interferometer modulator.

(a)　　　　　　　　　　　　(b)
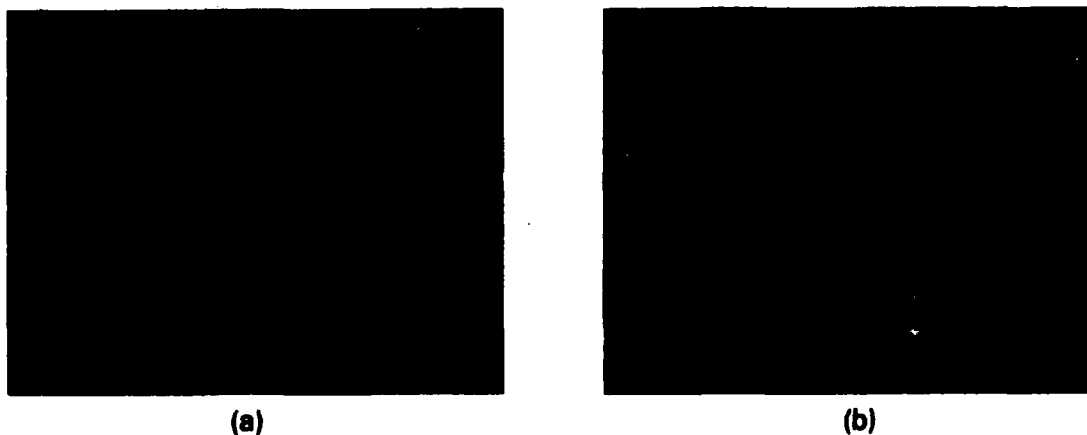
Figure 1-5. Signal obtained by mechanically scanning the output of the interferometer across a detector with (a) 0 V and (b) 25 V applied to one arm of the interferometer.
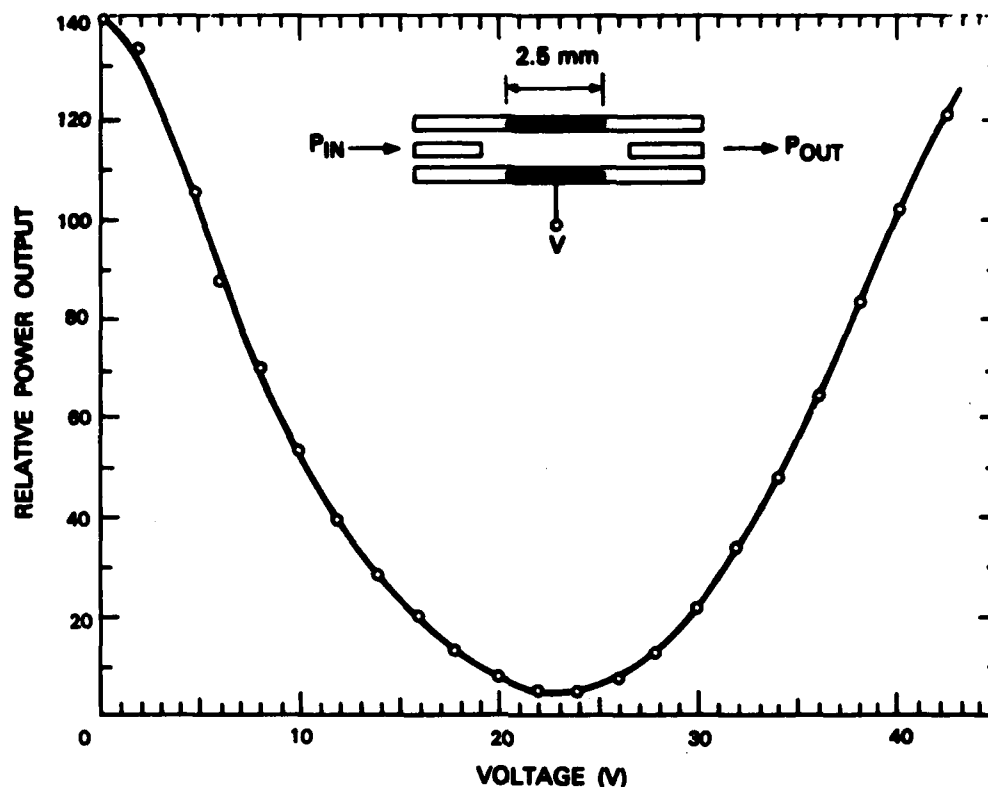
Figure 1-6. Relative power out of center guide of the output three-guide coupler vs voltage applied to one arm of the interferometer.

The output of the center guide vs bias on one of the arms is shown in Figure 1-6. As expected, the output is approximately a cosine function of voltage. Changes in electric field shape in the p^+-n^--n^+ junction with applied voltages (below that required for punch-through operation) cause a deviation from the cosine function, particularly at low voltages. The extinction ratio is 14.5 dB (96.5 percent). In another experiment, one arm of the interferometer was biased to ≈ 10 V and an AC 100-kHz signal applied to achieve large-signal AM modulation. The capacitance of one arm of the modulator is <1 pF, which means these interferometers should be capable of modulation up to at least 5 GHz in a 50-Ω system.

J.P. Donnelly   K.B. Nichols
N.L. DeMeo   F.J. O'Donnell
G.A. Ferrante

1.3 DESIGN, FABRICATION, AND CHARACTERIZATION OF HORN ANTENNAS IN Ti-INDIFFUSED LiNbO₃ CHANNEL WAVEGUIDES

Horn "antennas" in $LiNbO_3$ are useful for matching field patterns of components being coupled to single-mode $LiNbO_3$ waveguides and for increasing the collection efficiency of the wavefront sensor described below. The measurements described here also further the basic understanding of the operation of these horns.

7
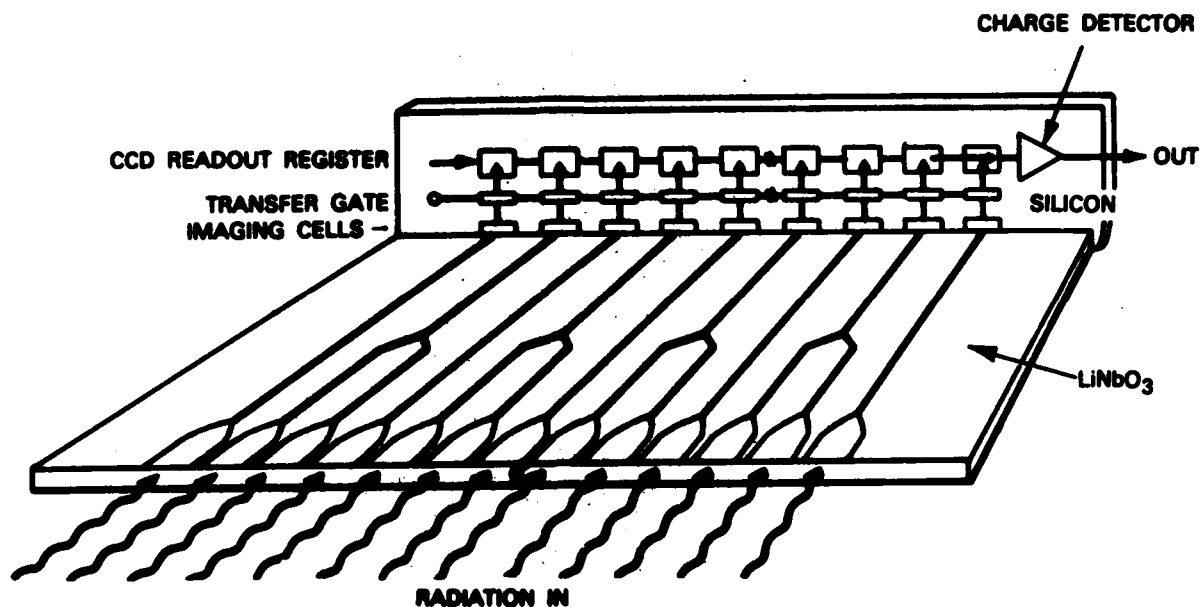
Figure 1-7. A wavefront measurement sensor consisting of an array of interferometers and straight waveguides with horn antennas at the input and CCD imager at the output.

In the wavefront measurement sensor, spatial variations in intensity and phase along the wavefront are measured using an array of alternate straight waveguides (for intensity) and interferometers (for phase). Figure 1-7 shows a simplified one-dimensional sensor including a CCD imager at the output and horn antennas to improve the collection efficiency at the input. Preliminary results on the performance of the interferometer and waveguide portions of the sensor have been presented. This report concerns itself with the performance of the horn antennas.

The horns and waveguides whose performance is described below were fabricated by diffusing 400-Å-thick Ti into an X-cut $LiNbO_3$ wafer for 5 hr at 1000°C in an atmosphere of argon and water vapor. The 3.8-μm-wide waveguides were oriented along the Y-direction and supported single TE and TM modes for $\lambda = 0.81$ μm. The horns which were nearly parabolic were designed using the criteria that require the horn angle to be less than the projection of the ray angle of the lowest-order mode in the plane of the horn.[17,18] Also taken into account in the design of the horn was the increasing Ti concentration and thus the increasing refractive index change due to the decreasing effect of lateral diffusion as the horn gets wider.[19]

The horns were studied as receiving antennas using the experimental arrangement shown in Figure 1-8. By appropriately rotating mirrors Nos. 1 and 2, the angle of the incident wave was changed while keeping the position of the wave on the $LiNbO_3$ sample unchanged. The incident field had uniform intensity and linear phase across the waveguide
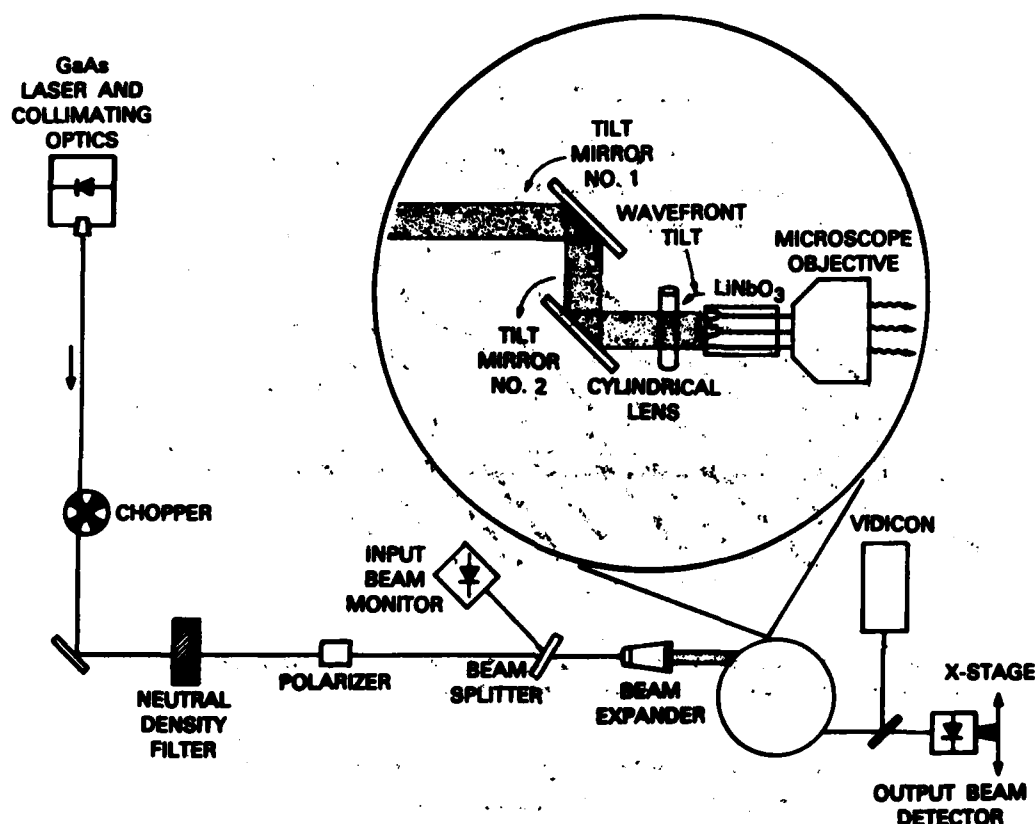
Figure 1-8. Experimental arrangement to measure far-field patterns of horns as receiving antennas. Although only two horns and one straight waveguide are shown on the LiNbO$_3$ wafer, there are over 100 horns and 30 straight waveguides on the wafer.

endface. The waveguide output normalized to the laser output was measured using the two photodiodes shown in the figure. To obtain the transmitting antenna patterns, the LiNbO$_3$ sample shown in Figure 1-8 was rotated 180° in the plane of the wafer, the input beam focused into one waveguide, the microscope objective shown in the output in Figure 1-8 removed, and the output detector translated in the plane perpendicular to the beam. Again, the normalized output was measured. The following measurements were taken: the receiving and transmitting (far-field) antenna patterns, both in the plane of the LiNbO$_3$ wafer as shown in Figure 1-8 and in the plane perpendicular to that of the wafer, and the near-field transmitter mode patterns.

The performance of 20-μm aperture horns is described here. Figure 1-9 shows the measured far-field receiving antenna pattern compared to a Gaussian curve. Figure 1-10 shows the measured far-field transmitting antenna pattern compared to the same Gaussian curve. The receiver and transmitter antenna patterns are nearly identical as expected. The full-width

9

ANTENNA PATTERN: ANGLE (deg)
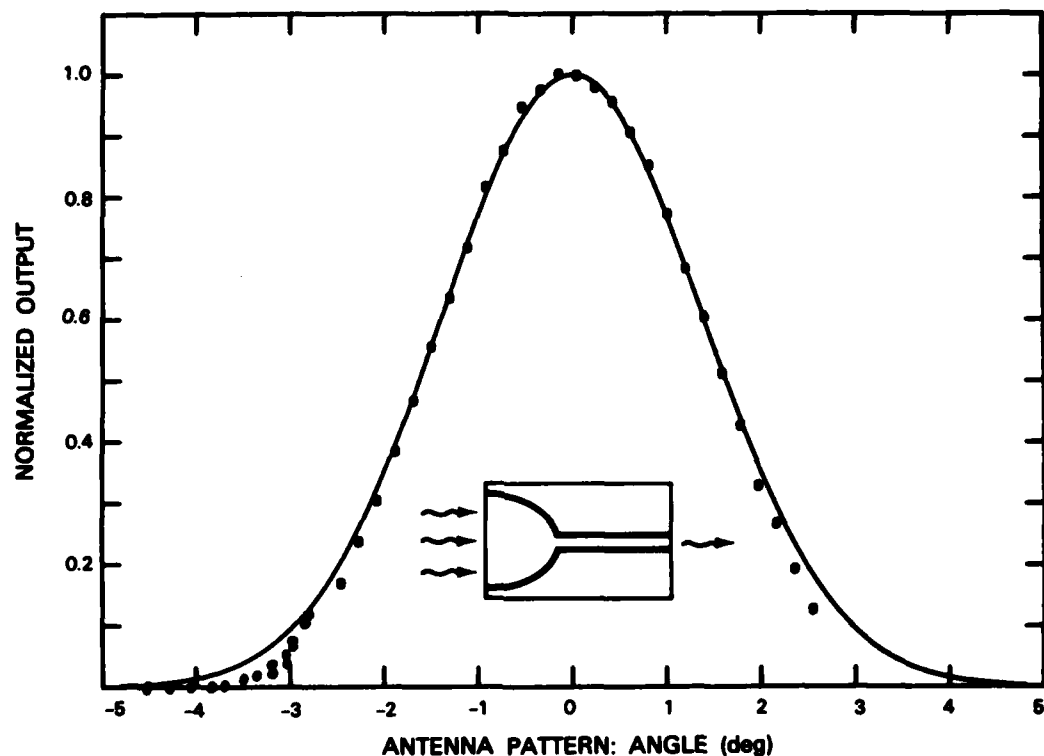
Figure 1-9. *Far-field receiver response for the 20-μm-aperture horn as a function of the incident plane-wave angle compared to the Gaussian far field theoretically predicted from a Gaussian near field with FWHM of 7.6 μm.*

at half maximum (FWHM) of the Gaussian curve in Figures 1-9 and -10 corresponds to a FWHM of a Gaussian near-field mode pattern of 7.6 μm. The near-field pattern and the associated video analyzer data are shown in Figure 1-11. The 8.0-μm FWHM of the near field as determined by the video analyzer data is in good agreement with the far-field measurement. The fact that the 20-μm horn aperture is not fully filled is consistent with theory[20] that relates the spatial size of the fundamental mode to width-to-depth ratio of a waveguide. For the large ratio in our case (≈9), the underfilling of the aperture is expected. These measurements showed that the horns are near adiabatic (that there is negligible conversion from the lowest-order mode excited at the waveguide input to the higher-order modes of the horn) and is consistent with the theory.[17,18]

Data taken with a video analyzer in the direction orthogonal to the wafer plane are shown in Figure 1-12. The results are asymmetric; there is a sharper cutoff at the air interface, as expected. Far-field patterns in this direction are consistent with the near-field data in Figure 1-12.

R.H. Rediker   R.A. Becker
T.A. Lind   L.M. Johnson

10
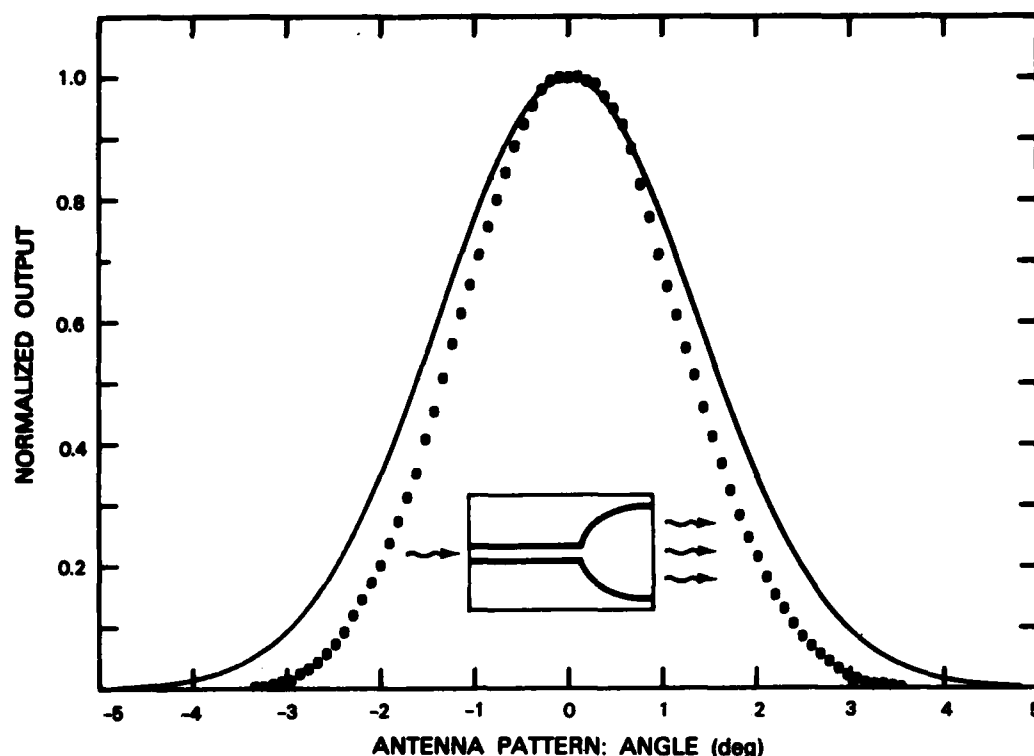
Figure 1-10. Far-field output intensity as a function of angle in the plane of the wafer for a 20-μm-aperture transmitting horn compared to the same Gaussian as in Figure 1-9.

1.4 NONLINEARITIES IN THE I-V CHARACTERISTICS OF InP:Fe OPTOELECTRONIC SWITCHES

Photoconductive switches on semi-insulating (SI) InP have been fabricated for signal-processing applications using a variety of metals alloyed under different conditions in order to investigate nonlinearities observed in the switch I-V characteristics as a function of illumination conditions (light-spot position, uniformity, and intensity). Even when microalloyed multi-metal contact technology is employed, the I-V characteristics of these devices depend strongly on the illumination conditions. These observations have been made not only on InP:Fe but on SI InGaAs, and Cr-doped and undoped GaAs.

The nature of the contact in photoconductive devices formed on SI materials is critical to their performance. Nonohmic contacts can lead to spurious response times,[21] secondary peaks,[22] and nonlinearities.[23] The mid-gap position of the Fermi level in these materials makes it difficult to obtain ohmic contacts. Unalloyed Au contacts, which have been the most frequently reported electrodes on SI photoconductive devices, are not ohmic and have, not surprisingly, led to the observation of numerous unexplained effects.

11

MICROMETERS
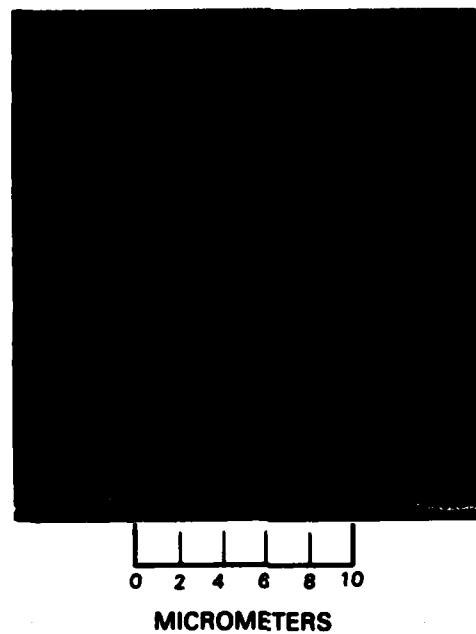
Figure 1-11. Photograph taken from video monitor of near-field output pattern of the 20-μm-aperture horn in the plane of the wafer. The FWHM from the associated video analyzer data is 8 μm.

MICROMETERS
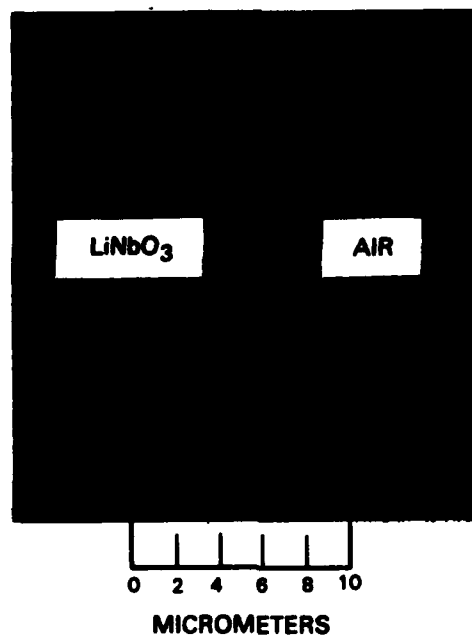
Figure 1-12. Video analyzer data representing the near-field output pattern of the 20-μm-aperture horn in the plane perpendicular to the wafer.

In the course of our investigation of optoelectronic switches fabricated on InP:Fe substrates, we have studied alloyed and unalloyed n-type (NiGeAu, AuSn) and p-type (AuZn, AuMg) contacts using interdigitated electrode patterns with 2-, 4-, and 6-μm finger width and spacing. Figure 1-13 shows a schematic of a 6-μm device with alloyed contacts and the I-V characteristics obtained when a focused He-Ne laser beam spot is swept across the fingers. Clearly, there exist illumination conditions (positions 3, 5, and 7) under which the photocurrent is linear with voltage, and therefore the contact could be said to be ohmic. However, truly ohmic contacts would not lead to the nonlinear behavior observed as a function of the position of the light spot on the switch. Nonlinear I-V curves are also observed when the illumination is purposely made nonuniform and again vary depending on where the brightest region is located on the switch. These effects were observed when both electrodes were p-type or n-type as listed above and were independent of the alloying parameters, which ranged from 400° to 600°C in temperature and 10 to 45 s in time. Nonalloyed contacts behaved similarly, but in addition exhibited a photovoltage that was strongly dependent on the position of the light spot. Photovoltages were generally not present in the alloyed devices.

To characterize further the observed nonlinear behavior, simple single-gap (10-μm) devices were tested and yielded identical results. However, since now the light was clearly near one or the other electrode, it was possible to correlate various effects with light-spot position. With the light spot near the positively biased end of the gap, the nonalloyed switches displayed the I-V characteristics of a photovoltaic device, i.e., a positive voltage and a negative current. Moving the light spot so that it was adjacent to the grounded end of the gap again resulted in the switch displaying a photovoltaic characteristic but of opposite polarity. With a few volts of bias, higher switch conductivity (i.e., a steeper I-V slope) was obtained with the light spot nearer the positively biased (anode), as opposed to the grounded end of the gap.

All the above I-V curves were measured on a standard curve tracer at a sweep rate of 120 Hz. In order to investigate quantitatively the I-V curves at frequencies in the range of potential application, e.g., 250 MHz, the intermodulation (IM) products were measured. This technique[24] determines the output amplitude of various product terms generated by a nonlinearity when two sinusoidal signals are applied to the input. The level of the second-order IM output will be dependent on the degree of symmetry of the I-V characteristic. The data presented in Table 1-1 show that nonuniform illumination can change the level of the second-order terms by 20 to 30 dB while the fundamental and third-order amplitudes change by only 0.3 to 0.4 dB and 4 to 6 dB, respectively. These results confirm that the effects of illumination uniformity on the I-V curve are the same at RF as at lower frequencies. The first pair of entries in Table 1-1 was obtained from switches in which the interdigitated electrodes were both alloyed NiGeAu. Similar results were obtained with other metals. Illuminating the switches with 50-ps light pulses yielded high-frequency pulse amplitude vs voltage curves that followed the low-frequency I-V behavior. The same behavior was obtained on bulk SI GaAs and LPE-grown SI InGaAs, indicating that these effects are not specific to InP but rather are due to the general characteristics of SI material.

13
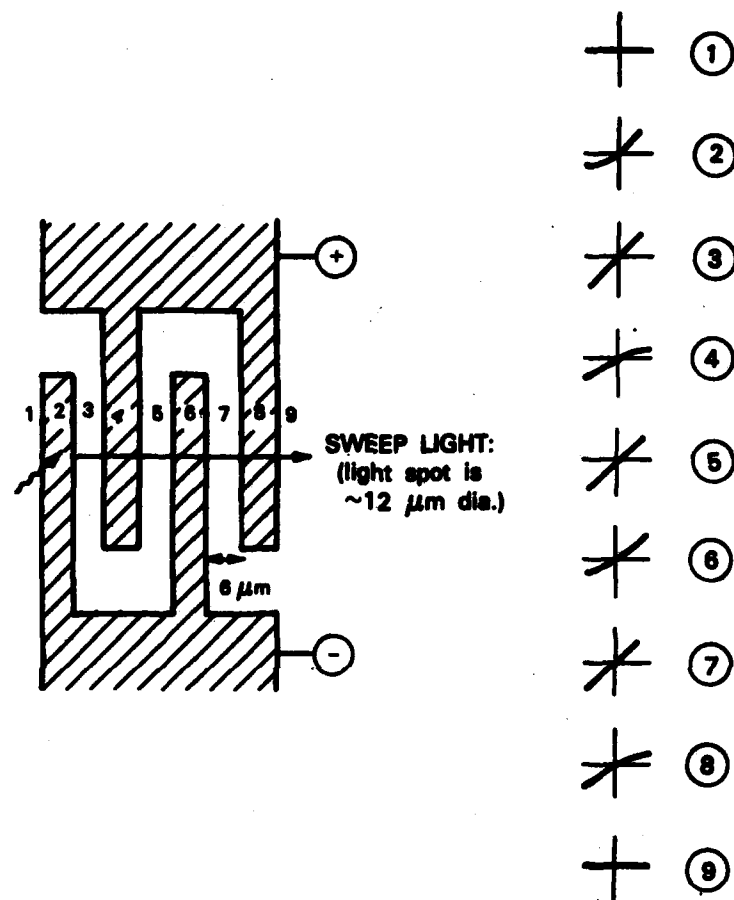
Figure 1-13. I-V characteristic as a function of light-spot position for a 6-μm optoelectronic switch. The interdigitated electrodes were alloyed NiGeAu, but similar results were obtained for other metals and geometries. The numbers next to the I-V curves correspond to the position of the light on the switch.

14

TABLE 1-1
Intermodulation Levels for InP Optoelectronic Switches, Input Frequencies 246.5 and 253.5 MHz

	Fundamental (dB)	2nd (dB)	3rd (dB)
NiGeAu Alloyed Contact			
Uniform	-15.9	>-99.9	-81.7
Nonuniform	-16.3	-64.7	-75.6
p/n Double Contact			ƒ
Uniform	-17.2	-64.5	-66.9
Nonuniform	-17.5	-44.8	-63.1

To investigate these effects, a double p/n contact structure was fabricated, in which both a p- and an n-type contact metal were deposited on each side of the switch. This experiment was suggested by the fact that since the Fermi level is located near the middle of the energy gap in SI materials, there will exist a barrier to either holes or electrons depending on the polarity and the type of metal used. With the double p/n contacts, regardless of the applied polarity, neither carrier type will encounter a potential barrier since the p contact carries only the hole current and the parallel n contact carries only the electron current. The idea was successfully used by Hurwitz[25] in making plasmon-wave density measurements on high-resistivity Ge crystals. The pattern of 2-μm-wide electrodes used in the present study is shown in Figure 1-14. Note that with this contact pattern there still may be an intervening contact finger of the undesired type and polarity; the only effect of this extra finger will be to widen the effective interfinger spacing. The p and n contacts on each side were shorted externally and bias was applied across the switch in the standard fashion. I-V curves obtained with a 6-μm-dia. light spot on these double p/n devices are shown in Figure 1-15 where the light spot was swept from right to left parallel to the fingers (i.e., from the positively biased to the grounded contact). The IM data are shown in the second pair of entries of Table 1-1. It is clear that this behavior is similar to that observed in the single-type electrode devices. These data suggest that the source of the nonlinearity is not charge pile-up at the metal-semiconductor interface. The fact that these effects have been observed in substrate as well as LPE-grown SI photoconductors (InP, GaAs, InGaAs), regardless of the electrode composition or alloying, suggests that it may be related to intrinsic ambipolar effects in these materials, rather than the metallization process or existence of

15

Figure 1-14. Photomicrograph of the double p/n contact structures. The dark-colored electrodes are p-type (alloyed AuZn) and the light-colored ones are n-type (alloyed NiGeAu). The scale is 2 μm/div. In-coated ribbons are bonded to each pad and bias applied across the switch (left side negatively biased).

a simple Schottky barrier. The implication of these observations for the various RF signal-processing applications, such as mixing and sampling, is that the performance may be limited by the degree of uniformity of the illumination used to activate the switch.

V. Diadiuk
C.H. Cox III
F.J. Leonberger
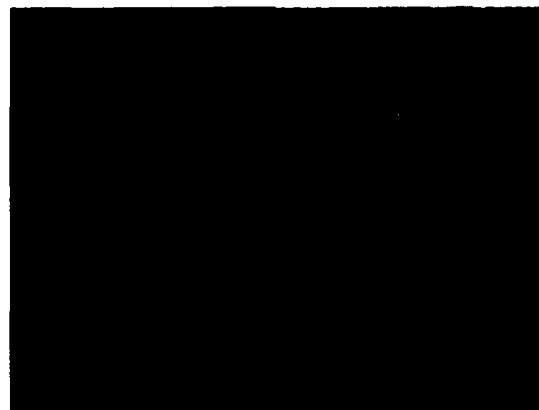
Figure 1-15. I-V characteristics of the double p/n contact switch with the light spot near (a) the anode (right side of Figure 1-14), (b) center, and (c) cathode. Similar results were obtained when the center fingers were p-type.

REFERENCES

1. D.Z. Tsang and J.N. Walpole, IEEE J. Quantum Electron. **QE-19**, 145 (1983).

2. Solid State Research Report, Lincoln Laboratory, M.I.T. (1981:2), p.1, DTIC AD-A110947/9; and D.Z.Tsang, J.N. Walpole, S.H. Groves, J.J. Hsieh, and J.P. Donnelly, Appl. Phys. Lett. **38**, 120 (1981).

3. D.Z. Tsang, J.N. Walpole, and Z.L. Liau, IEEE Trans. Electron Devices **ED-30**, 1596 (1983); and Solid State Research Report, Lincoln Laboratory, M.I.T. (1983:3), p. 11.

4. D.Z. Tsang, J.N. Walpole, Z.L. Liau, and S.H. Groves, 4th Intl. Conf., Integrated Optics and Optical Fiber Communication (IOOC '83), Postdeadline Technical Digest, Tokyo, Japan, 27-30 June 1983, paper 29B5-6.

5. Z.L. Liau and J.N. Walpole, Appl. Phys. Lett. **40**, 568 (1982); IEEE Trans. Electron Devices **ED-29**, 1675 (1982).

6. R.H. Kingston, Appl. Phys. Lett. **34**, 744 (1979).

7. V. Diadiuk, S.H. Groves, D.Z. Tsang, and J.N. Walpole, IEEE Trans. Electron Devices **ED-30**, 1608 (1983).

8. Y. Ohmachi and J. Noda, Appl. Phys. Lett. **27**, 544 (1975).

9. F. Auracher and R. Keil, Wave Electronics **4**, 129 (1980).

10. F.J. Leonberger, Opt. Lett. **5**, 312 (1980).

11. K. Iwasaki, S. Kurazano, and K. Itakuna, Jpn. Electron. Commun. **58-C**, 100 (1975).

12. H.A. Haus and C.G. Fonstad, Jr., IEEE J. Quantum Electron. **QE-17**, 2321 (1981).

13. J.P. Donnelly, N.L. DeMeo, and G.A. Ferrante, J. Lightwave Tech. **LT-1**, 417 (1983).

14. E.A.J. Marcatili, Bell Syst. Tech. J. **53**, 697 (1974).

15. F.J. Leonberger, J.P. Donnelly, and C.O. Bozler, Appl. Phys. Lett. **28**, 616 (1976).

16. J.P. Donnelly, F.J. Leonberger, and C.O. Bozler, Appl. Phys. Lett. **28**, 206 (1976).

17. W.K. Burns, A.F. Milton, and A.B. Lee, Appl. Phys. Lett. **30**, 28 (1977).

18. A.F. Milton and W.K. Burns, IEEE J. Quantum Electron. **QE-13**, 828 (1977).

19. W.K. Burns, P.H. Klein, E.J. West, and L.E. Plew, J. Appl. Phys. **50**, 6175 (1975).

20. S.K. Korotky, W.J. Minford, L.H. Buhl, M.D. Devino, and R.C. Alferness, IEEE J. Quantum Electron. **QE-18**, 1796 (1982).

21. P.M. Downey, D.H. Auston, and P.R. Smith, Appl. Phys. Lett. **42**, 215 (1983).

22. P.K. Bharadwej, R.F. Code, H.M. van Driel, and E. Walentynowicz, Appl. Phys. Lett. **43**, 207 (1983).

23. K. Li, E. Rezek, and H.D. Law, Proc. SPIE **439**, 105 (1983).

24. E.W. Pappenfus, W.B. Bruene, and E.O. Schoenike, *Single Sideband Principles and Circuits* (McGraw-Hill, New York, 1964), pp. 179-182.

25. C.E. Hurwitz and A.L. McWhorter, Phys. Rev. **134**, A1033 (1964).

2. QUANTUM ELECTRONICS

2.1 Na PROFILES IN SiO₂ FILMS BY FLUORESCENCE INDUCED DURING REACTIVE-ION ETCHING

The performance of MOS devices is severely degraded by the presence of mobile alkali ions in concentrations in excess of $\sim10^{15}$ cm^{-3} in oxide films. Numerous techniques have been developed to reduce the total mobile ion concentration below this level and to spatially confine these species to minimize drifting under bias. There remains a need for a simple, sensitive, diagnostic technique for determining mobile ion concentrations and profiles in SiO₂ films grown for device applications. Ideally, the diagnostic technique should: (a) allow for rapid analysis of wafers to provide near-real-time information when trying to ascertain the source of contamination, (b) provide high spatial resolution, both in depth and in lateral dimensions, and (c) provide a minimum detectable concentration limit below the levels deleterious to device performance.

We report on the detection and depth profiling of Na concentrations in SiO₂ films thermally grown on Si substrates by monitoring the Na fluorescence induced during reactive-ion and sputter etching in a simple parallel-plate triode reactor. Fluorescence from atomic species sputtered from surfaces by energetic ion and neutral bombardment is a well-known phenomenon; there have been numerous measurements and discussions of the effect and of its use for materials analysis.[1] Detection sensitivities of $\sim10^{15}$ cm^{-3} (~0.1 ppm) are reported here using a very simple experimental arrangement, having measurement times of <4 min. for a 100-nm-thick oxide. Simultaneous monitoring of the reflectivity of the SiO₂-Si wafer with a He-Ne laser probe provides a real-time measurement of the oxide thickness for depth profiling. The relatively low energy ion, neutral and electron bombardment characteristic of the RF-excited reactive-ion etching environment minimizes the redistribution of the mobile ion species within the oxide during the measurement. Substantial improvements in the sensitivity and the lateral resolution can be expected with improvements in the experimental system.

The 9-cm-dia. reactor consisted of three stainless-steel electrodes separated by cylindrical fused-quartz vacuum walls. The reactor configuration is shown schematically in Figure 2-1. A 13.56-MHz RF discharge was maintained between the grounded top electrode and a middle electrode (constructed of fine mesh screening). Samples were placed on the lower, DC-biased, electrode. This triode configuration allowed control over both the reactive radical concentrations and the ion bombardment energy. Typically, the etching gas was CF₄ and the SiO₂ etch rate was 25 to 50 nm/min. Qualitatively similar results, but with widely differing SiO₂ etch rates, were obtained with other gases such as Ar, N₂ and SF₆.

The Na emission at 589 nm, which was clearly visible from both NaCl samples and deliberately heavily contaminated (surface concentrations of 10^{13} cm^{-2}) SiO₂ films, was observed to be localized just above the sample surface. This is readily understood from
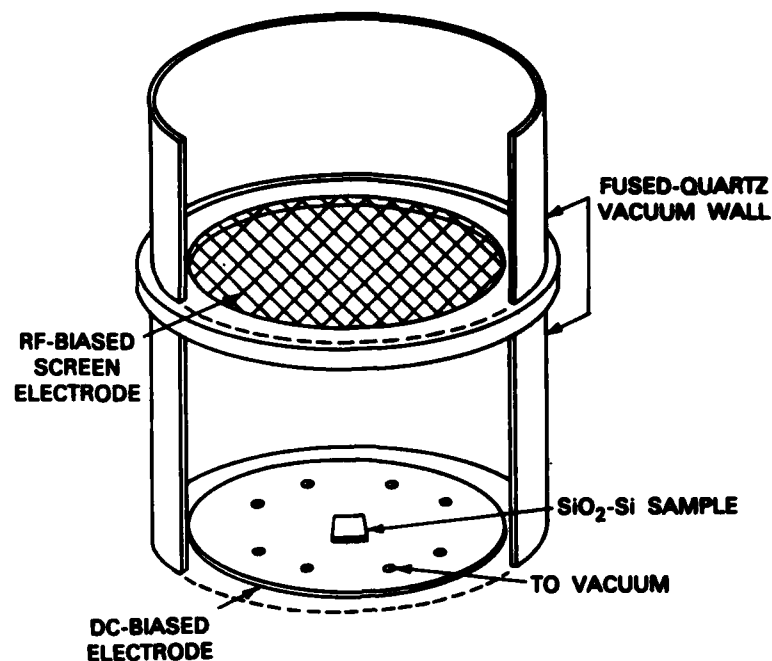
Figure 2-1. The reactor and biasing arrangement used for the detection of Na-atom fluorescence during reactive-ion etching of SiO_2-Si wafers.
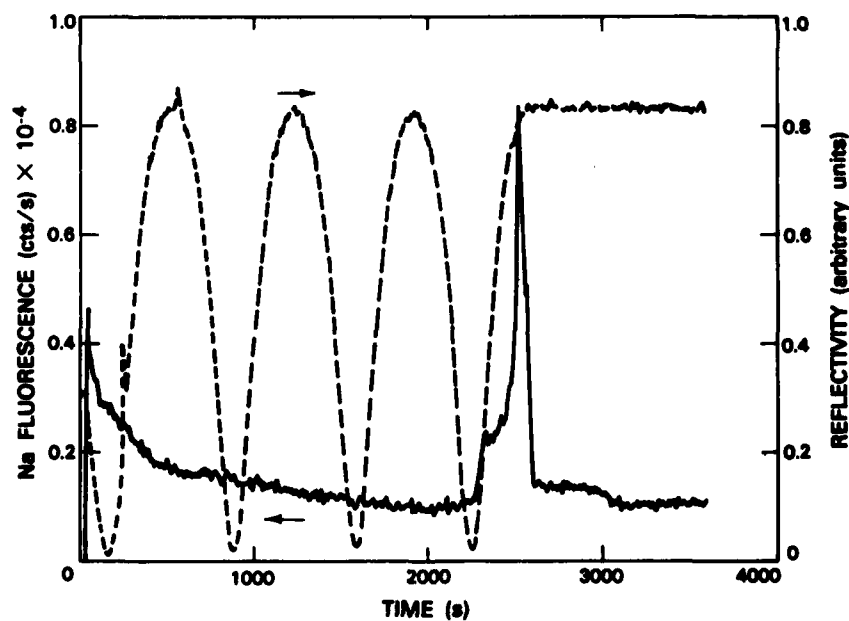
Figure 2-2. Na fluorescence signal during etching of a 1-μm-thick oxide on Si. Note the increase in the fluorescence signal near the oxide-Si interface. Also shown is the intensity of a He-Ne laser beam reflected from the wafer during the etching. Periodic changes in the reflected signal are due to interference effects as the oxide thickness decreases. The oxide is completely removed when the reflectivity reaches a steady-state value.

the near thermal mean kinetic energy of sputtered Na atoms and the Na radiative lifetime of 13 ns, implying that the radiating atoms are within 40 μm of the surface. The detection optics were arranged to collect the fluorescence emitted parallel to the film surface. This geometry had the additional advantage of minimizing the collection of background light emitted from the plasma discharge. The fluorescence was analyzed with a 1/4-m spectrometer and detected with a cooled photomultiplier using photon-counting electronics.

Sensitivities to surface Na concentrations of $\sim 10^{10}$ cm^{-2} were obtained, which correspond to an average Na concentration of 10^{15} cm^{-3} uniformly distributed throughout the oxide. This sensitivity was limited by a sputter-induced fluorescence background from the stainless-steel electrode and sample mounting platform. This fluorescence was visually apparent as a diffuse yellow-orange glow extending approximately 1 to 2 cm from the electrode surfaces at a DC-bias voltage of 1.5 kV. A typical Na concentration profile which exhibits a low level of Na atoms, near the detection limit of the experiment, in the bulk of the oxide, with higher concentrations at both the oxide surface and the SiO_2-Si interface, is shown in Figure 2-2. The surface Na signal was dependent on the treatment of the sample and, as expected, was sensitive to deliberate contamination introduced by dipping the wafers in NaOH solutions. In contrast, the signal at the SiO_2-Si interface, while it depended on the wafer, was relatively insensitive to the surface contamination. Experiments are currently under way to investigate the dependence of this signal on the ion energy and to attempt to separate the components resulting from mobile ion drift due to charging effects during the etching and from actual Na contamination at the interface.

S.R.J. Brueck
S.W. Pang
T.F. Deutsch

2.2 LASER-INITIATED CHEMICAL VAPOR DEPOSITION OF TUNGSTEN FILMS

The deposition of refractory metal films is of interest for the fabrication of low-resistance interconnects and contacts for semiconductor devices. Chemical vapor deposition (CVD) of tungsten over SiO_2 requires temperatures in excess of 700°C; at lower temperatures deposition is difficult and films, when obtained, generally have poor adhesion. We have used ArF excimer laser radiation to initiate low-temperature (<500°C) CVD deposition of W films on SiO_2 and have obtained adherent, low-resistivity films under conditions where films could not be produced without laser initiation.

The deposition chamber was a stainless-steel cross capable of accepting 2-in.-dia. wafers. The substrates were mounted on a stainless-steel pedestal, which contained a heater element capable of producing substrate temperatures of 500°C. The 193-nm ArF laser was operated at 50 Hz and produced average powers of 4 to 7 W. A beam-reducing telescope was used to produce a collimated beam which passed about 1 mm above the substrate. WF_6 and H_2 were fed through mass flow controllers, mixed near the chamber, and introduced through a nozzle above the substrate. A H_2 flow of 100 sccm (standard cubic centimeter per minute)
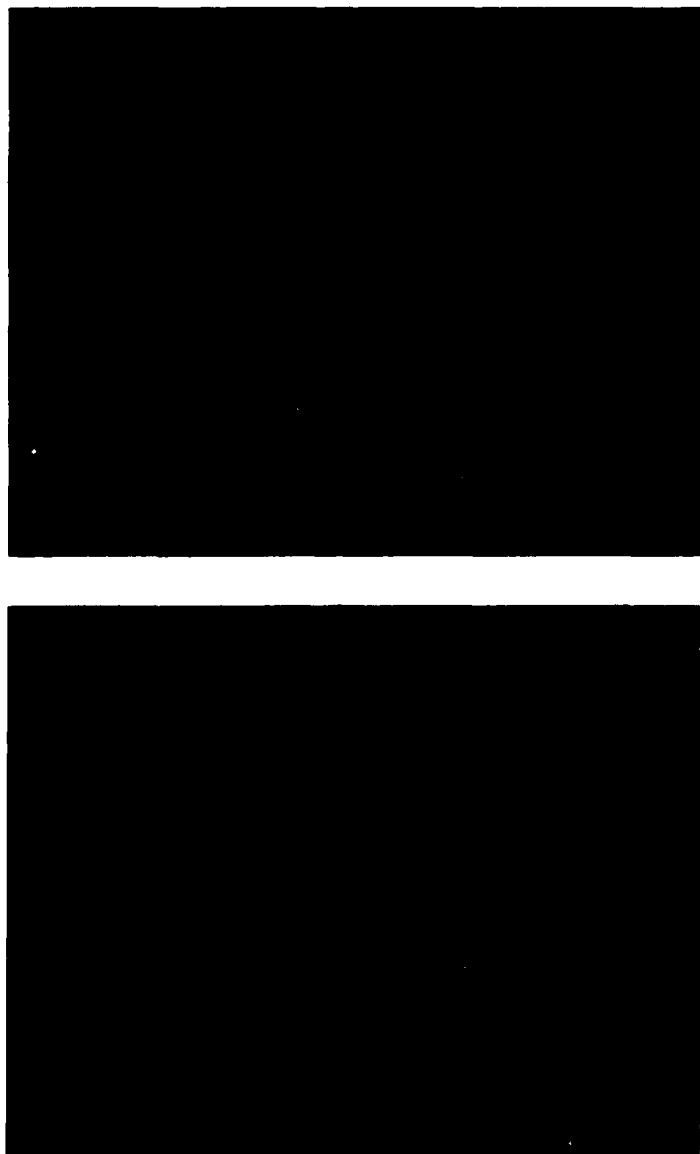
Figure 2-3. SEM micrographs showing a side and top view of a W film over SiO_2 steps on a Si substrate. Conditions: ArF laser irradiation, WF_6-H_2 mix, 285°C.

and a WF_6 flow of 2.1 sccm were used; typical total chamber pressure was 8 Torr. Substrates were Si wafers and Si covered with 460 nm of thermal SiO_2. In some cases SiO_2 films were patterned with gratings in order to examine conformal coverage.

Without laser irradiation W deposition did not occur on SiO_2 at temperatures up to 400°C; similar results have been observed by others.[2] With laser irradiation shiny metallic films were obtained at temperatures as low as 240°C; however, only films deposited at 440°C passed the adhesive tape test for adherence. Figure 2-3 shows two scanning electron microscope (SEM) micrographs illustrating the excellent conformal coverage and the surface morphology of W films deposited at 285°C over SiO_2 steps on Si.

Figure 2-4 shows the temperature dependence of the W deposition rate on Si or SiO_2 using ArF laser radiation, as well as the thermal deposition rate on Si substrates. The activation energy obtained for the thermal reaction, ~18 kcal/mole, is in reasonable agreement with the value of 16 kcal/mole found by others.[3] The effect of laser irradiation is to reduce
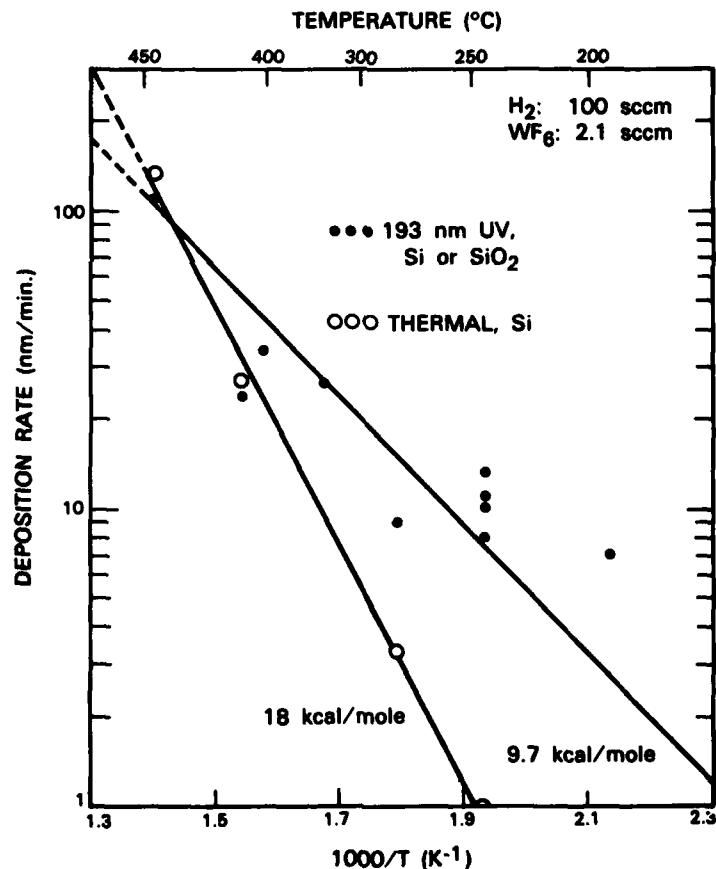
Figure 2-4. Temperature dependence of the deposition rate for thermal and for laser-initiated W film deposition. Conditions: 100 sccm H_2, 2.1 sccm WF_6.

25

the activation energy for the reaction to about 9.7 kcal/mole, increasing the deposition rate on Si for temperatures in the 200° to 300°C range significantly, and allowing deposition on SiO_2.

Sheet resistivity measurements were performed using a four-point probe, and film thickness was determined by Dektak profilometer measurements of etched films. Figure 2-5 shows that film resistivity is a strong function of deposition temperature. At 440°C a resistivity of 17 $\mu\Omega$-cm, about three times the bulk value of 5.3 $\mu\Omega$-cm, was obtained for a laser-deposited film on SiO_2; a thermally deposited film on Si had a resistivity of 8 $\mu\Omega$-cm.

The dependence of film resistivity on both deposition temperature and subsequent thermal annealing can be understood in terms of the film microstructure produced. Tungsten can exist both in the stable α-W phase and in the metastable β-W phase. Studies on sputtered and evaporated[4] films have shown that β-W phase films consist of small crystallites, 5 to 10 nm in diameter, with a high density of stacking faults and twins, while α-W films consist of large crystallites, 150 to 250 nm in diameter, free of structural defects. The high resistivity (100 to 300 $\mu\Omega$-cm) of β-W films has been attributed to diffuse scattering of electrons by grain boundaries.
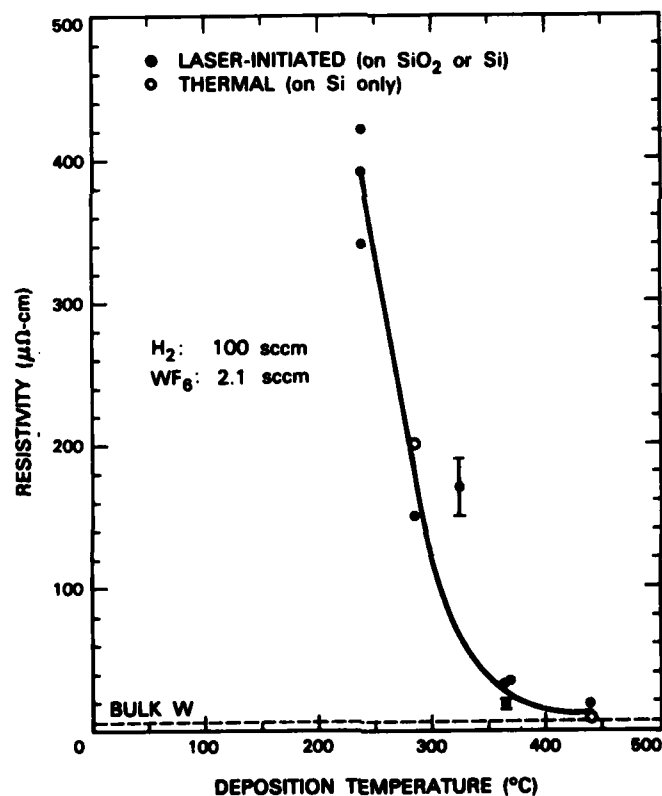
Figure 2-5. W film resistivity as a function of deposition temperature for both thermal and laser-deposited films.

X-ray diffraction measurements on W films laser-deposited on SiO_2 substrates at three different substrate temperatures showed that the structure changes from β-W to α-W as the temperature is increased from 330° to 440°C. This change of crystal structure, with the accompanying change in crystallite dimension discussed above, is responsible for the sharp decrease in resistivity with deposition temperature seen in Figure 2-5.

The chemistry of the conventional CVD of W films may be summarized by the overall reaction,

$$WF_6 + 3\ H_2 \rightarrow W + 6\ HF \quad . \tag{2-1}$$

The activation energy for the deposition reaction, 16 kcal/mole, has been identified with the dissociation of adsorbed H_2 molecules on the surface under conditions where the reaction is not mass-transport limited.[3] In the case of laser initiation the initial step is probably dissociation of WF_6 by the 193-nm radiation to release at least one or more F atoms and produce radicals of the form WF_n (n = 1 - 5). The reaction

$$H_2 + F \rightarrow HF + H \quad , \tag{2-2}$$

which is 31.9 kcal/mole exothermic, can then occur. The hydrogen atoms can react with WF_6 and WF_n radicals via a complex series of reactions to deposit W and produce HF. Thus ArF laser radiation can serve to change the reactions involved.

In conclusion, ArF laser radiation can be used to deposit low-resistivity W films on SiO_2 at temperatures at which deposition is otherwise not observed. The low temperatures required for the laser-initiated deposition process and the excellent conformal coverage demonstrated here make this process useful for both discrete device fabrication and the production of films suitable for fabrication into low-resistivity interconnects.

<div align="right">

T.F. Deutsch
D.D. Rathman

</div>

REFERENCES

1. For a recent review see G.E. Thomas, Surf. Sci. **90**, 381 (1979).

2. T. Moriya, S. Shima, Y. Hazuki, M. Chiba, and M. Kashiwagi, 1983 International Electronic Device Meeting (IEDM) Technical Digest, p. 550 (1983).

3. W.A. Bryant, J. Electrochem. Soc. **125**, 1534 (1978).

4. A.K. Sinha, T.E. Smith, T.T. Sheng, and N.N. Axelrod, J. Vac. Sci. Technol. **10**, 436 (1973).
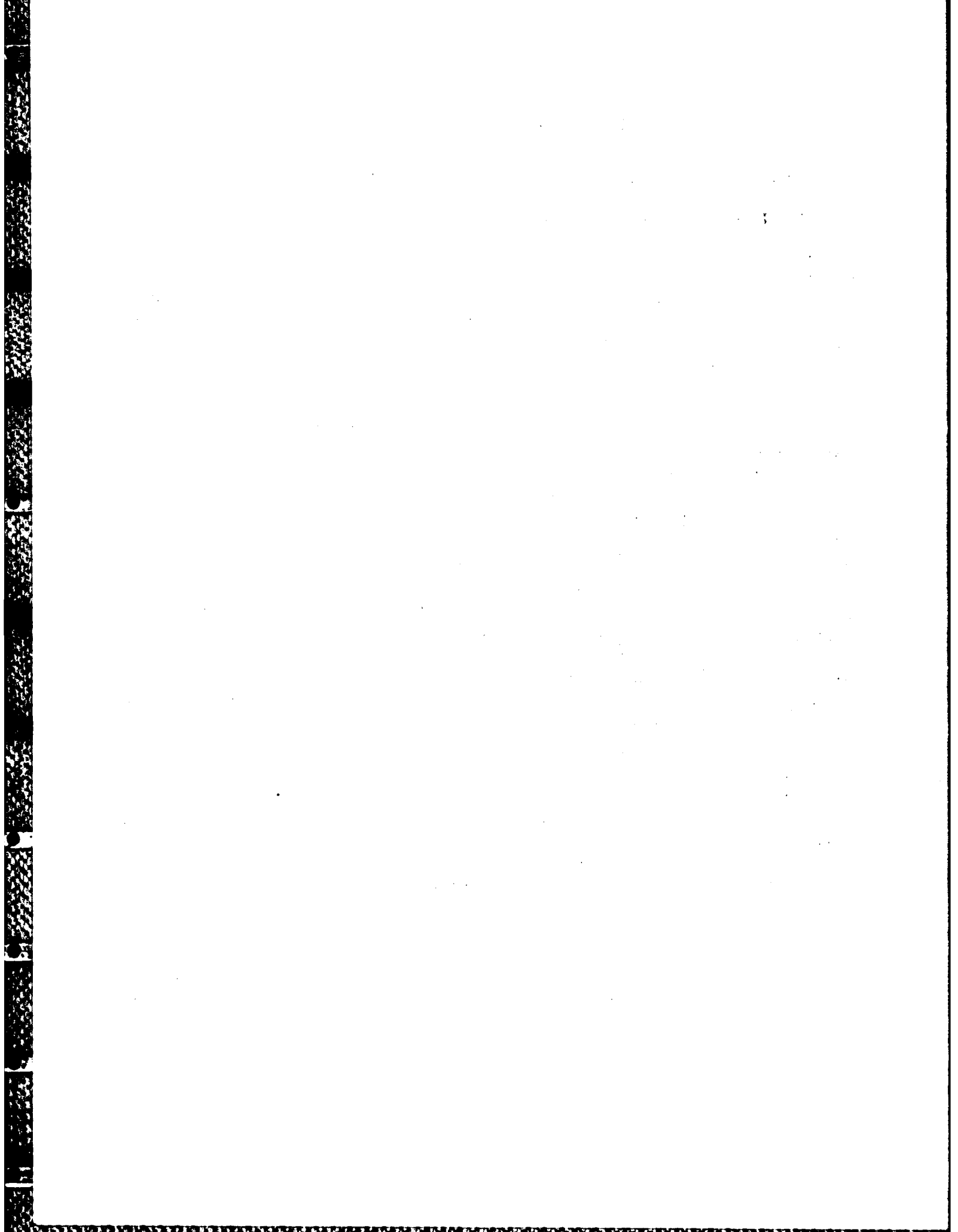
3. MATERIALS RESEARCH

3.1 ZONE-MELTING-RECRYSTALLIZED Si-ON-INSULATOR FILMS

3.1.1 Effects of Ionizing Radiation on CMOS Devices

We have previously described[1-3] a graphite-strip-heater technique for obtaining large-area, high-quality Si films on SiO_2-coated Si substrates by zone-melting recrystallization (ZMR). We have also reported[4] an initial study of the effects of ionizing radiation on CMOS devices fabricated in such silicon-on-insulator (SOI) films. In that study it was found that applying a bias voltage V_B of –5 V to the Si substrate during irradiation and measurement greatly reduced the effect of radiation on the subthreshold leakage current of n-channel SOI/MOSFETs without producing a significant increase in the leakage current of p-channel devices. If the gate voltage V_G was positive, however, n-channel devices exhibited a large increase in leakage current after a total dose of 10^6 rad(Si), and the threshold voltage of these devices decreased sharply for total doses above 10^4 rad(Si). By making a number of changes in device design and fabrication procedure, including a reduction in the thickness of the gate oxide to only 10 nm, we have substantially improved the radiation hardness of the SOI/CMOS devices. For V_B = –5 V, both n- and p-channel devices now exhibit low subthreshold leakage, small threshold voltage shifts, and very little transconductance degradation for total radiation doses up to 10^7 rad(Si).

The CMOS devices, which were fabricated in 0.5-μm-thick ZMR films, have a poly-Si gate and self-aligned ion-implanted source and drain. The gate width is 45 μm, the gate length is 3.5 μm. Before irradiation, the individual n- and p-channel devices were well behaved, with field-effect mobilities of ~550 and 180 cm^2/V-s for electrons and holes, respectively, and subthreshold leakage currents of <0.1 and 0.5 pA/μm (channel width), respectively. For more than 100 devices tested the yield exceeded 98 percent and the characteristics of the working devices were quite uniform.

The MOSFETs were mounted in 24-pin ceramic packages without covers and irradiated with a beam of 1.5-MeV electrons from a Van de Graaff generator. The electron doses ranged from 2×10^{12} to 2×10^{14} cm^{-2}, corresponding to ionizing doses from 10^5 to 10^7 rad(Si). In order to minimize gate oxide instability due to hot-electron injection, operating voltages of 3 V were used. The bias voltages during irradiation were: V_G = +3, 0 or –3 V; drain voltage V_D = 0, +3 (for n-channel devices) or –3 V (for p-channel devices); and V_B = 0, –5, –8 or –10 V. The device body (or channel) was left floating. Subthreshold leakage current, threshold voltage, and transconductance measurements were performed within 20 min. after exposure. In all cases the V_B value was the same during the measurements as during irradiation.

For devices with V_B = 0, large n-channel leakage currents ($>10^{-8}$ A) were observed after irradiation to doses of 10^6 rad(Si) or above, while there was no increase in p-channel leakage current. For V_B = –8 or –10 V, on the other hand, after irradiation the n-channel leakage current remained low but the p-channel leakage current was 2 to 3 orders of magnitude

29

higher than for $V_B = 0$. Best results were obtained with $V_B = -5$ V. Figure 3-1 shows the subthreshold characteristics of n- and p-channel devices biased with $V_D = 0$ V and $|V_G| = 3$ V during irradiation. The measurements were made with $V_D = 3$ and -3 V for the n- and p-channel devices, respectively. Leakage currents of <0.2 pA/μm (channel width) were observed for both types of devices up to 10^7 rad(Si). With increasing dose the leakage currents for n-channel devices increase slightly, whereas those for p-channel devices decrease. These changes are attributed to hole trapping at the lower Si-SiO$_2$ interface. Similar leakage currents have been measured for devices biased with $|V_D| = 3$ V and $|V_G| = 0$ or 3 V during irradiation.
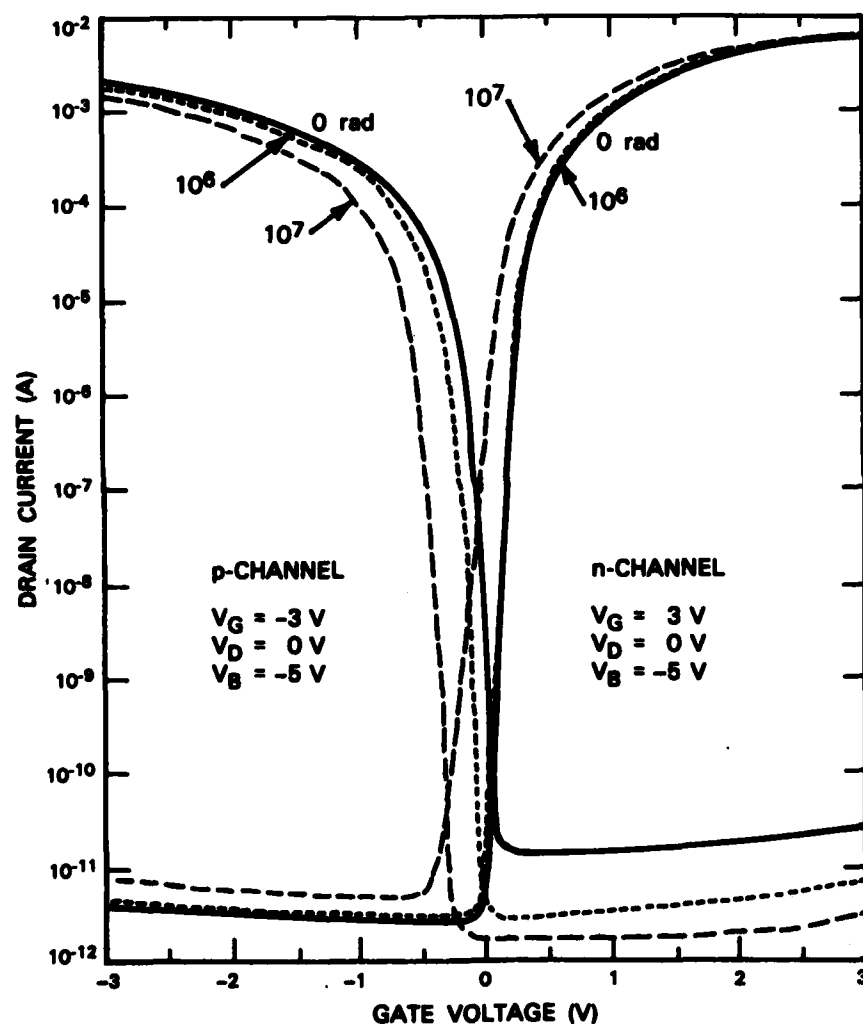
Figure 3-1. Subthreshold characteristics of n- and p-channel SOI/MOSFETs before and after irradiation. Bias voltages during irradiation are shown.

30

Another effect of ionizing radiation is a shift of threshold voltage (ΔV_T) due to charge trapping in the gate oxide and generation of interface states at the gate-oxide/Si interface. In Figure 3-2, ΔV_T for V_B = –5 V is plotted as a function of ionizing dose. For n- and p-channel devices the values of V_T are <–0.04 and <–0.10 V, respectively, after 10^6 rad(Si); these values are <–0.18 and <–0.46 V, respectively, after 10^7 rad(Si). In general, positive gate biasing produces a larger ΔV_T than zero or negative gate biasing. This result is consistent with the generally accepted hole trapping model,[5] according to which holes produced in the gate oxide by the radiation are repelled toward the gate-oxide/Si interface by a positive gate bias and are then trapped near the interface. For n-channel devices, V_T can also be affected by charge trapping at the lower SiO_2-Si interface,[6] but the negative substrate bias practically eliminates this effect.

The generation of interface states by high doses of ionizing radiation frequently causes mobility degradation and reduction of channel transconductance. For the SOI/CMOS devices, however, the transconductance degradation was <5 percent even for a total dose of 10^7 rad(Si), as illustrated in Figure 3-3 for n-channel devices. The generation of interface states is generally believed to be a consequence of hole transport and trapping near the gate-oxide/Si interface.[7-9] In the present devices, it appears that the number of interface states generated is small because only a small number of holes are induced in the thin gate oxide.

B-Y. Tsaur G.W. Turner
R.W. Mountain J.C.C. Fan
C.K. Chen C.H. Anderson, Jr.

3.1.2 Vertical Bipolar Transistors

In the development of SOI technology an important objective is the fabrication of high-performance bipolar and merged CMOS-bipolar integrated circuits. The merged circuits are particularly attractive for many applications because they combine high-speed digital MOS capability with high-performance bipolar analog capability on the same chip.[10] In addition to allowing convenient integration of CMOS and bipolar devices, the SOI structure should permit higher packing density without latch-up and also higher speed performance. To realize these advantages it is necessary to develop a process for producing fully isolated, vertical bipolar transistors in SOI films. We report here the first fabrication of such transistors (specifically, n-p-n devices) in such films prepared by zone-melting recrystallization (ZMR). Previously, lateral bipolar transistors have been fabricated[11,12] in films of this type, and vertical bipolar transistors have been fabricated in SOI films prepared by high-dose oxygen implantation.[13]

The SOI structures used for device fabrication consist of a 1-μm-thick ZMR Si film on a SiO_2-coated Si substrate. A conventional planar LOCOS process was used for device isolation. The base was formed by B^+ ion implantation and thermal annealing. The emitter was formed by low-temperature diffusion from a doped poly-Si film, a technique similar to the
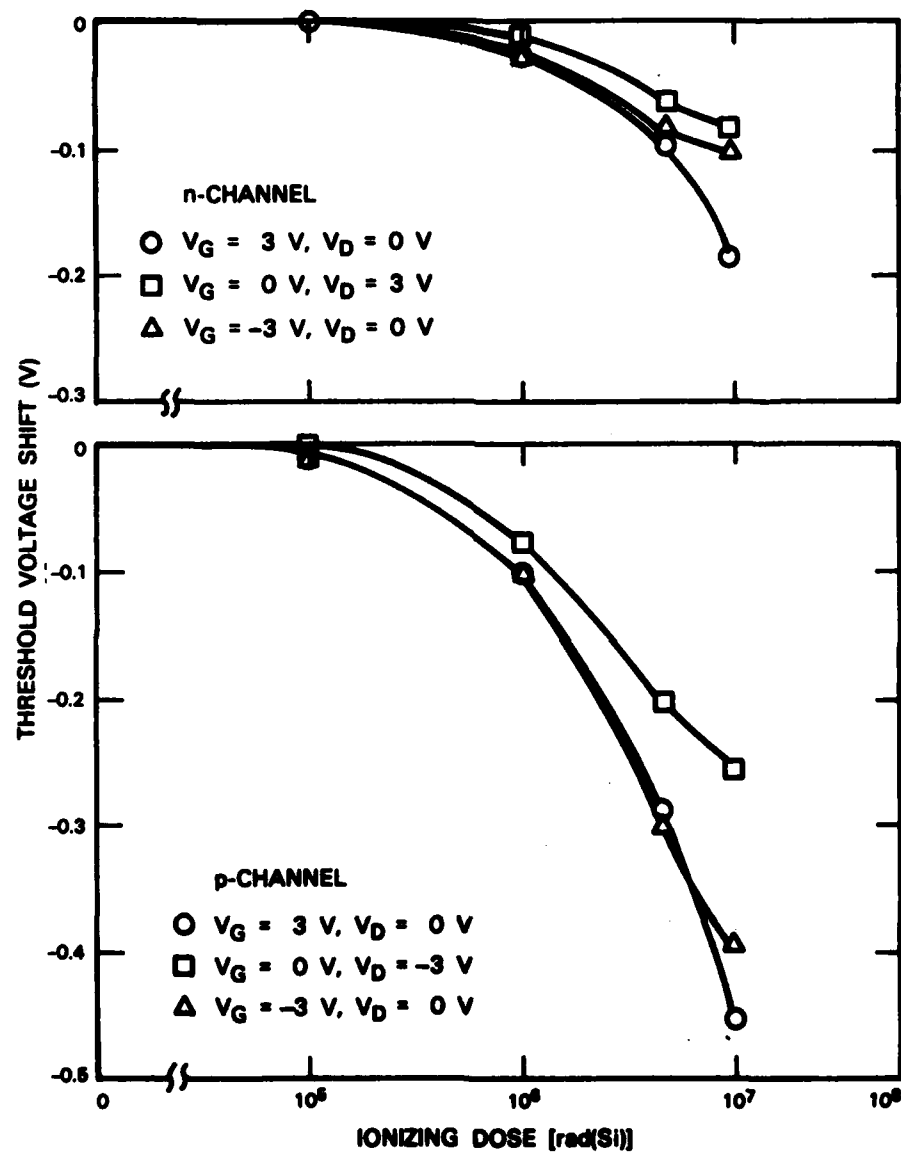
Figure 3-2. Threshold voltage shifts for n- and p-channel devices as a function of ionizing dose. Bias voltages during irradiation are shown.

32

(a)
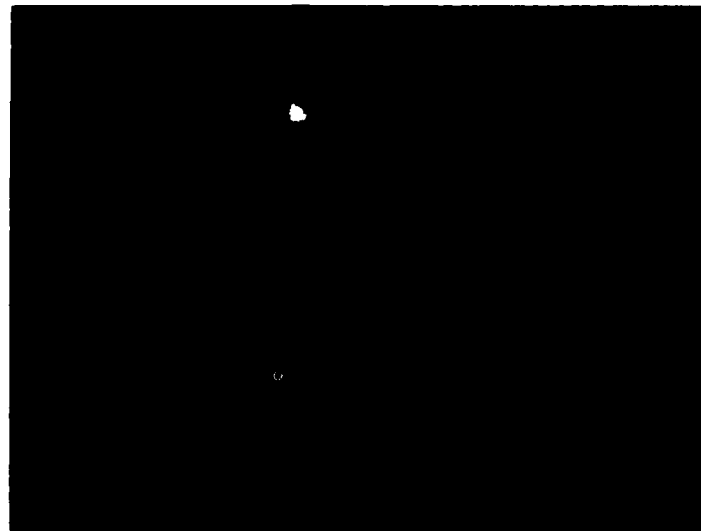
(b)

Figure 3-3. Transistor characteristics for n-channel MOSFETs (a) before and (b) after irradiation to a dose of 10^7 rad(Si). Bias voltages during irradiation were $V_G = 3$ V and $V_D = 0$ V.

33
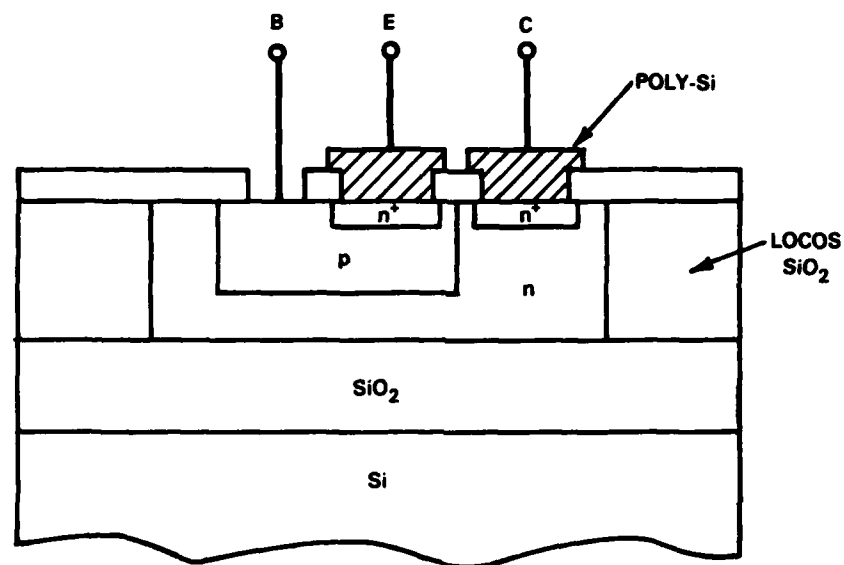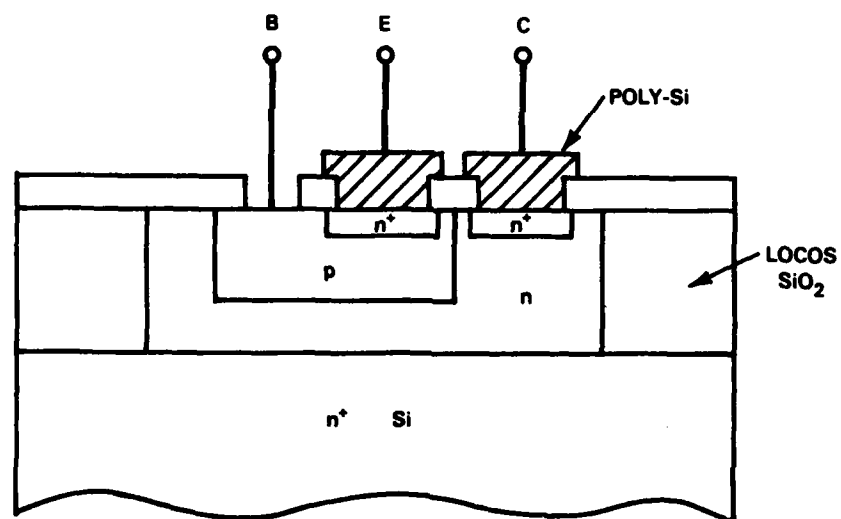
Figure 3-4. Schematic diagrams of vertical bipolar transistors. (a) SOI device, (b) bulk device.

141881-N

one whose use in the fabrication of advanced bulk bipolar devices has been reported previously.[14] For comparison, similar bulk devices were fabricated in single-crystal Si films grown on n^+ Si substrates. Figure 3-4 shows the schematic structures of the SOI and bulk devices.

The use of a poly-Si emitter greatly reduces emitter-collector shorting even for base widths of only 0.2 to 0.3 μm. The V_{EBO} for the SOI transistors is 8 to 10 V. This value, which is comparable to the value for bulk devices, indicates good emitter-base junction quality. The V_{CBO} for the SOI devices is over 50 V, considerably higher than the value of ~30 V obtained for the bulk devices. The increase in collector breakdown voltage for the SOI devices is attributed to the presence of the SiO_2 layer underneath the collector region. For bulk devices the collector breakdown is governed primarily by the punch-through of the collector space-charge region into the heavily doped n^+ Si substrate. In the SOI structure the entire Si film beneath the collector-base junction becomes depleted, forcing field lines to be terminated in the SiO_2 layer.

Figure 3-5 shows typical transistor I-V characteristics for the SOI and bulk devices. Common-emitter current gains of more than 100 have been measured for the SOI devices, comparable to those for the bulk devices. The V_{CEO} is higher for the SOI devices than for the bulk devices. Because of the higher collector resistance of the SOI transistors, the increase in collector saturation current with increasing base current is not as rapid for these devices as for the bulk devices. Thus, the collector currents for $V_{CE} = 4$ V and $I_B = 10$ μA were ~20 percent smaller for the SOI transistors than for bulk devices. Using a buried collector layer would increase the current capability of the SOI transistors, but even their present characteristics are adequate for some linear-circuit applications. These bipolar devices should be easily integrated with the high-performance CMOS devices that have been successfully fabricated in ZMR SOI films.

B-Y. Tsaur   C.K. Chen
R.W. Mountain   J.C.C. Fan

3.2 AlGaAs DOUBLE-HETEROSTRUCTURE DIODE LASERS FABRICATED ON A MONOLITHIC GaAs/Si SUBSTRATE

For numerous applications of integrated circuits it will be advantageous, and in many cases essential, to utilize electronic/optoelectronic systems that employ both Si and GaAs-based circuits. For example, GaAs/GaAlAs optoelectronic interface units could provide high-data-rate optical links to replace wire interconnects between Si VLSI subsystems. While it is possible to take advantage of the complementary capabilities of the two material technologies by using hybrid circuits composed of devices on separate Si and GaAs wafers, it would be even more beneficial to utilize circuits that combine both types of devices fabricated on a single monolithic GaAs/Si (MGS) substrate.

Attempts to prepare usable MGS substrates by growth of GaAs epilayers directly on Si wafers have not been successful. Such growth has not yet yielded high-quality layers, both

(a)
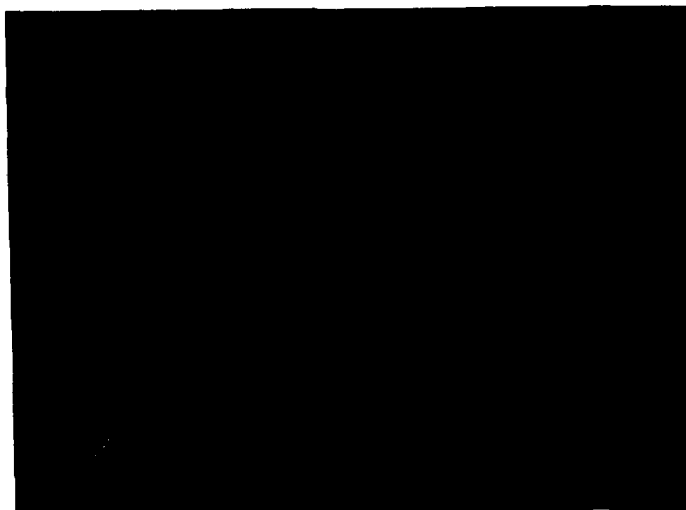
(b)

Figure 3-5. Common-emitter I-V characteristics of vertical bipolar transistors. (a) SOI device, (b) bulk device.

36

because nucleation is difficult and because the two materials differ greatly in their lattice constants and thermal expansion coefficients. However, GaAs shallow-homojunction solar cells[15] and light emitting diodes[16] have been fabricated on MGS substrates prepared by growing GaAs layers on Si wafers coated with a nucleating epilayer of Ge. In addition, MGS GaAs MESFETs have recently been fabricated in our laboratory on similar substrates.[17] We report here the fabrication of the first MGS AlGaAs double-heterostructure diode lasers.

The design of the MGS diode lasers, which are oxide-defined stripe geometry devices, is shown schematically in Figure 3-6. A p^+ Si wafer, oriented $2°$ off $\{100\}$ toward the $\langle110\rangle$ direction, was coated with a thin (~1500 Å) Ge film. The following layers were then grown by MBE: a 1.0-μm n^+ GaAs buffer layer, a 2.0-μm n^- $Al_{0.32}Ga_{0.68}As$ confining layer, a 0.25-μm nominally undoped $Al_{0.1}Ga_{0.9}As$ active layer, a 1.0-μm p^- $Al_{0.32}Ga_{0.68}As$ confining layer, and a 0.25-μm p^+ GaAs cap layer. Si and Be were used as the n- and p-type dopants, respectively.
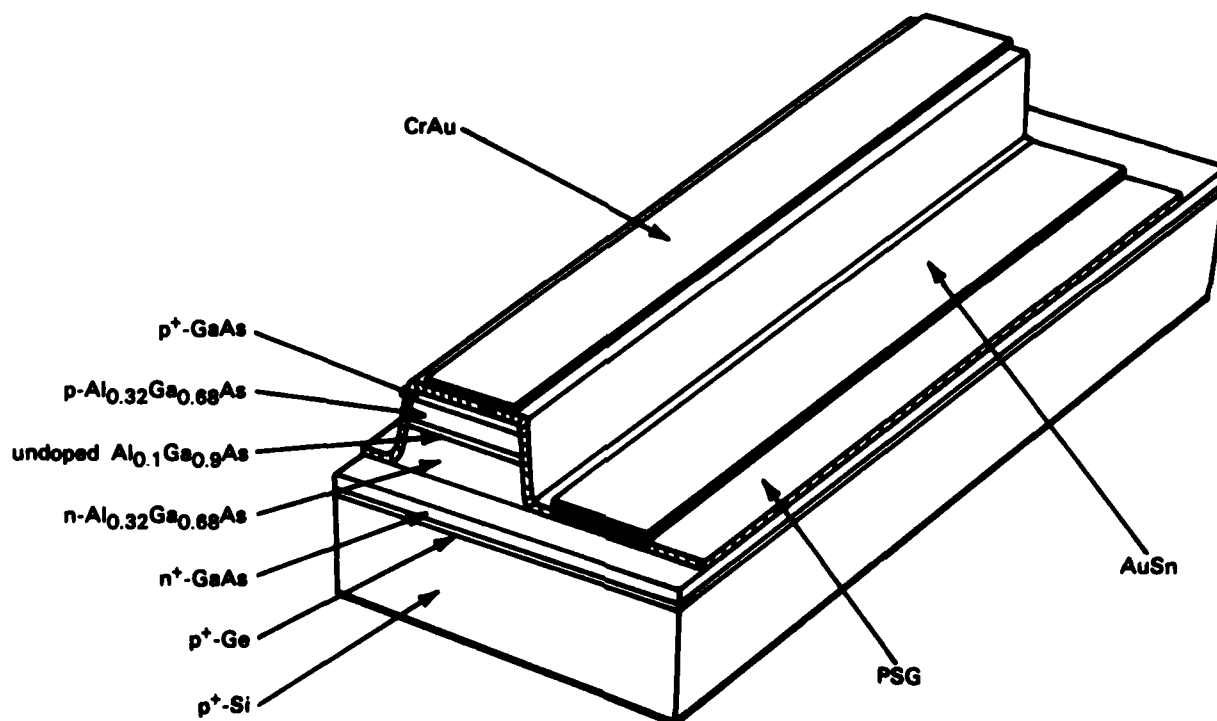
Figure 3-6. Schematic illustration of the MGS double-heterostructure diode laser showing one of the etched facets.

Device fabrication begins by etching through the AlGaAs layers to expose the GaAs buffer layer, forming a series of long parallel mesas 100 μm wide separated by contact wells. The wafer is then coated with pyrolytically deposited phosphosilicate glass (PSG). Contact windows are opened through the PSG in the wells, and the exposed n^+ buffer layer

37
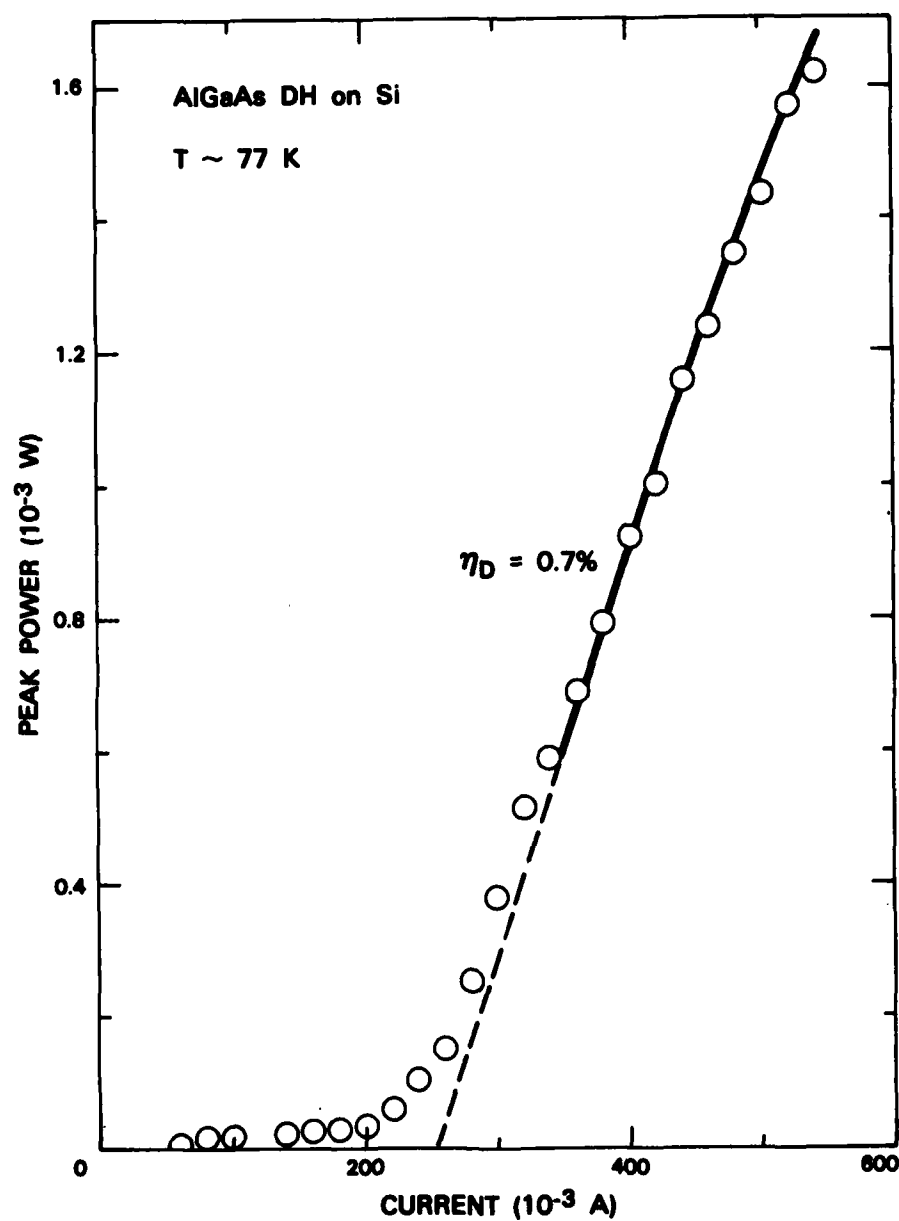
Figure 3-7. Power emitted from one facet of an MGS diode laser as a function of pulsed bias current at 77 K. The 0.7 percent quantum efficiency was calculated assuming equal power emission from both facets.

38

is electroplated with a AuSn eutectic. Off-center stripe contact windows (8 × 300 μm) are then opened in the PSG on the mesas. Chrome-gold contact pads are deposited over the stripe contact windows by electron-beam evaporation and photolithographic liftoff.

Because GaAs and Si have different preferred cleavage planes the MGS laser facets cannot be formed by cleaving through the entire structure, the technique used for conventional diode lasers. Instead, the facets are formed by ion-beam assisted etching.[18] A thin layer of Ni deposited by electron-beam evaporation is used as an etch mask. By means of photolithographic liftoff the Ni is removed from the regions separating adjacent rows of 300-μm-long devices. The exposed area is then etched to approximately the depth of the buffer layer, forming channels with vertical sidewalls. These sidewalls form the etalon facets. The Ni is removed by immersing the wafer in sulfuric acid. Finally, the wafer is diced into individual chips to facilitate device characterization.

Several devices randomly chosen from a single wafer were evaluated by pulsed operation at room temperature. The spontaneous emission was very weak, and all the devices failed during attempts to increase the bias sufficiently to obtain stimulated emission. Ten more devices from the same wafer were then evaluated at ~77 K by applying 100-ns pulses at a 1-kHz repetition rate. Eight of these produced stimulated emission at values of threshold current (I_{th}) between 260 and 350 mA. If current spreading under the stripe contact is neglected, the lowest threshold of 260 mA corresponds to a threshold current density of 10.8 kA/cm^2. For the device with this threshold the power output from one facet is plotted against current in Figure 3-7. The differential quantum efficiency is 0.7 percent, assuming equal power emission from both facets. The maximum power output for the various devices ranged from ~1.6 to 1.8 mW per facet, corresponding to efficiencies from 0.6 to 1.2 percent. It is probable that the low values of output power and efficiency result largely from the high defect density in the grown layers. The measured etch pit density was ~5 × 10^6 cm^{-2}. Improvements in material quality, device geometry, and fabrication techniques are expected to result in greatly improved performance.

Emission spectra obtained above and below I_{th} for the lowest threshold laser, operating at ~77 K, are shown in Figure 3-8. The emission at 1.1 I_{th} is nearly single mode with maximum intensity at 7812 Å (1.587 eV). A device with a threshold of 290 mA also exhibited a nearly single mode emission spectrum, peaked at 7787 Å (1.592 eV). The remaining devices had multimode emission spectra, with a dominant peak about 6 dB larger in intensity than the next highest one. In all cases the dominant peak, which ranged in wavelength from 7787 to 7812 Å, occurred on the long wavelength side of the spontaneous emission curve. The separation between the minor peaks was ~3 Å, which is characteristic of multiple longitudinal mode oscillation.

T.H. Windhorn   B-Y. Tsaur
G.M. Metze   J.C.C. Fan

Figure 3-9. Spectral emission from the lowest threshold MGS diode laser at 77 K, exhibiting (a) nearly single mode oscillation at 1.1 I_{th}, and (b) spontaneous emission at 0.9 I_{th}.

40

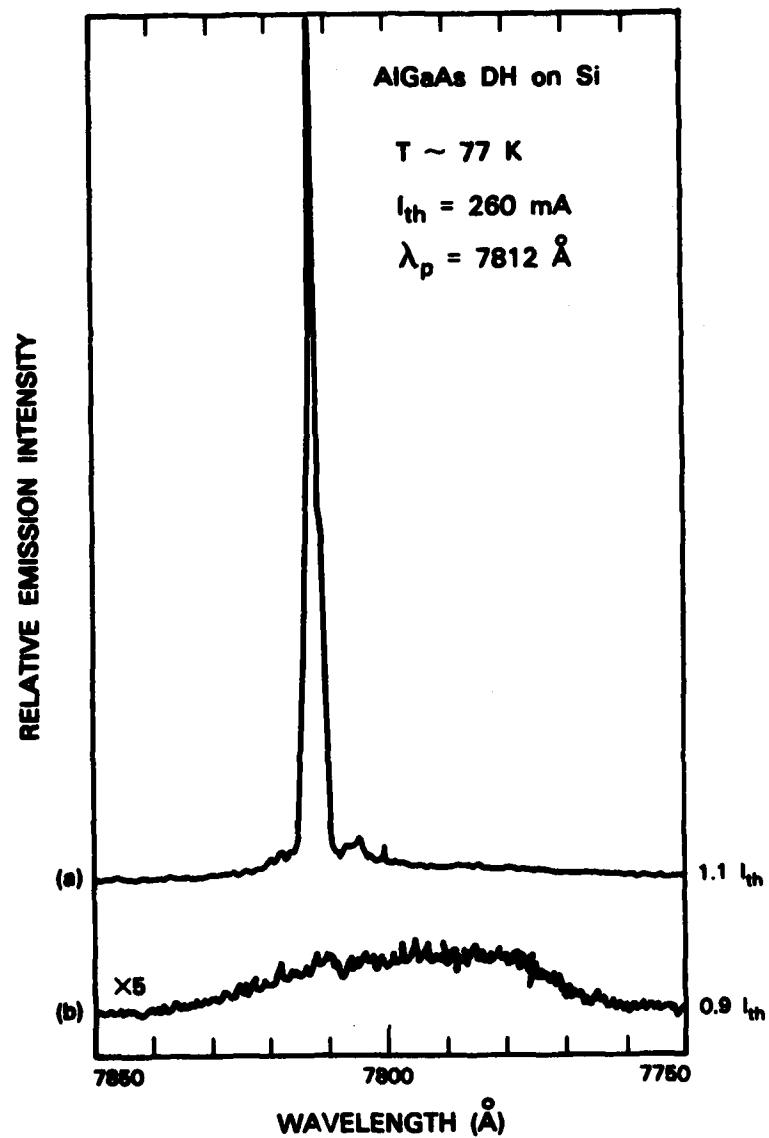## 3.3 GaAsP SHALLOW-HOMOJUNCTION SOLAR CELLS FOR TANDEM APPLICATIONS

The large increase in conversion efficiency calculated for two-cell, multi-bandgap tandem structures over single-junction cells could make tandem structures the economically preferable choice for large-scale photovoltaic systems.[19] For AM1 one-sun conditions, the maximum efficiencies calculated for two-cell structures are 36 to 37 percent, compared to 27 to 28 percent for single-junction cells. For optimum overall performance of a two-cell tandem structure, the upper cell should have a bandgap of 1.7 to 1.8 eV, and the bandgap of the bottom cell should be 1.0 to 1.1 eV (Reference 19). The advanced state of Si solar cell technology suggests Si, with a bandgap of 1.1 eV, as the most probable choice for the bottom cell material. Among the most promising materials for the top cell are $Ga_{1-x}Al_xAs$ and $GaAs_{1-x}P_x$ alloys with x values between 0.25 and 0.35. The technology involved in utilizing these ternary alloys for solar cells is still in the early stage of development.

We have chosen to investigate GaAsP for the upper cell material. Shallow-homojunction $GaAs_{0.82}P_{0.18}$ cells have previously been fabricated on GaAs substrates by low-pressure organo-metallic chemical vapor deposition (OMCVD).[20] The $GaAs_{0.82}P_{0.18}$ active region was grown directly on the GaAs substrate without any intermediate layers of graded alloy composition. The efficiency at 7.4 suns was 14.8 percent at AM2, but no one-sun results were given. We report here the fabrication on single-crystal GaAs substrates of $GaAs_{0.75}P_{0.25}$ shallow-homojunction solar cells with one-sun conversion efficiencies of 14.8 pecent at AM1. This GaAsP technology will be applicable to the fabrication of mechanically stacked tandem cells using the CLEFT process[21,22] and monolithic tandem cells formed by direct growth on Ge-coated Si substrates.[15]

The shallow-homojunction $n^+/p/p^+$ structures were deposited on GaAs substrates oriented 2° off (100), using an $AsCl_3$-PCl_3-H_2-GaAs CVD system.[23,24] To minimize the effects of the 1-percent lattice mismatch between $GaAs_{0.75}P_{0.25}$ and GaAs, a two-step graded composition structure was grown first. This structure consists of successive p^+ $GaAs_{0.93}P_{0.07}$ and p^+ $GaAs_{0.88}P_{0.12}$ layers, each ~3 μm thick and doped with Zn to ~5 × 10^{18} cm^{-3}. Three $GaAs_{0.75}P_{0.25}$ layers were then deposited: 4-μm-thick p^+ (Zn-doped, ~5 × 10^{18} cm^{-3}), ~4-μm-thick p (Zn-doped, ~1 × 10^{17} cm^{-3}) and ~1500-Å-thick n^+ (S-doped, ~4 × 10^{18} cm^{-3}). No window layer was used.

Figure 3-9 is an optical micrograph showing the stained cross section of a step-graded solar cell structure. The compositions of the GaAsP layers were determined from their lattice constants, as measured by x-ray diffraction. The step-graded cells have mirror-like surfaces that exhibit a cross-hatched morphology, as shown in Figure 3-10. For $GaAs_{0.75}P_{0.25}$ grown without step-graded intermediate layers, the surface is very rough and irregular.

Cell fabrication techniques were similar to those used for single-crystal GaAs cells.[24] The front and back contacts were electroplated gold. Cell areas of 0.095 or 0.51 cm^2 were

3.3 μm
3.7 μm
2.5 μm
2.5 μm

$\}$ $x = 0.25$ p^+, p, n^+
$\leftarrow$ $x = 0.12$ p^+
$\leftarrow$ $x = 0.07$ p^+

GaAs SUBSTRATE

Figure 3-9.   Stained cross section of GaAs$_{1-x}$P$_x$ step-graded solar cell structure.

200 μm

NO GRADED
STRUCTURE

WITH 2-STEP GRADED
STRUCTURE
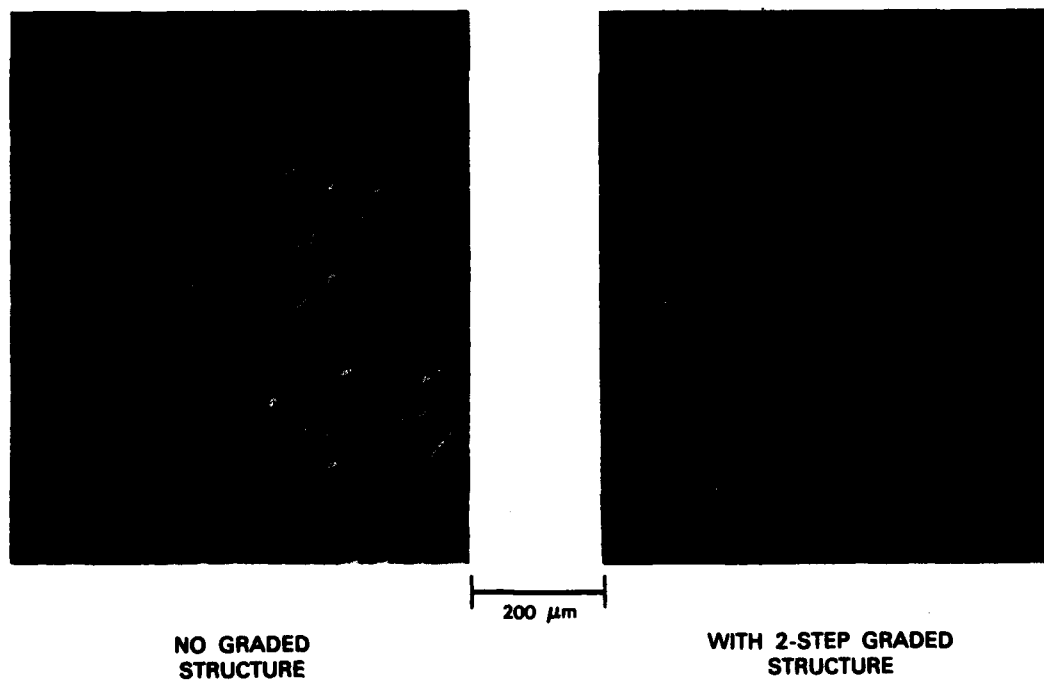
Figure 3-10.   Surface morphology of GaAs$_{0.75}$P$_{0.25}$ layers without step grading (left) and with two-step compositional grading (right).

defined by etching. The n^+ layer was thinned to <1000 Å by an anodic oxidation step. An antireflective coating was used but was not optimum for a bandgap of 1.7 eV. The final cell configuration is shown in Figure 3-11.

For a $GaAs_{0.75}P_{0.25}$ cell with an area of 0.51 cm^2, rooftop measurements of the short-circuit current density J_{sc} and open-circuit voltage V_{oc} were made at noon under approximately AM1 conditions at an ambient temperature of 13°C. The rooftop power density determined with a Si standard reference cell was 100 mW/cm^2. An I-V curve was then measured in the laboratory with the cell maintained at 13°C under illumination from a xenon-lamp AM1 solar simulator adjusted to give the same J_{sc} (15.6 mA/cm^2) as the rooftop measurement. The value of the V_{oc} was found to be 1.21 V.

Measurements with the calibrated solar simulator were then made on the same cell at 25°C. The I-V curve at 100 mW/cm^2 is shown in Figure 3-12. The J_{sc} is 15.2 mA/cm^2, V_{oc} is 1.18 V and the fill factor is 0.80, yielding a one-sun efficiency of $\sim$14.8 percent at AM1. For $GaAs_{0.75}P_{0.25}$ cells grown without composition grading between the active layers and the GaAs substrate, we have never measured values of V_{oc} exceeding 0.95 V at one sun, presumably because the quality of these layers is degraded by misfit dislocations resulting from the GaAsP/GaAs lattice mismatch.

Figure 3-13 shows the curve of external quantum efficiency vs wavelength measured at room temperature for a $GaAs_{0.75}P_{0.25}$ cell. The edge of the curve fixes the cell bandgap at $\sim$1.7 eV, consistent with the active layer composition of $GaAs_{0.75}P_{0.25}$ determined by x-ray diffraction. The cell shows very good response at wavelengths close to the edge, indicating good minority carrier diffusion length. The efficiency at shorter wavelengths could be improved by optimizing the n^+ layer thickness and using a more effective antireflection coating. These improvements can be expected with further development of GaAsP cell fabrication technology.

For mechanically stacked two-cell tandem structures, thin single-crystal GaAsP cells are needed. It should be possible to obtain such cells by the CLEFT process, in which a layer formed by lateral growth over a patterned mask is cleaved from the substrate. This process was initially demonstrated for GaAs layers[21] and solar cells[22] grown on (110) GaAs substrates. In preliminary experiments using such substrates we have obtained smooth $GaAs_{0.75}P_{0.25}$ layers by lateral overgrowth, and we have successfully separated one of these layers from the substrate.

R.W. McClelland J.C.C. Fan

B.D. King R.L. Chapman
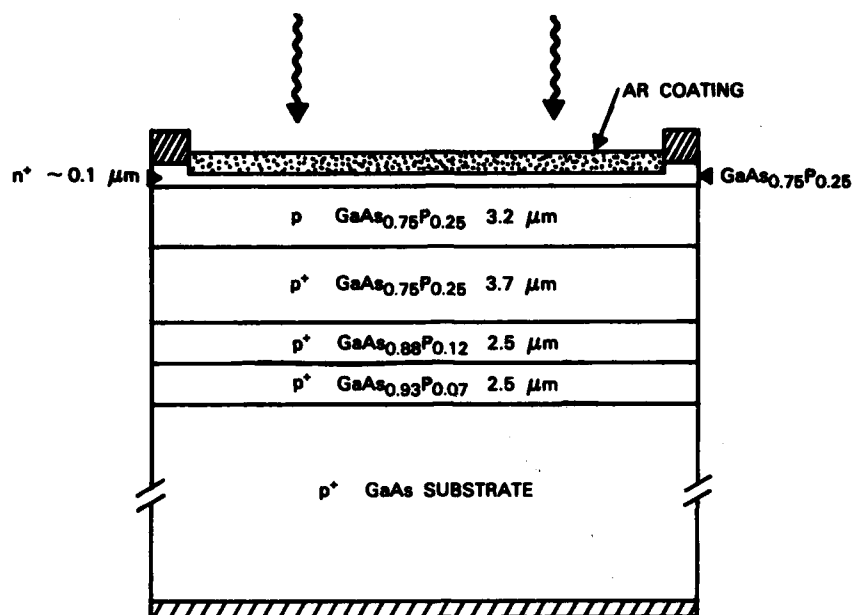
Figure 3-11. Schematic cross section of step-graded GaAs$_{0.75}$P$_{0.25}$ shallow-homojunction solar cell.
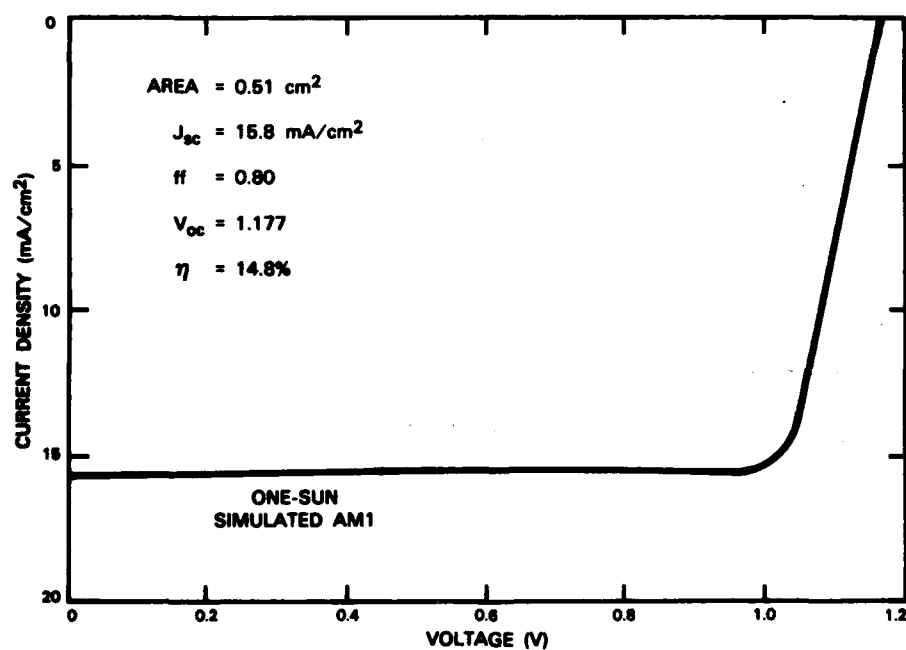
Figure 3-12. Current density as a function of voltage for GaAs$_{0.75}$P$_{0.25}$ solar cell under simulated AM1, one-sun conditions.

44
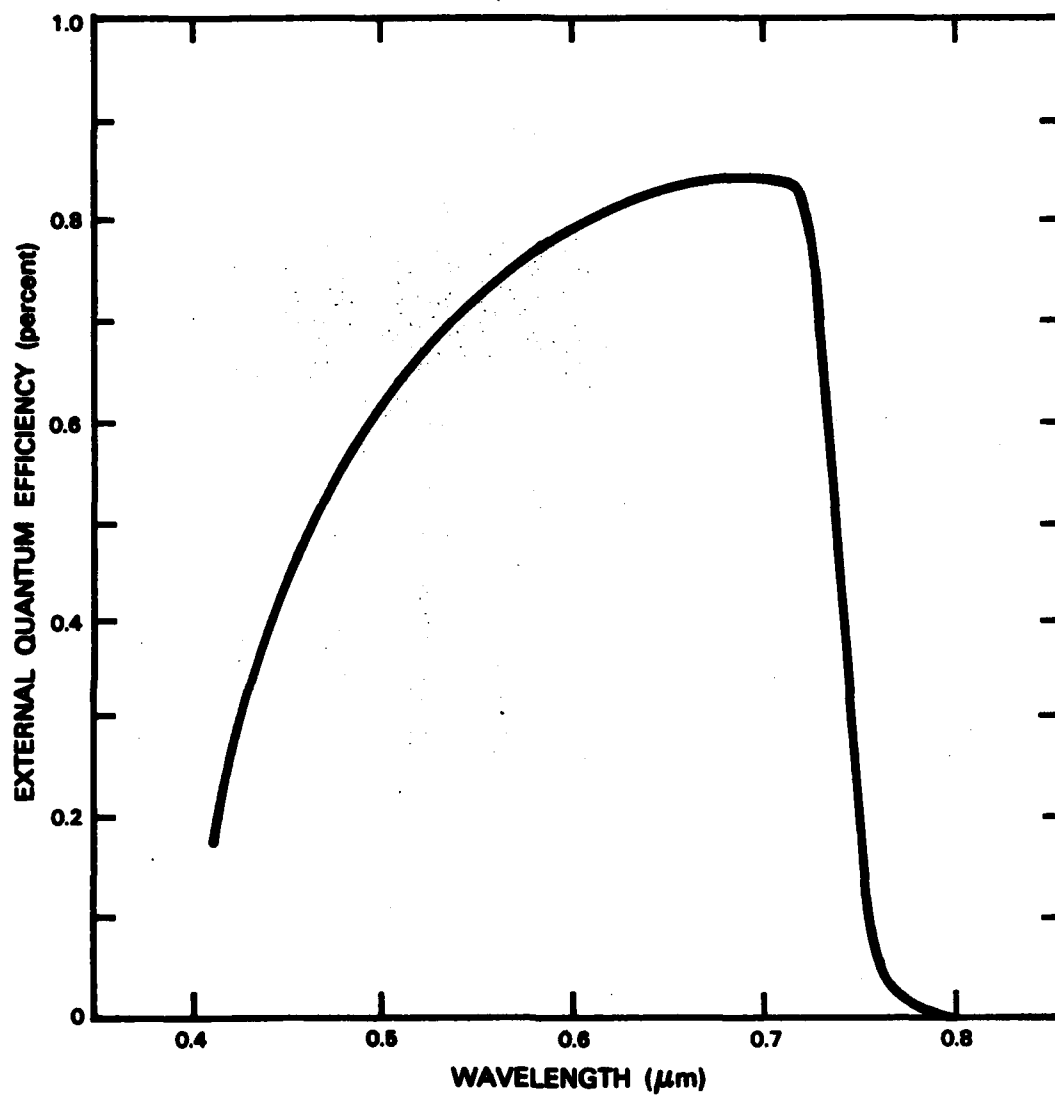
Figure 3-13. External quantum efficiency as a function of wavelength for a GaAs$_{0.75}$P$_{0.25}$ cell.

REFERENCES

1. B-Y. Tsaur, J.C.C. Fan, M.W. Geis, D.J. Silversmith, and R.W. Mountain, Appl. Phys. Lett. **39**, 561 (1981).

2. M.W. Geis, H.I. Smith, B-Y. Tsaur, J.C.C. Fan, E.W. Maby, and D.A. Antoniadis, Appl. Phys. Lett. **40**, 158 (1982).

3. J.C.C. Fan, B-Y. Tsaur, and M.W. Geis, J. Cryst. Growth **63**, 453 (1983).

4. Solid State Research Report, Lincoln Laboratory, M.I.T. (1983:1), p. 43, DTIC AD-A128894/3.

5. See, for example, D.J. DiMaria, A.A. Weinberg, and J.M. Aitken, J. Appl. Phys. **48**, 898 (1977).

6. B-Y. Tsaur, J.C.C. Fan, G.W. Turner, and D.J. Silversmith, IEEE Electron Device Lett. **EDL-3**, 195 (1982).

7. P.S. Winokur, H.E. Boesch, Jr., J.M. McGarrity, and F.B. McLean, J. Appl. Phys. **50**, 3492 (1979).

8. F.B. McLean, IEEE Trans. Nucl. Sci. **NS-27**, 1651 (1980).

9. S.K. Lai, Appl. Phys. Lett. **39**, 58 (1981).

10. J. Miyamoto, S. Sitoh, H. Momose, H. Shibata, K. Kanzaki, and S. Kohyama, IEDM Tech. Digest, p. 63 (1983).

11. M. Rodder and D.A. Antoniadis, IEEE Electron Device Lett. **EDL-4**, 193 (1983).

12. B-Y. Tsaur, D.J. Silversmith, J.C.C. Fan, and R.W. Mountain, IEEE Electron Device Lett. **EDL-4**, 269 (1983).

13. E.W. Greeneich and R.H. Reuss, IEEE Electron Device Lett. **EDL-5**, 91 (1984).

14. J. Graul, A. Glasl, and H. Murrmann, IEEE J. Solid-State Circuits **SC-11**, 491 (1976).

15. R.P. Gale, J.C.C. Fan, B-Y. Tsaur, G.W. Turner, and F.M. Davis, IEEE Electron Device Lett. **EDL-2**, 169 (1981).

16. Y. Shinoda, T. Nishioka, and Y. Ohmachi, Jpn. J. Appl. Phys. **22**, L450 (1983).

17. Solid State Research Report, M.I.T. Lincoln Laboratory (1984:1); and H.K. Choi, B-Y. Tsaur, G.M. Metze, G.W. Turner, and J.C.C. Fan, IEEE Electron Device Lett. (to be published).

18. G.A. Lincoln, M.W. Geis, S. Pang, and N.N. Efremow, J. Vac. Sci. Technol. B **1**, 1043 (1983).

19. J.C.C. Fan, B-Y. Tsaur, and B.J. Palm, in *Proceedings of the 16th IEEE Photovoltaic Specialists Conference* (IEEE, New York, 1982), p. 692.

20. L.M. Fraas, B.K. Shin, J.A. Cape, R.A. Ransom, and D.E. Sawyer, *Ibid.*, p. 655.

21. R.W. McClelland, C.O. Bozler, and J.C.C. Fan, Appl. Phys. Lett. **37**, 560 (1980).

22. C.O. Bozler, R.W. McClelland, and J.C.C. Fan, IEEE Electron Device Lett. **EDL-2**, 203 (1981).

23. W.F. Finch and E.W. Mehal, J. Electrochem. Soc. **111**, 814 (1969).

24. C.O. Bozler, J.C.C. Fan, and R.W. McClelland, Chapter 5 in *Gallium Arsenide and Related Compounds (St. Louis), 1978* (The Institute of Physics, London, 1979), pp. 429-436, DDC AD-A072370/0.

4. MICROELECTRONICS

4.1 A SELF-ALIGNED DUAL-GRATING GaAs PERMEABLE-BASE TRANSISTOR (PBT)

Discrete GaAs PBTs have been fabricated with measured gain of 16 dB at 18 GHz and an extrapolated maximum frequency of oscillation of $\sim$100 GHz.[1] To maintain the high-frequency performance of these devices in circuits, the techniques by which they are integrated become important. We describe a new PBT structure, permitting either vertical or planar integration, in which two independently contacted submicrometer-period tungsten gratings are embedded one above the other in single-crystal GaAs. In this structure the lines and spaces of the upper grating are aligned with the spaces and lines, respectively, of the lower grating.

The dual-grating PBT fabrication sequence is summarized in Figure 4-1. Two scanning electron microscope (SEM) micrographs of typical cleaved cross sections of completed devices are shown in Figure 4-2. The light regions are the tungsten grating lines and the gray background is the GaAs. The high magnification micrograph of Figure 4-2(a) reveals a dual-grating structure of quality similar to previous single-grating PBTs.[2,3] The lower magnification micrograph of Figure 4-2(b) shows an extremely uniform pair of buried gratings with no missing tungsten lines. High-quality overgrowths similar to those shown in Figure 4-2 have been obtained on several wafers.

The key features of the dual-grating structures, together with two potential integration schemes, are shown schematically in Figure 4-3. If this structure is fabricated on an n^+ substrate, as in this study, the vertical integration shown in Figure 4-3(b) is obtained, with both gratings playing the role of control electrodes. Since the spacing between the gratings can be varied by varying the etch depth into the n-GaAs, these devices offer the opportunity to study dual-base transistors over the entire range from interacting to independent operation.[4] The structure in Figure 4-3(b) can be used as a PBT NAND gate if a load resistor or transistor is connected to the collector terminal. If the dual-grating structure is fabricated on a semi-insulating substrate, the planar single-base PBT of Figure 4-3(c) is obtained, with the lower grating used as the collector contact electrode, so that all three contacts are accessible from the top surface.

Figures 4-4(a) and (b) show current-voltage characteristics for a device with a spacing between the upper and lower grating of 0.35 μm that uses the vertical integration scheme of Figure 4-3(b). The upper grating-to-emitter voltage, V_2, is +0.5 V in Figure 4-4(a) and –1.0 V in Figure 4-4(b), while in both cases the lower grating-to-emitter voltage is varied from –1.5 V to +0.5 V in 0.5-V increments. These current-voltage characteristics demonstrate the feasibility of obtaining four-terminal device operation from a dual-grating GaAs PBT. While considerable additional work is necessary to improve device characteristics, a structure of this type offers the potential for PBT integration as well as the potential for studying the device physics of closely spaced short-gate transistors.

B.A. Vojak   A.R. Calawa
R.W. McClelland   D.C. Flanders
G.A. Lincoln   M.W. Geis

Ni

SiO₂

GaAs

DEFINE SUBMICROMETER-PERIOD
GRATING Ni ETCH MASK BY
X-RAY LITHOGRAPHY AND LIFTOFF

REACTIVE-ION ETCH SiO₂
AND INTO GaAs

ION-BEAM-ASSISTED ETCH GaAs

REMOVE ETCH MASK
BY WET ETCHING

W

EVAPORATE W

GROW GaAs BY VAPOR
PHASE EPITAXY

124335-N-03
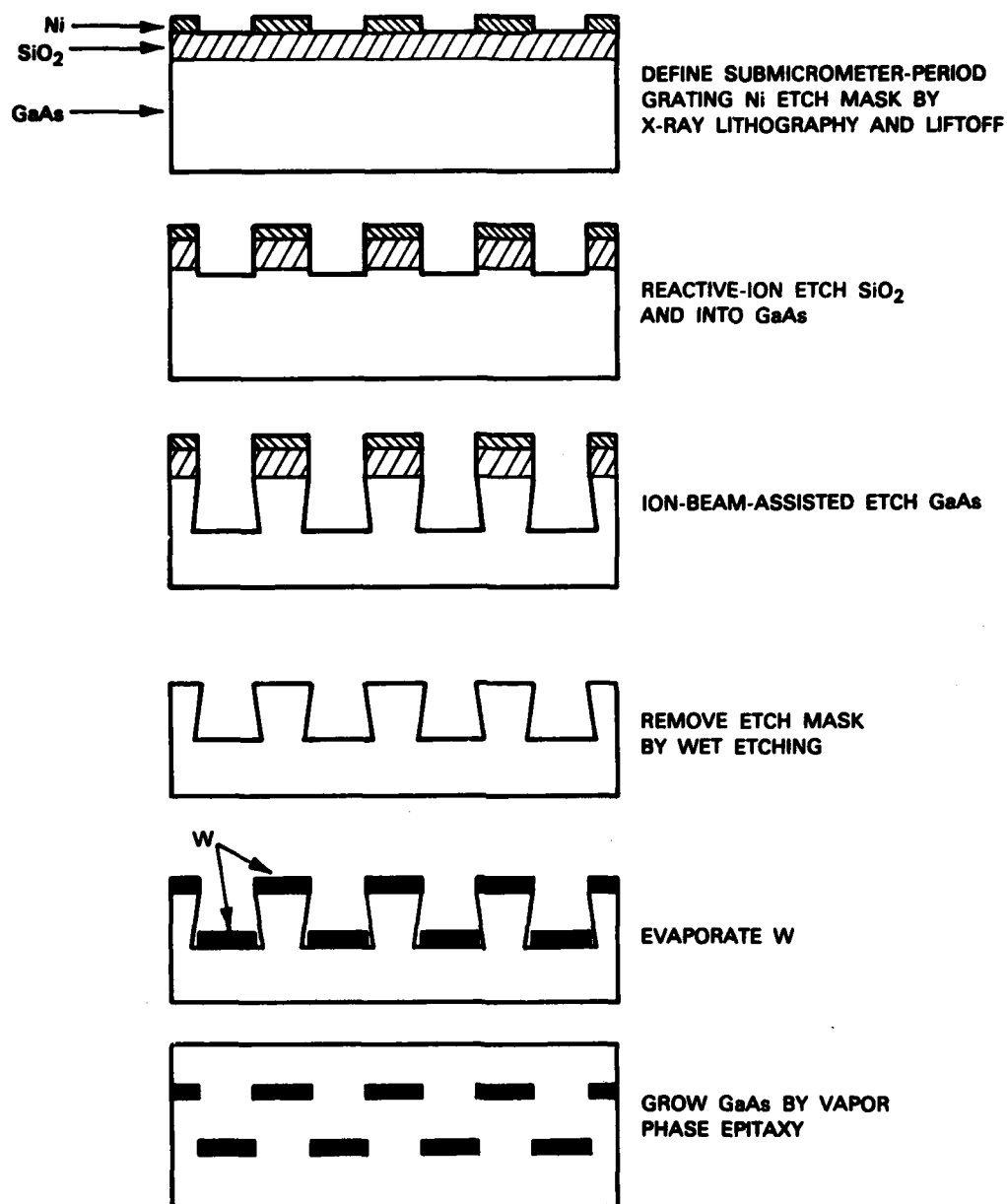
Figure 4-1. Self-aligned dual-grating GaAs permeable-base transistor fabrication sequence.

50

(a)
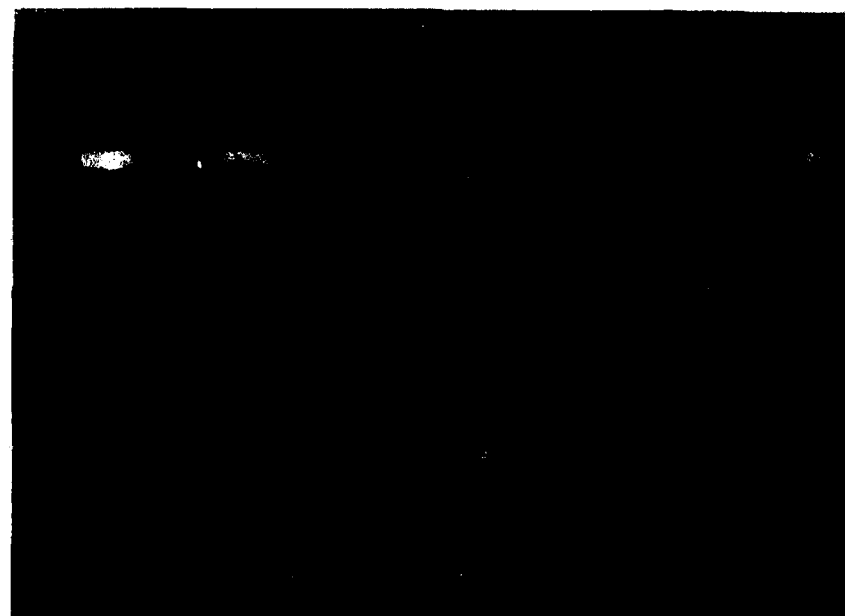
(b)

Figure 4-2. SEM cleaved cross-section micrographs of a dual-grating PBT: (a) high magnification and (b) low magnification.

51
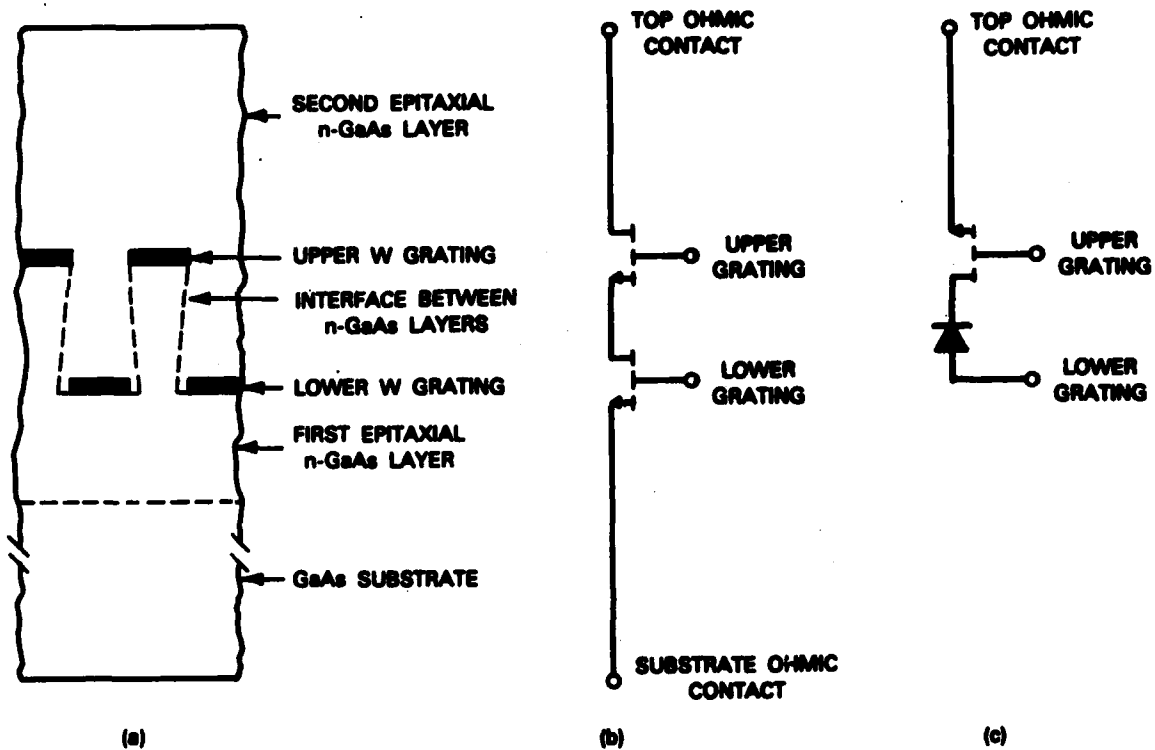
Figure 4-3. (a) The generic dual-grating PBT structure; (b) and (c) two potential integration schemes.

(a) $V_2 = 0.5$ V

(b) $V_2 = -1.0$ V

Figure 4-4. Common-emitter current-voltage characteristics of a dual-grating PBT operating in the vertical integration scheme of Figure 4-3(b).

4.2 GENERATION OF <50-nm PERIOD GRATINGS USING EDGE-DEFINED TECHNIQUES

Recently, high resolution edge-defined techniques have been developed which enable one to generate smaller linewidths than are possible using conventional lithography. Several of these techniques result in a doubling of the number of lines in a pattern since both edges of the original pattern lead to the generation of a new line. This property of edge-defined techniques has been used to generate smaller period gratings[5-7] than are readily obtained by conventional interferometric techniques. We report several new sequences of edge-defined techniques which allow the multiplication of the number of lines in a grating pattern. Two sequences that can be used successively are shown in Figures 4-5 and -6. In the first sequence an initial or "parent" grating pattern with vertical sidewalls and controlled linewidth is fabricated in SiO_2 on a silicon wafer. A layer of Si_3N_4 of controlled thickness is deposited on the parent structure by chemical vapor deposition (CVD). The areas of the Si_3N_4 layer which are parallel to the plane of the wafer are then removed in an isotropic
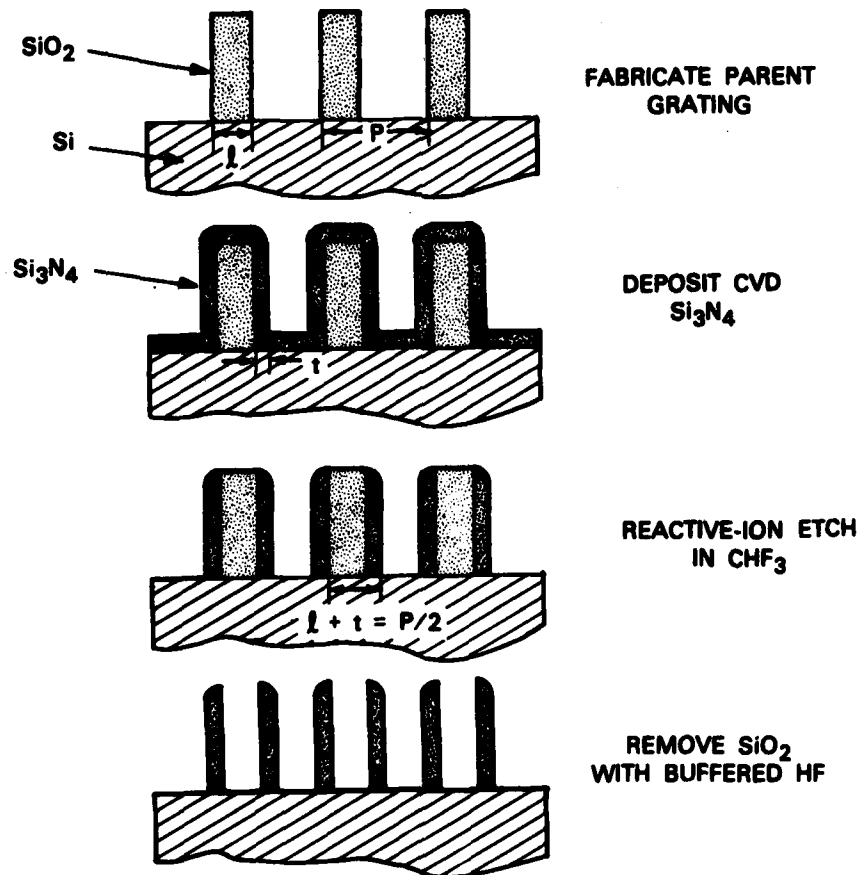
Figure 4-5. Sequence of fabrication steps for doubling the number of lines in a grating pattern. The initial grating is composed of SiO_2 and the final grating is composed of Si_3N_4.

54

selective etch. Figure 4-5 shows that if the linewidth of the parent grating plus the thickness of the CVD deposited Si_3N_4 is equal to one-half of the period grating, the final structure will be a grating with one-half the parent grating period having a linewidth equal to the CVD Si_3N_4 thickness. A similar sequence is shown in Figure 4-6. In this case either Si_3N_4 or SiO_2 can be used for the parent grating since CVD Si is used in place of the CVD Si_3N_4 used in Figure 4-5. This allows selective removal of the Si_3N_4 in concentrated HF, which does not etch the Si. Successive use of the processes shown in Figures 4-5 and -6 can result in gratings of one-quarter of the period of the parent grating if proper linewidth and thickness control is realized. The quality of the parent grating is clearly of paramount importance. The precision with which the linewidths can be controlled and the smoothness of the line edges ultimately determine how many times the lines in a grating can be doubled and still yield a useful structure.

Si_3N_4
OR   →   FABRICATE PARENT
SiO_2 GRATING

Si →

Si →

                         DEPOSIT LPCVD
                              Si

                         REACTIVE-ION ETCH
                              IN CF_4

                         REMOVE Si_3N_4 OR SiO_2
                              WITH HF
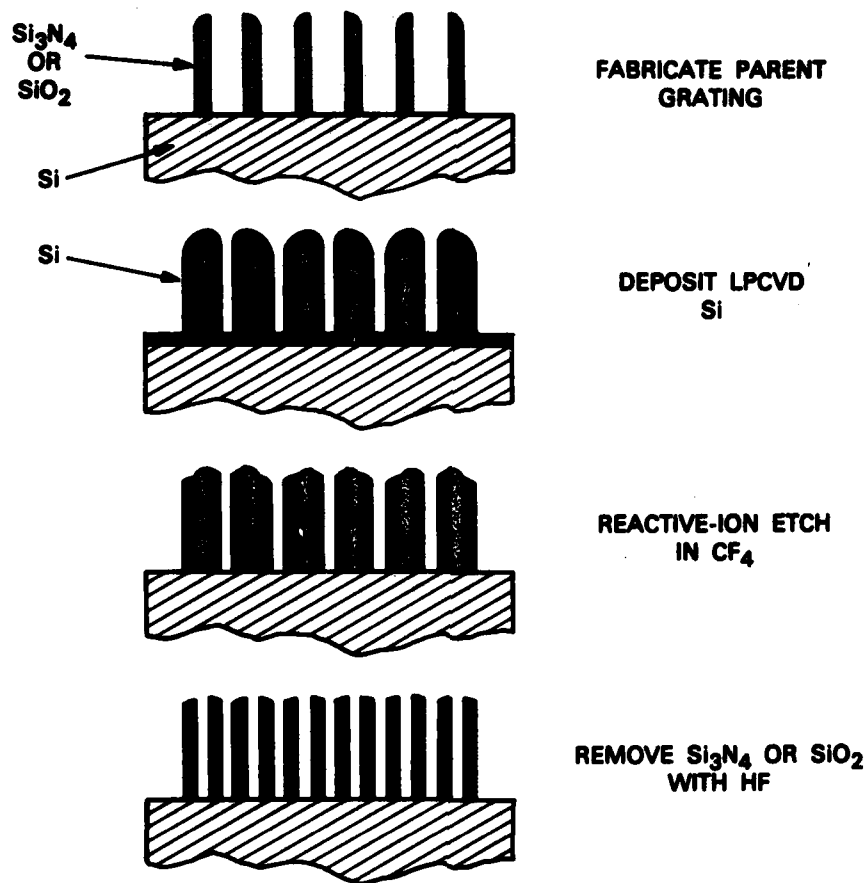
Figure 4-6. Sequence of fabrication steps which results in the doubling of the number of lines in a Si_3N_4 or SiO_2 grating. The final structure is composed of Si.

55
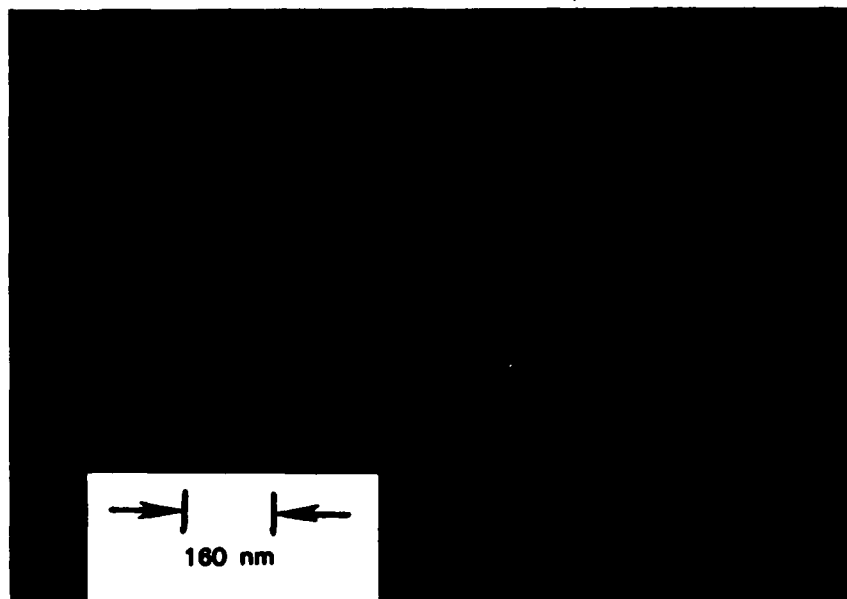
Figure 4-7. SEM micrograph of a 160-nm-period PMMA grating on a SiO₂-coated silicon substrate. The grating was exposed using a "shadowed" x-ray mask with carbon (4.5 nm) x-ray line.

X-ray masks with 240- and 160-nm period were prepared by holographic exposure. Details of the anisotropic etching of silicon, replication of the structure in polyimide, and shadowing of the polyimide structure with tungsten required to complete the masks are described in previous publications.[8,9] An SEM micrograph of a 160-nm-period PMMA grating on an SiO₂-coated silicon substrate produced by replicating one of these masks with contact carbon (4.5 nm) x-ray lithography is shown in Figure 4-7. The area of this mask is ~ 1 cm². The fabrication sequences illustrated in Figures 4-5 and -6 were executed using parent gratings made from the 240- and 160-nm masks. Figures 4-8 and -9 show the parent SiO₂ grating, Si₃N₄ grating with one-half the initial period, and Si grating with one-quarter the initial period for the 240- and 160-nm-period gratings. The one-half period gratings are quite good, with minimum fundamental components. The one-quarter period gratings are not as good because of cumulative errors in line thickness. This is mainly due to the difficulty of making accurate linewidth measurements in the SEM, which are required because the deposition thicknesses are not the same on the gratings and flat areas. Careful iterative adjustments in the process should yield nearly perfect gratings.
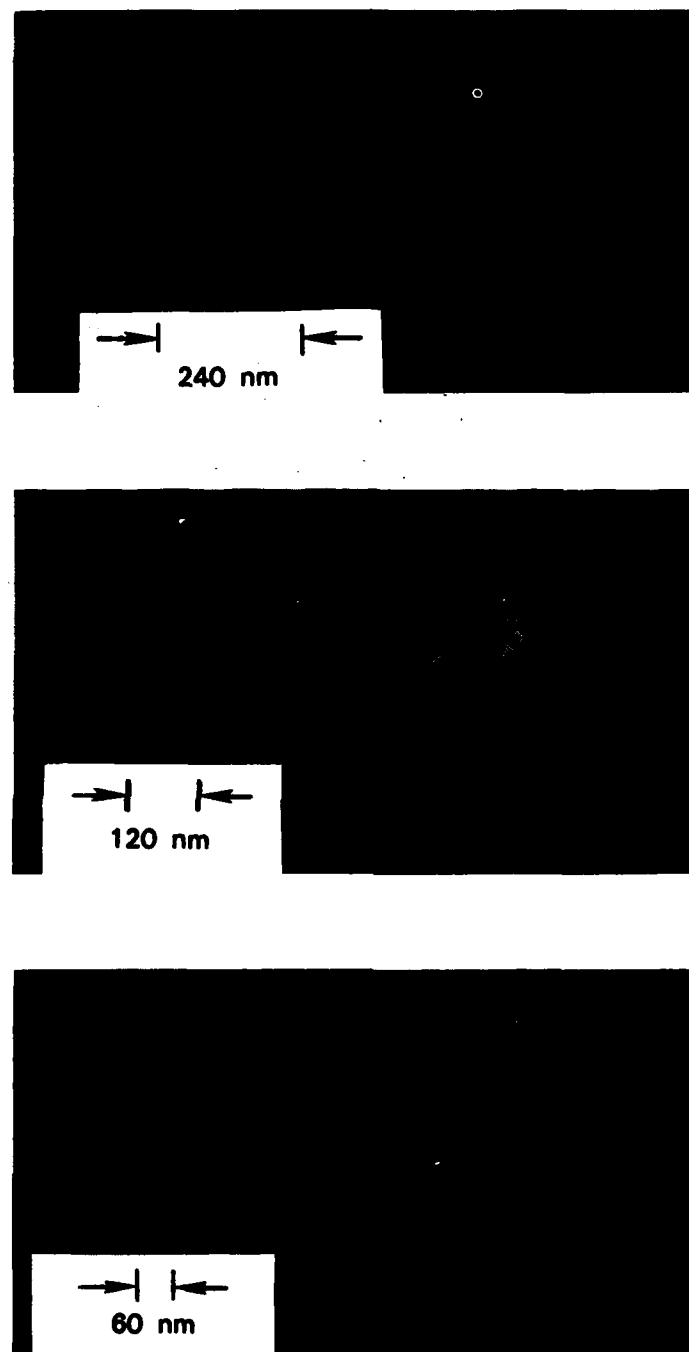
Figure 4-8. SEM micrographs of a 240-nm SiO_2 grating, a 120-nm-period Si_3N_4 grating produced from the SiO_2 grating, and a 60-nm-period Si grating produced from the 120-nm-period Si_3N_4 grating.

57
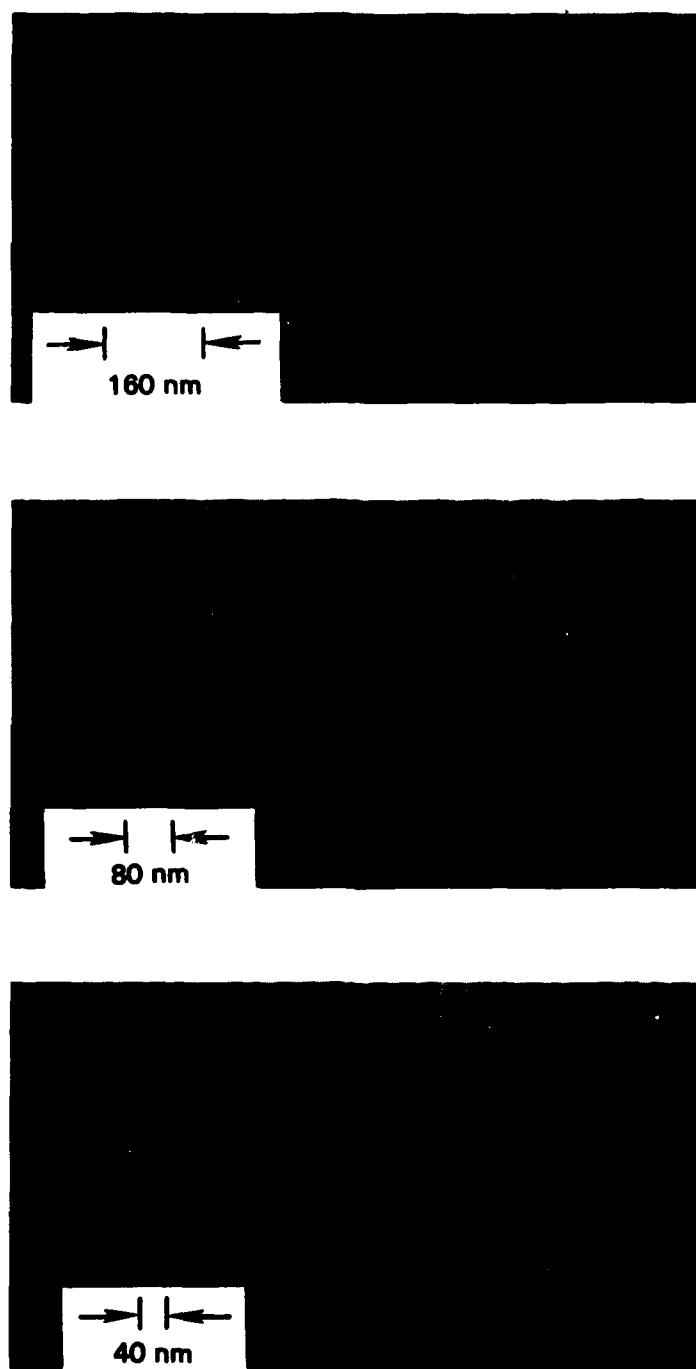
Figure 4-9. SEM micrographs of a 160-nm-period SiO$_2$ grating produced from the 160-nm-period SiO$_2$ grating, and a 40-nm-period Si grating produced from the 80-nm-period Si$_3$N$_4$ grating.

58

Because of their very small periods and the large areas possible (≈ 1 cm^2 in this work), these gratings will be useful in a wide variety of new applications and devices. X-ray replication of gratings smaller than 40-nm period appears to be quite difficult. However, it is clear that processes similar to those illustrated in Figures 4-5 and -6 could be used directly to produce useful gratings perhaps as small as 10-nm period from a 40-nm parent grating on a variety of substrates.

D.C. Flanders
N.N. Efremow

4.3 IMPURITY SCATTERING IN QUANTUM WELLS

We have observed direct evidence that the presence of impurities in a quantum well will lower the resonant tunneling current density. By eliminating impurities from the well, we have been able to increase the tunneling current density by a factor of nearly 30 over previously reported measurements.[10,11]

The energy diagram for the double barrier tunneling structure is shown in Figure 4-10. The transmitted current density has peaks which correspond to a resonant condition between the two barriers, much as in an optical Fabry-Perot resonator. The one-electron wave function ψ is also shown in Figure 4-10 for an electron incident from the left. Resonance
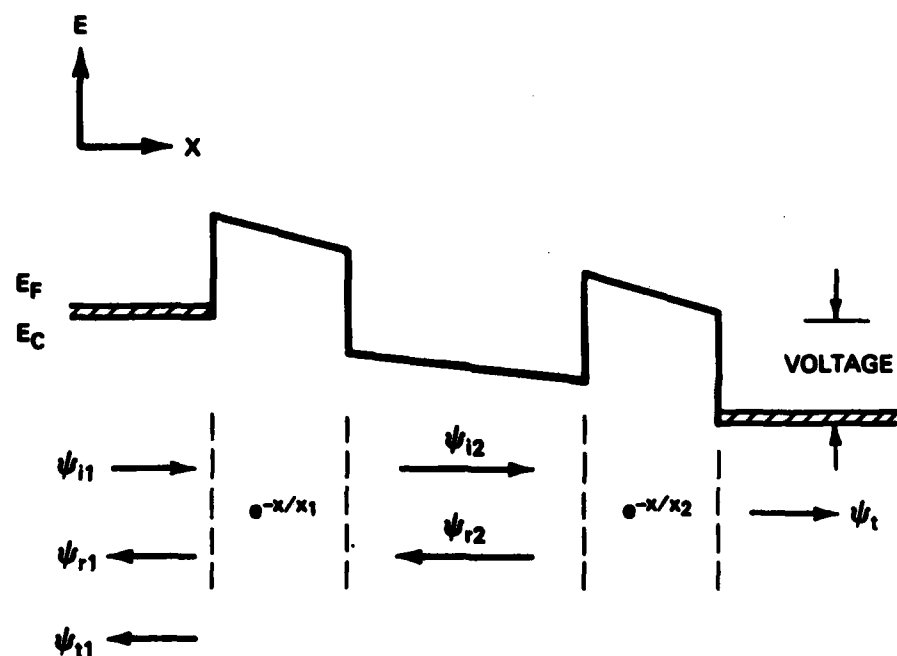
Figure 4-10. Electron energy as a function of distance for a double-barrier tunneling structure. Also shown are the various components of the single-electron wave function, ψ, for an electron incident from the left.
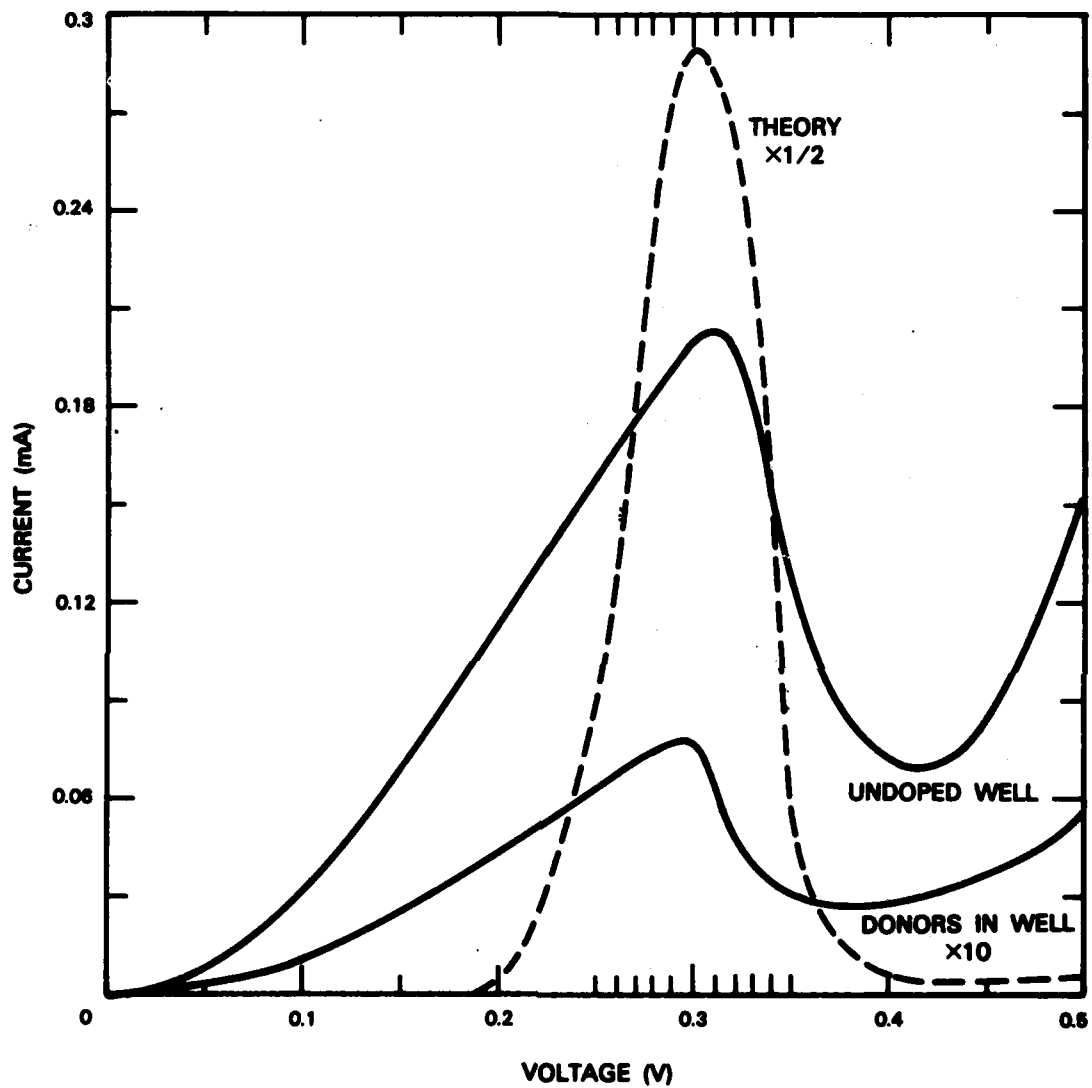
Figure 4-11. Current-voltage curves at 77 K for samples with intentionally doped well region, undoped well, and a theoretical I-V curve assuming no scattering. The current axis of the doped-well sample and of the theoretical curve have been scaled for clarity.

60

occurs when the reflected part of the wave function ψ_{r1} is cancelled by that part of ψ_{r2} which extends outside the well through the left barrier, ψ_{t1}. Any scattering of the electron in the well would destroy the coherence between ψ_{r1} and ψ_{t1}, reducing the transmission to the product of the individual transmission coefficients of the two barriers.

In our original experiments[11] the central 10 percent of the 40-Å well was doped with 10^{18} cm^{-3} Si donors, giving a sheet density of $N_s = 4 \times 10^{10}$ cm^{-2}. In the samples of the present study the wells were grown by MBE with no intentional doping. The result was a net acceptor concentration in the well of a few times 10^{14} cm^{-3}. All other parameters were the same during the growth of these two wafers.

Figure 4-11 shows the resulting I-V curves (at 77 K) of the two different types of wells for mesas with the same area (2×10^{-7} cm^2). The curve for the doped well has been multiplied by 10 for clarity. Also shown is the theoretical curve (divided by a factor of 2) which includes no scattering. The peak current for the undoped well is much closer to the theoretical current peak.

The theoretical I-V curve was calculated on the basis of the effective mass model. Continuity of ψ and ψ' is required at the barrier interfaces; also, momentum parallel to the barrier is conserved in the tunneling process. This is a first-order theory which does not include scattering, tunneling via impurities, or details of the semiconductor band structure. We have some evidence that the excess current measured at voltages below that corresponding to the peak is due to impurity-assisted tunneling, and we propose that the rapid increase in current at voltages above the peak is due to tunneling into upper conduction band valleys.

Calculation of the scattering cross section in the well is quite complex. The usual plane wave scattering is not valid since the incident particle has the wave function appropriate to tunneling through the well. Also the scattering couples the longitudinal and transverse momentum of the tunneling electron, which further complicates the solution of the tunneling current integral. Finally, the case here involves a rather high density of scattering centers, so multiple scattering may become important. Ignoring these difficulties may lead to comforting but erroneous results, so we shall pursue the solution of the more complete theory before making a numerical comparison with the experimental results presented here.

T.C.L.G. Sollner
H.Q. Le*
W.D. Goodhue

4.4 SOLID STATE SUBMILLIMETER-WAVE SOURCE

We are continuing to pursue the development of a compact, tunable source of radiation obtained by harmonic generation that can be used for spectroscopic experiments in the submillimeter. Previously, we had doubled the 285-GHz output of a carcinotron to 570 GHz in

---

* Frances Bitter National Magnet Laboratory, M.I.T.

PHASE-LOCKED
GUNN
OSCILLATOR

92.7 GHz →

INJECTION-
LOCKED
IMPATT
OSCILLATOR

FREQUENCY
TRIPLER

FREQUENCY
DOUBLER

556 GHz

142125-N
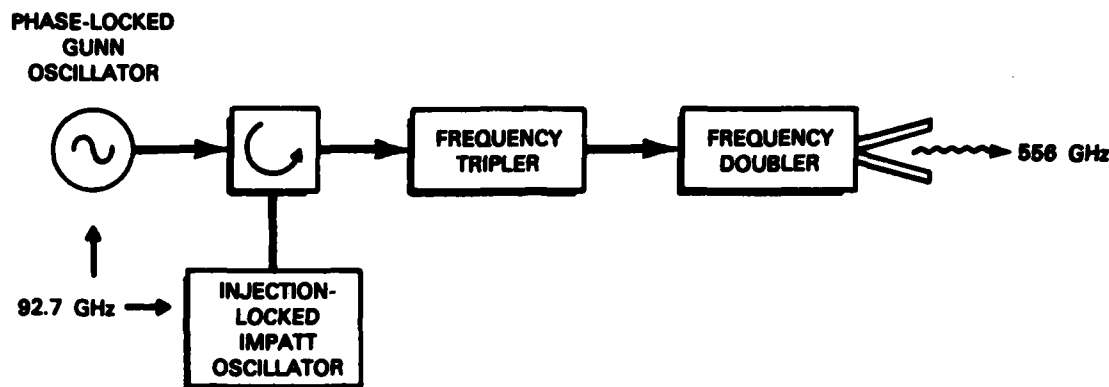
Figure 4-12. Block diagram of harmonic multiplication chain for 556-GHz solid state source.

a harmonic mixer.[12] We have now been able to generate radiation at 556 GHz (540 μm) by means of a frequency multiplier chain using only solid state components.

The first stage of this chain is a phase-locked GaAs Gunn oscillator at 92.7 GHz which drives an injection-locked Si IMPATT oscillator at the same frequency (see Figure 4-12). This fundamental source of 75 mW is applied to a frequency tripler containing a GaAs var-actor Schottky diode. The tripler produces 1 mW at 278 GHz, which is then fed by wave-guide to a frequency doubler containing a similar diode. The doubler yields approximately 50 μW at 556 GHz, for a total RF conversion efficiency of –32 dB. Frequency tunability is roughly 0.1 percent.

Although this system is suitable for use in direct-detection spectroscopy, it is not useful as the local oscillator of a low-noise heterodyne radiometer due to the IMPATT's character-istic, wideband noise. Consequently, we will attempt to substitute a Gunn oscillator of suffi-cient power for the fundamental driving source at 92.7 GHz.

J.A. Taylor
N.R. Erickson*
P.E. Tannenwald

* Five College Radio Astronomy Observatory, University of Massachusetts, Amherst.

REFERENCES

1. G.D. Alley, C.O. Bozler, N.P. Economou, D.C. Flanders, M.W. Geis, G.A. Lincoln, W.T. Lindley, R.W. McClelland, R.A. Murphy, K.B. Nichols, W.J. Piacentini, S. Rabe, J.P. Salerno, and B.A. Vojak, "Millimeter-Wavelength GaAs Permeable Base Transistors," 1982 Device Research Conference, Ft. Collins, Colorado, 21-23 June 1982.

2. B.A. Vojak and J.P. Salerno, Appl. Phys. Lett. **41**, 1151 (1982).

3. B.A. Vojak, J.P. Salerno, D.C. Flanders, G.D. Alley, C.O. Bozler, K.B. Nichols, R.W. McClelland, N.P. Economou, G.A. Lincoln, R.A. Murphy, W.T. Lindley, and G.D. Johnson, J. Appl. Phys. **54**, 3554 (1983).

4. E. Allamando, G. Salmer, M. Bouhess, and E. Constant, Electron. Lett. **18**, 791 (1982).

5. L.F. Johnson and K.A. Ingersoll, Appl. Phys. Lett. **38**, 532 (1981).

6. G.J. Sonek, D.K. Wagner, and J.M. Ballantyne, J. Vac. Sci. Technol. **19**, 921 (1981).

7. D.C. Flanders and Alice E. White, J. Vac. Sci. Technol. **19**, 892 (1981).

8. D.C. Flanders, Appl. Phys. Lett. **36**, 93 (1980).

9. D.C. Flanders, J. Vac. Sci. Technol. **16**, 1615 (1979).

10. R. Tsu and L. Esaki, Appl. Phys. Lett. **22**, 562 (1973).

11. T.C.L.G. Sollner, W.D. Goodhue, P.E. Tannenwald, C.D. Parker, and D.D. Peck, Appl. Phys. Lett. **43**, 588 (1983).

12. Solid State Research Report, Lincoln Laboratory, M.I.T. (1982:3), p. 27, DTIC AD-A124305/4.

5. ANALOG DEVICE TECHNOLOGY

5.1 SUPERCONDUCTIVE CONVOLVER WITH JUNCTION RING MIXERS

The first demonstration of a superconductive convolver has been described previously.[1,2] This device employed a niobium microstrip line as a low-loss delay element[3] and single, superconductive tunnel junctions as mixing elements. Because of the low saturation level of the single-junction mixers, the output level of this device was only marginally greater than the noise floor of the room-temperature electronics. An upgraded convolver has now been realized using multiple-junction ring mixers.

The new convolver design, shown schematically in Figure 5-1, incorporates superconductive ring mixers[4] with series arrays of tunnel junctions. The mixer ring provides higher output power levels and, with a quadrature feed, achieves a 10-dB suppression of undesirable mixing self-products over the 2-GHz design bandwidth. A photograph of the improved device, fabricated on a 125-μm-thin, 2.5×4 cm^2 sapphire substrate, is shown in Figure 5-2. The central region of the device consists of a meander delay line with proximity taps. A niobium ground plane is deposited on the opposite side of this substrate. A second sapphire substrate with another niobium ground plane is pressed against the delay-line region of the first substrate with a spring arrangement to create a 50-Ω 14-ns-long stripline. Taps with junction ring mixers which provide local multiplication are located along both sides of the meander delay line. The mixing products are collected and summed by two 15-Ω microstrip transmission lines; tapered lines transform the output to 50 Ω.

The device was evaluated by entering gated CW tones and wideband chirped waveforms (generated by superconductive tapped delay lines[5]) into the signal and reference ports of the device. The measured response for CW tones gated to 14-ns duration is shown in Figure 5-3(a). The output waveform approximates the triangular shape expected from the convolution of two nearly rectangular input pulses. A maximum device output level of -60 dBm and an efficiency factor 10 log $[P_{out}/(P_{sig} \times P_{ref})]$ of -32 dBm were measured. Compared to the earlier result,[2] this is a 16-dB increase in output relative to the thermal noise floor and a 9-dBm increase in efficiency. The improved performance allowed testing with wide bandwidth waveforms. The compressed pulse output of the convolver with inputs of a flat-weighted upchirp and a complementary downchirp is shown in Figure 5-3(b). The chirp slope is about 62 MHz/ns; the output waveform has an instantaneous bandwidth of 1.7 GHz. Use of flat-weighted chirps should yield a (sin x)/x response with a null-to-null width of 1.2 ns and peak relative sidelobes of -13 dB. A null-to-null width of 1.5 ns was observed with an excessive sidelobe-to-peak ratio of -7 dB. These distortions are attributed primarily to mixer products produced from undesired electromagnetic feedthrough of input signal onto the output line.

In the next stage of the device development, the spurious sidelobe levels will be reduced by improved design of the input and output transmission-line circuits. The time-bandwidth
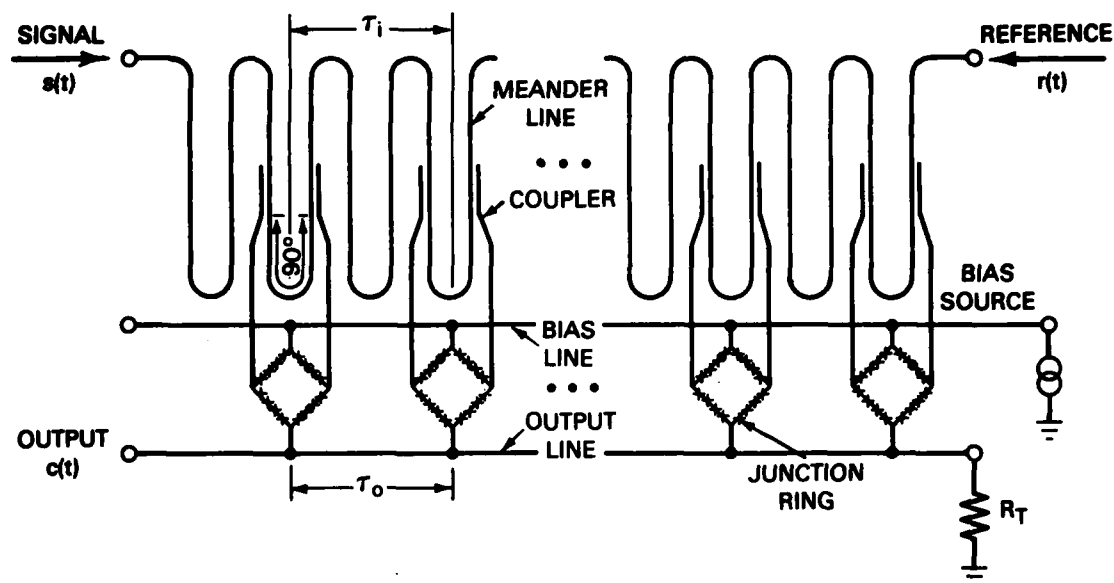
Figure 5-1. Schematic of superconductive convolver with a delay line for signal shifting, taps for sampling, junction rings for multiplication, and an output line for summation.
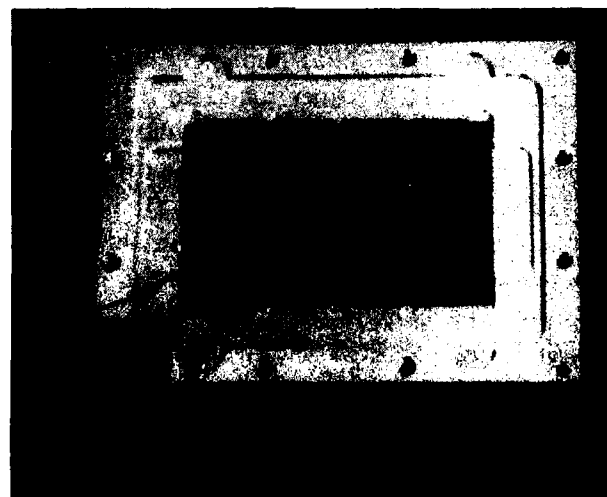
Figure 5-2. Photograph of superconductive convolver with top dielectric removed. Inset shows junction ring mixer with vertical connections to taps and bias horizontal line, and microstrip output line.

66

(a)

(b)

Figure 5-3. Convolver output for inputs of (a) gated CW tones and (b) wideband chirped waveforms.

142047-R

product of the convolver will be extended to 100 by increasing the duration of the input delay line from the current 14 ns to 50 ns and by integrating 100 junction ring mixers into the upgraded design. It appears feasible to eventually produce a convolver with a 10-GHz bandwidth that provides signal processing gains of up to 1000.

S.A. Reible
E.M. Macedo

5.2 HOLOGRAPHIC-GRATING ACOUSTIC-WAVE DEVICES

The concept of holographically written reflection gratings for acoustic waves has been discussed previously.[6] The hologram, which is stored in the bulk crystal as a spatially varying electric field, can interact with the acoustic wave by means of the electroacoustic effect. We have previously reported measurements of the electroacoustic coefficients[7] and shown that the predicted interaction of the acoustic wave with the holographic grating is strong enough to make practical signal-processing devices. In the following, we report the first observation of the reflection of acoustic waves from a holographically written grating.

Iron-doped lithium niobate (Fe:LiNbO$_3$) was chosen to demonstrate the effect. Fe:LiNbO$_3$ has been extensively studied as a storage medium for optical holograms, while undoped LiNbO$_3$ has well-known acoustic properties. Our earlier measurements on undoped LiNbO$_3$ demonstrated a sufficiently strong electroacoustic effect. However, the initial attempts to fabricate a bulk-acoustic-wave (BAW) delay line in LiNbO$_3$ with 0.1-percent iron doping have shown the material to have excessive acoustic loss above 200 MHz. The loss is approximately 20 dB/cm at 200 MHz and increases with frequency. These results indicate that our initial methods for the demonstration of reflection gratings would not work because of high acoustic propagation loss. Our goal is to eventually fabricate BAW reflective-array devices at frequencies well beyond the 1-GHz limit imposed by propagation losses in surface-acoustic-wave (SAW) devices. Indeed, the lowest convenient frequency for operation of the proposed BAW device would be 750 MHz, which is set by the practical need to define holographic gratings with a period of 5 μm or less. At 750 MHz the acoustic attenuation would be so high in the iron-doped material as to make the experiment impractical.

As an expeditious means to demonstrate the desired effect, we have used a SAW delay line fabricated on iron-doped LiNbO$_3$. The propagation loss of a surface wave is comparable to that of a bulk wave. However, short delay lines are much more conveniently fabricated with SAW than with BAW techniques. The interdigital transducers have a center frequency of 245 MHz; the third harmonic response centered at 735 MHz is used for the experiment. Since the SAW velocity is lower than the BAW velocity by nearly a factor of 2, a 2.4-μm-period holographic grating is required. The grating is written by the interference of blue light at λ = 4579 Å from an argon ion laser. Figure 5-4 shows the experimental arrangement with the SAW oriented to propagate in the Z direction on the X face of the sample. The overlap of the volume hologram with the surface wave is diminished compared with the bulk wave; thus the observed reflection is expected to be weaker.

STORED HOLOGRAPHIC GRATING

INPUT/
OUTPUT

SAW
DELAY LINE

f_0 = 245 MHz, $3f_0$ = 735 MHz
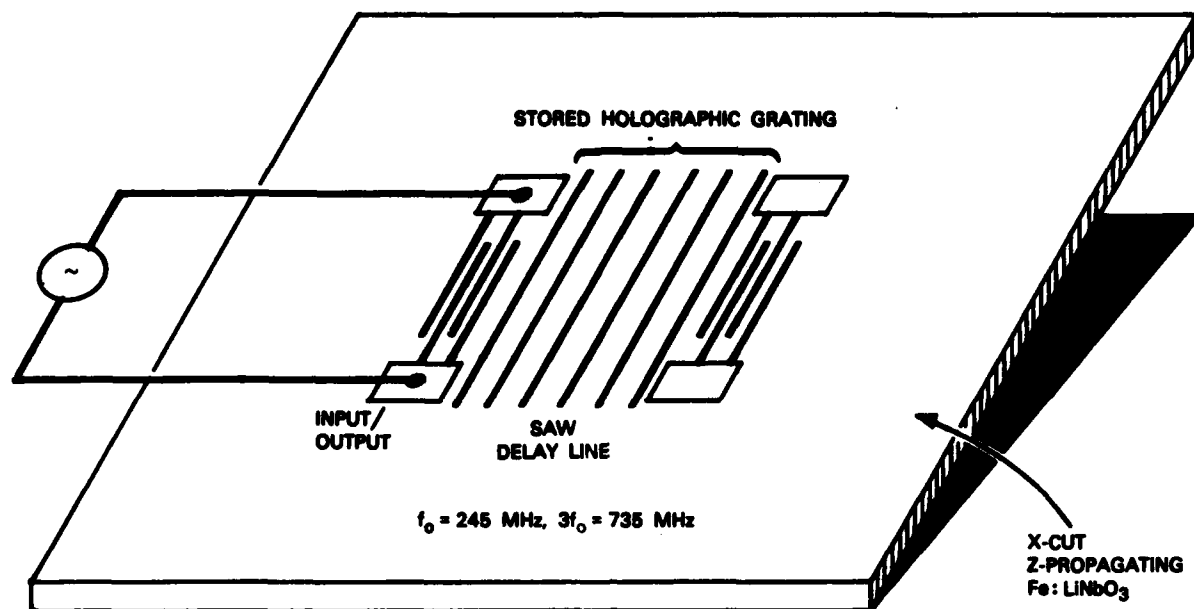
X-CUT
Z-PROPAGATING
Fe : LiNbO₃

142048-N

Figure 5-4. Schematic of holographic reflection grating device.

The reflection from the holographic grating is observed as a return signal to the input transducer which has been delayed by the round-trip transit time from transducer to the grating. Figure 5-5 shows oscilloscope traces of the output before and after 30 min. of hologram writing. The input RF pulse is seen and the signal is offscale at this sensitivity. Since the holographic reflection grating fills the entire crystal, the reflection is seen immediately after the RF input pulse is turned off. Also since the crystal has large propagation loss, the signal decays strongly for larger propagation delays. As expected, the frequency response of the effect is quite narrow. The reflection is accompanied by a decrease in transmitted signal in the conventional SAW delay line.

The reflected signal can be made to disappear and reappear by repetitive erase/write cycles of hologram.

These are the first observations of acoustic interaction with a holographically created grating. Efforts are now under way to better quantify the effects, including the excessive acoustic loss in doped LiNbO₃. Attempts will be made to fabricate short BAW delay lines on better doped material.

D.E. Oates
P. Gottschalk

69

(a)   BEFORE WRITE

(b)   30-min. WRITE

INPUT RF PULSE

REFLECTED ACOUSTIC PULSE
f = 743 MHz

142046-R

Figure 5-5. Reflected surface wave signal in device of Figure 5-4 with grating: (a) absent and (b) present.

70

REFERENCES

1. S.A. Reible, A.C. Anderson, P.V. Wright, R.S. Withers, and R.W. Ralston, IEEE Trans. Magn. MAG-19, 475 (1983).

2. Solid State Research Report, Lincoln Laboratory, M.I.T. (1983:1), p. 89, DTIC AD-A128894/3.

3. S.A. Reible, *1982 Ultrasonics Symposium Proceedings* (IEEE, New York, 1982), pp. 190-201.

4. Solid State Research Report, Lincoln Laboratory, M.I.T. (1983:3), p. 79.

5. R.S. Withers, A.C. Anderson, P.V. Wright, and S.A. Reible, IEEE Trans. Magn. MAG-19, 480 (1983).

6. Solid State Research Report, Lincoln Laboratory, M.I.T. (1984:1), pp. 73-77.

7. P.G. Gottschalk, D.E. Oates, and P.V. Wright, *1983 Ultrasonics Symposium Proceedings* (IEEE, New York, 1983), p. 1091.

REPORT DOCUMENTATION PAGE		READ INSTRUCTIONS BEFORE COMPLETING FORM
1. REPORT NUMBER ESD-TR-84-024	**2. GOVT ACCESSION NO.** *A147 640*	**3. RECIPIENT'S CATALOG NUMBER**
4. TITLE *(and Subtitle)* Solid State Research		**5. TYPE OF REPORT & PERIOD COVERED** Quarterly Technical Report 1 February — 30 April 1984
		6. PERFORMING ORG. REPORT NUMBER 1984:2
7. AUTHOR(s) Alan L. McWhorter		**8. CONTRACT OR GRANT NUMBER(s)** F19628-80-C-0002
9. PERFORMING ORGANIZATION NAME AND ADDRESS Lincoln Laboratory, M.I.T. P.O. Box 73 Lexington, MA 02173-0073		**10. PROGRAM ELEMENT, PROJECT, TASK AREA & WORK UNIT NUMBERS** Program Element No. 63250F Project No. 649L
11. CONTROLLING OFFICE NAME AND ADDRESS Air Force Systems Command, USAF Andrews AFB Washington, DC 20334		**12. REPORT DATE** 15 May 1984
		13. NUMBER OF PAGES 100
14. MONITORING AGENCY NAME & ADDRESS *(if different from Controlling Office)* Electronic Systems Division Hanscom AFB, MA 01731		**15. SECURITY CLASS.** *(of this report)* Unclassified
		15a. DECLASSIFICATION DOWNGRADING SCHEDULE

16. DISTRIBUTION STATEMENT *(of this Report)*

Approved for public release; distribution unlimited.

17. DISTRIBUTION STATEMENT *(of the abstract entered in Block 20, if different from Report)*

18. SUPPLEMENTARY NOTES

None

19. KEY WORDS *(Continue on reverse side if necessary and identify by block number)*

solid state devices	photodiode devices	infrared imaging
quantum electronics	lasers	surface-wave transducers
materials research	laser spectroscopy	charge-coupled devices
microelectronics	imaging arrays	acoustoelectric devices
analog device technology	signal processing	

20. ABSTRACT *(Continue on reverse side if necessary and identify by block number)*

This report covers in detail the solid state research work of the Solid State Division at Lincoln Laboratory for the period 1 February through 30 April 1984. The topics covered are Solid State Device Research, Quantum Electronics, Materials Research, Microelectronics, and Analog Device Technology. Funding is primarily provided by the Air Force, with additional support provided by the Army, DARPA, Navy, NASA, and DOE.